INVESTIGATIONS OF DOPED $L1_0$ FePt FILMS FOR HEAT ASSISTED MAGNETIC RECORDING (HAMR)

A THESIS SUBMITTED FOR THE DEGREE OF DOCTOR OF PHILSOPHY

XU DONGBIN

(B. Sci., Lanzhou University, China)

DEPARTMENT OF MATERIALS SCIENCE AND ENGINEERING

NATIONAL UNIVERSITY OF SINGAPORE

2013

Declaration

I hereby declare that the thesis is my original work and it has been written by me in its entirety. I have duly acknowledged all the sources of information which have been used in the thesis.

This thesis has also not been submitted for any degree in any university previously.

_____

Xu Dongbin

18 February 2013

ACKNOWLEDGEMENTS

Firstly, I would like to give the sincerest thanks to my supervisors Prof. Chow Gan-Moog and A/Prof. Chen Jingsheng for their constant support and invaluable suggestions throughout my whole Ph. D study. I benefit a lot from every discussion with them and the most important thing to me is how to think independently and critically.

The research facilities provided by the National University of Singapore (NUS), Data Storage Institute (DSI) and Argonne National Laboratory (ANL) are appreciated. Thanks should be given to Dr. Zhou Tiejun for his guidance in DSI. The temperature-dependent magnetic data collected with the help of Dr. Yi Jiabao is also acknowledged. Heartfelt thanks should be given to Dr. Sun Chengjun for his guidance during my stay in ANL to do the measurements using synchrotron radiation. I'm grateful for every fruitful discussion with him. Biplab Sanyal from Uppsala University is also appreciated for carrying the first-principle calculation.

Last but not least, I would like to thank my parents for their continuous care and love. The acknowledgement would be incomplete without mentioning my wife Loo Lin Jy for her thoughtful love and support.

CONTENTS

SUMMARY

$L1_0$ FePt with high magnetic anisotropy possesses the most promising role to realize the potential of heat assisted magnetic recording (HAMR) for ultra-high density recording. The issues of degradation and thermal design brought by the integration of thermal dimension in the writing process make the thermal investigation of $L1_0$ FePt HAMR media highly desirable. This thesis mainly focused on investigating the thermal-dependent structural and magnetic properties of $L1_0$ FePt using different doping elements. The doping effects and the relations between macroscopic properties (crystallographic structure, magnetic properties and their thermal dependences) and microscopic properties (local atomic structure and spin/orbital moments) were studied. An in-depth investigation on the effects of composition, heat sink layer and doping elements including Nd (rare-earth), Mn (3d-transition) and Rh (4d-transition) on the structural properties, magnetic properties and their thermal dependences of $L1_0$ FePt was pursued.

LIST OF TABLES

LIST OF FIGURES

LIST OF PUBLICATIONS

1. D. B. Xu, J. S. Chen, T. J. Zhou, and G. M. Chow, "Effects of Mn doping on temperature-dependent magnetic properties of $L1_0$ FeMnPt", J. Appl. Phys. 109, 07B747 (2011)
2. C. J. Sun, D. B. Xu, S. M. Heald, J. S. Chen, and G. M. Chow, "Directional short range order in $L1_0$ FeMnPt magnetic thin films", Phys. Rev. B 84, 140408(R) (2011)
3. D. B. Xu, C. J. Sun, J. S. Chen, S.-W. Han, S. M. Heald, R. A. Rosenberg, and G. M. Chow, "Investigation of spin and orbital moments of $L1_0$ FePtRh thin films", J. Appl. Phys. 111, 07C120 (2012)
4. C. J. Sun, D. B. Xu, D. L. Brewe, J. S. Chen, S. M. Heald, and G. M. Chow, "Investigation of Heat-assisted Magnetic Recording Media Films in Four Dimensions", IEEE Trans. Magn. (2013) (in-press)
5. D. B. Xu, C. J. Sun, D. L. Brewe, S. W. Han, P. Ho, J. S. Chen, S. M. Heald, X. Y. Zhang, and G. M. Chow, "Spatiotemporally separating electron and phonon thermal transport in nanostructured magnetic thin films" (submitted)
6. D. B. Xu, C. J. Sun, J. S. Chen, S. M. Heald, B. Sanyal, R. A. Rosenberg, T. J. Zhou and G. M. Chow, "Large Enhancement of the Magnetic Moment in $L1_0$ Ordered FePt Thin Films by Nd Doping" (submitted)
7. D. B. Xu, C. J. Sun, J. S. Chen, T. J. Zhou, S. M. Heald, and G. M. Chow, "Tuning the Curie temperature of High Structural Ordered Magnetic Thin Films through Direction Selective Element Doping" (to be submitted)

I. INTRODUCTION

Information growth has experienced an unprecedented explosion since the revolution of the modern electronic techniques. For example, the global information grew from 100 Exabytes (EB) (1 Exabytes = 10^{18} bytes) in 2005 to 750 Exabytes in 2009 within just 4 years [1]. For comparison, all the catalogued books in America's Library of Congress are just 15 Terabytes (TB) (1 Terabytes = 10^{12} bytes) [2]. To date, the growth rate continues. Three major approaches to store high capacity data are magnetic recording (*e.g.* Tape, Hard disk drives (HDDs)), semiconductor devices (*e.g.* flash) and optical storage (*e.g.* CDs, DVDs). Among these three techniques, HDDs hold the superiority by providing the highest areal density and lowest average price ($/GB). Basically, the requirements for the development of information storage are high capacity, small size and low cost. In essence, the only way to satisfy all these three requirements simultaneously is to increase the areal density. In this chapter, the development of HDDs together with the challenges will be described (section 1.1). The next generation techniques for fabricating HDDs media and prospects will then be discussed (section 1.2). Finally, the current status of heat assisted magnetic recording (HAMR) media will be reviewed and discussed in details (section 1.3).

1.1 THE DEVELOPMENT OF HDDS AND CURRENT CHALLENGES

Hard disk drives (HDDs), known as the non-volatile storage of digital data in a random-access manner, have made a tremendous increase in areal density in the past five decades. The first hard disk drive named as Random access method of accounting

and control (RAMAC) was introduced by International Business Machines Corporation (IBM) in 1956. At that time, it only had an areal density of around 2 Kbits/in^2, corresponding to a total capacity of 5 Megabytes (MB) (1 Megabytes = 10^6 bytes) with fifty 24-inch platters. To date, the areal density of commercial HDDs available in industrial production is around 600 Gbits/in^2, which is about 300 million times of inception value [3].

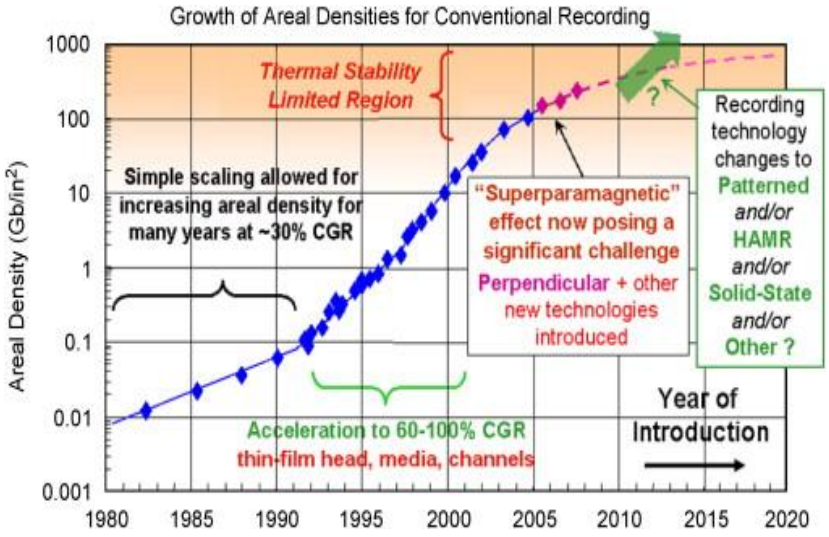

Fig. 1. The areal density evolution for HDDs in the past several decades (Courtesy of R. Wood [4])

The areal density enhancement of HDDs from 1980 is shown in Fig. 1. From 1960s to 1990s, the increase in areal density was mainly attributed to the simple scaling of bit size, which maintained a compound growth rate (CGR) of 30 %. With

introduction of magneto-resistance (MR) and giant magneto-resistance (GMR), together with the switching of the recording mode from longitudinal to perpendicular recording, the CGR was boosted up to 60-100 %. This is called Kryder's law [5], which was even faster than the doubling transistors in one certain area every 2 years predicted by Moore's law [6],[7]. The discovery of GMR led to the award of the 2007 Nobel Prize in Physics.

1.1.1 SUPERPARAMAGNETIC LIMIT

The bit size cannot be infinitely shrunk for a certain recording material. It will eventually face the problem known as the superparamagnetic limit. The occurrence of superparamagnetic effect is due to the competition between the anisotropy energy $K_u V$ (K_u: uniaxial magneto-crystallize anisotropy, V: grain volume) and the thermal agitation energy $k_B T$. When single-domain particles become small enough, $K_u V$ would become so small that energy fluctuations caused by thermal agitation could overcome the anisotropy forces. This may lead to spontaneous reversal of magnetization of a particle from one easy direction to the other, even without any applied external field.

Normally, the thermal decay of magnetization can be expressed by the following equations

$$\mathrm{M} = \mathrm{M}_0 \exp\left(-\frac{\mathrm{t}}{\tau}\right) \quad \tau = \frac{1}{f_0}\exp\left(\frac{K_u V}{k_B T}\right) \tag{1-1}$$

where f_0 is frequency factor with the typical value of $10^9 - 10^{10}$ Hz, V is volume of the particle under consideration, T is absolute temperature, k_B is Boltzmann's constant and K_u is anisotropy constant. From these equations, it can be concluded that at a finite

temperature, the magnetization of the particles has a probability to switch direction even in the absence of external magnetic field. Regarding a group of particles, a decay of magnetization can be observed as a function of time.

1.1.2 TRILEMMA IN MAGNETIC RECORDING MEDIA

For magnetic recording media, there are three imposed constraints. They are SNR (Signal-to-Noise Ratio), thermal stability and writability. Among these, a balance must be achieved.

The SNR is an important parameter in determining the error rate and the reliability of read-back signal in HDDs. The noise arising in reading process consists of direct current (DC) noise and transition noise. DC noise is due to the non-uniformity in the grain size and the grain orientations. Transition noise arises from the transition region and is related to the interaction between grains. It is mainly determined by exchange coupling and magneto-static interaction among grains. In order to increase SNR, small, uniform and exchange decoupled grains are therefore required. SNR can be expressed as

$$\mathrm{SNR(dB)} = 10\log(\mathrm{N}) \tag{1-2}$$

where N is the number of grains per bit. Reduction in grain size per bit leads to increase of N and thus SNR. However, only reduction in grain size without a reduction in exchange coupling would not be beneficial. If there is a large exchange coupling between the grains, a few grains will couple together and act as a magnetic

cluster. Therefore, the effective magnetic unit can be larger than the physical grain.

Decrease in grain size can increase the areal density and SNR. However, when the size of grain decreases, the magnetic anisotropy energy $K_u V$ also decreases and eventually becomes comparable to the thermal energy $k_B T$. Due to the superparamagnetic effect, magnetization can be easily switched by the thermal energy.

Normally, a ratio of 60 for energy barrier $K_u V$ (here V is the volume of grain) and thermal agitation energy $k_B T$ are required for the magnetization of the grains to remain thermally stable for 10 years.

$$\frac{K_u V}{k_B T} \geq 60 \tag{1-3}$$

Basing on this requirement, one method to maintain this ratio is to increase K_u by introducing high anisotropy materials such as $L1_0$ FePt. However, K_u cannot be infinitely increased due to the limitation of writing field known as the writability. The conventional writer using FeCo-based alloy has a magnetic saturation (B_s) of 2.4 T. Consider the gap between the head and the recording media, the effective field that acts on recording media is only around 1.9 T (80 % of B_s) [8]. Simulations showed that the areal density of conventional perpendicular magnetic recording (PMR) cannot exceed 1 Tbit/in^2 due to the limitation of writing field [9]. The limited value of a writing filed will therefore constrain the value of anisotropy constant of a recording media that can be used to counter the undesirable superparamagnetic effect.

The other method to maintain the ratio is by increasing grain volume *V*, which can be realized in the bit-patterned media (BPM). In this approach, one bit is represented by one grain to maintain thermal stability. These two proposed approaches for next generation magnetic recording media will be reviewed and discussed in the following section.

1.2 NEXT GENERATION MAGNETIC RECORDING TO EXTEND AREAL DENSITY BEYOND 1 TBITS/IN^2

Conventional perpendicular magnetic recording firstly proposed by Iwasaki [10] has a limitation on the highest writing field that can be achieved. As mentioned that simulations showed the areal density of conventional PMR cannot exceed 1 Tbit/in^2 due to the limitation of writing field [9]. In order to further increase the areal density beyond 1Tbits/in^2, several methods have been proposed. Among these, exchange coupled composite (ECC) media and heat assisted magnetic recording (HAMR) attempt to improve the writability, thus allowing the use of materials with smaller grain size and higher anisotropy. Bit-patterned media (BPM) aims to improve the thermal stability without deteriorating the writibility and SNR.

1.2.1 EXCHANGE COUPLED COMPOSITE (ECC) MEDIA AND GRADED MEDIA

The ECC media provides a method to reduce the media switching field without compromising the thermal stability. The concept of ECC was first proposed by R. H. Victora and X. Shen in 2004 [11]-[13]. Later a similar concept named “exchange spring media” was independently proposed by Suess *et al.* [14],[15]. In principle, the

ECC media consists of a magnetically soft phase and a magnetically hard phase in the same grain. The hard phase provides the thermal stability and soft phase provides assistance in magnetization reversal. When applying an external field, the magnetization of the soft magnetic phase reverses first. At the same time, it exerts a torque to the hard phase through the exchange coupling as shown in Fig. 2. The energy barrier for reversing both phases equals to the difference of (a) the domain wall energy in hard phase and (b) the domain wall energy plus the nucleation energy in the soft phase. In order to fully utilize the ECC potential, the thickness of soft phase should be optimized.

The "figure of merit" $\xi=2E_b/(M_sH_sV)$ is used for evaluation. Here E_b M_s, H_s and V are energy barrier (higher barrier is preferred to suppress thermal fluctuation), saturation magnetization, switching field and grain volume, respectively. For an ideal conventional perpendicular recording media, where grains coherently switch in the Stoner–Wohlfarth (S-W) model, $\xi=1$. Based on a two-spin model, a maximum of $\xi=2$ can be found for the two layer composite media [16]. The graded media as shown in Fig. 2, where magnetic anisotropy continuously varies, is promising to further increase ξ [16]. For this media, the ξ can be extended to 4 at most. The configuration of quadratic anisotropy variation is very close to this limit [17]. However, Victora suggested that the practical ξ that can be achieved would be only around 2.6 for graded media with a total film thickness at about 15 nm [18].

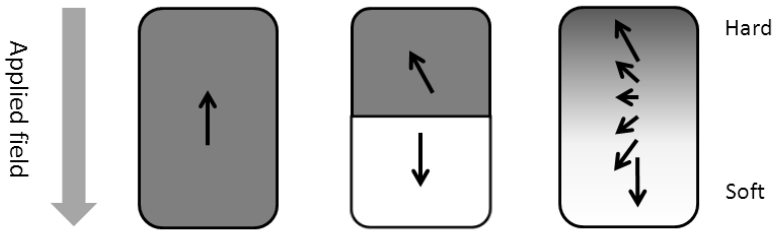

Fig. 2. A schematic representation of the structure of conventional media (left), ECC media (middle) and graded media (right) with magnetic field applied to switch the magnetization of hard phase

The advantage of this technique is that the ECC media can be directly implemented into the mature conventional perpendicular recording system. However, the difficulties in controlling of magnetic anisotropy distribution and columnar structure remain challenging. As discussed above, this method can only extend the areal density 2-3 times in practice. For further increasing the areal density up to 5-10 Tbits/in^2, alternatives such as two dimensional magnetic recording (TDMR), bit-patterned media (BPM) and heat assisted magnetic recording (HAMR) need to be considered.

1.2.2 TWO DIMENSIONAL MAGNETIC RECORDING (TDMR)

TDMR combines two techniques: shingled write recording (SWR) and 2-D read back and signal-processing. In SWR, the tracks are overlapped and a wide write-pole

with one side-shield is used. During writing, only a narrow part along one edge of the track remains when writing the adjacent track since the tracks are overlapped. This can provide a stronger write field due to larger pole and sharp corner-edge field. However, the main challenge for SWR is that a single track cannot be updated without affecting the adjacent tracks. Normally, the adjacent tracks must be stored before writing the target track and then be recovered in to the disk after the target track is updated. Therefore, an effective buffer caching will be needed. Solid state disk (SSD) technology can be a good choice for embedded cache [19]. Additionally, TDMR reads the information from several adjacent tracks simultaneously so that a powerful 2-D coding and 2-D signal-processing should be applied.

Theoretically, TDMR may approach the capacity with one bit represented by one grain if both the writing process and read back process have high resolution and low noise [19]. However, more research will be warranted to fully assess the viability of the TDMR concept.

1.2.3 BIT-PATTERNED MEDIA (BPM)

Bit-patterned media is a proposed strategy to break the trilemma by increasing the grain size as previously discussed in section 1.1.2. In this method, the recording bits can be physically separated and one recording bit can be represented by one grain instead of many grains in a recording bit of a conventional media. As a result, the grain size may be increased [20]. The magnetic media used in patterned media is different from the conventional media. In patterned media, each bit can switch by

following the Stoner-Wolfarth (S-W) mode since the grains are well separated from each other to realize the fully decoupling. The isolation of bits is controlled by patterning where the transition is well defined. The transition noise can therefore be significantly reduced.

Table 1. Comparison of different lithograph techniques for patterning. The areal density was estimated by assuming an aspect ratio of 2 with shorter direction in down track and a filled area of 60 % (Courtesy of E. A. Dobisz *et al.* [20])

Patterning methods	**Resolution (center to center)**	**Estimated areal density (Gbits/in^2)**	**Grain size (nm^2)**	**Advantages**	**Challenges**
Deep UV lithograph	100 nm	32	60 ×120		Low resolution
Extreme UV lithograph	15 nm	1430	9 ×18	Good resolution	Only useful for line, square and rectangular pattern, unsuitable to pattern sufficiently large area
Synchrotron X-ray lithography				Good resolution	Not an easy access, too expensive
Nanoimprint lithography	10 nm	3225	6 ×12	High resolution, throughput and imprint uniformity	Depends on mold quality
Electron beam lithography	10 nm	3225	6 ×12	High resolution	Time consuming and costly, low throughput and high expense of rotary stage e-beam tool
Self-assembly	3 nm	36000	1.8 ×3.6	Ultrahigh resolution, well controlled grain size and size distribution	High ordering temperature of FePt may deteriorate grain size, size distribution and texture

However, there are many challenges to fabricate patterned media. Table 1 shows the different lithograph techniques for patterning and the estimated maximum areal density. Among these, electron beam lithography (EBL) and nanoimprint lithography (NIL) have the resolution smaller than 25 nm [21]. Normally, these two methods are involved together in the patterning process. Firstly, a master disk pattern is developed by using EBL. After that, the master mold would be replicated into subsequent daughter and granddaughter molds, which would imprint hundreds of disks per hour. Finally, the pattern is imprinted into the disk using physical or chemical etching processes. For EBL, the major issues are throughput and expense of the rotary stage e-beam tool, which makes the price of each master very expensive. For example, the time for patterning a data area of 65 mm diameter disk at a bit density of 1 Tbits/in^2 with e beam current 10nA on polymethyl methacrylate (PMMA) would be 16 days [20]. For NIL, it is important to ensure the accuracy of replication. It could be achieved by choosing low-viscosity resist and controlling resist thickness. Besides these, the integration of BPM with HDDs is a challenge. In patterned disks, control of the head-to-disk interface may require a low-cost disk planarization scheme [22], thus a complex track-following servo mechanism will be required to keep the magnetic read-write head on the track.

1.2.4 HEAT ASSISTED MAGNETIC RECORDING (HAMR)

Heat assisted magnetic recording (HAMR) is a promising technique proposed to extend the areal density limitation of conventional perpendicular recording up to 5-10 Tbits/in^2. During the writing process, the thermal energy is utilized to temporally reduce the coercivity of magnetic material, making it compatible with the currently achieved maximum magnetic field of ~2.4 T.

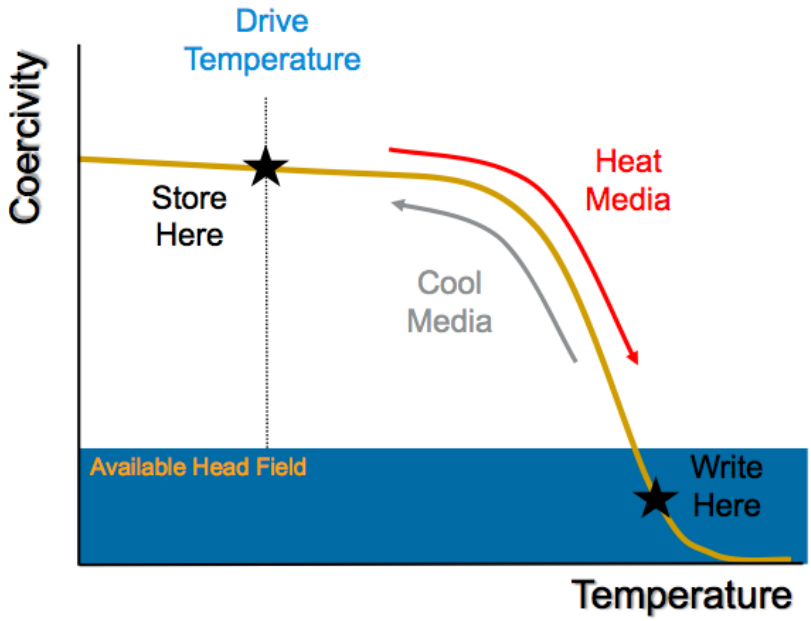

Fig. 3. The basic principle of HAMR (Courtesy of M. H. Kryder [23])

In this technique, a fine laser beam is used to heat the local area where the information will be written. As shown in Fig. 3, when the temperature approaches Curie temperature (T_C), the coercivity decreases rapidly [23]. This allows the switching of magnetization by the applied field produced by the currently used

recording head. In the presence of writing field, the laser beam is then removed and the temperature decreases. Eventually, the information is encoded with the form of magnetization orientation and can then be stored in the media for a time of more than 10 years [23].

The reason that recording must be done near T_C is due to the reversal dynamics. It was reported that the linear reversal mode, which is expected to play a crucial role in ultrafast reversal and recovery of magnetization for high writing rate due to its lower effective energy barrier compared to coherent rotation, can only exist in the vicinity of T_C based on the Landau-Lifshitz-Bloch equation [24]. In other words, the writing temperature for HAMR needs to be very close to or even above T_C. However, $L1_0$ FePt possesses a high T_C of 750 K, which imposes stringent requirements on the media overcoat, lubricants and optical system [23]. Therefore, reducing T_C while simultaneously maintaining a reasonable K_u are crucial for the application of HAMR.

Currently, the main challenges to realize HAMR are as follows:

- A laser must be integrated into the writing head to locally heat the media material. In this process, laser focusing, the efficiency of light delivery and heating effects on the writing head need to be considered.
- The recording should be done around the Curie temperature. For $L1_0$ FePt and CoPt, T_C is 750 K and 840 K, respectively. Currently, there are no overcoat and lubricant materials that can withstand such high temperature.

Therefore, new thermally stable overcoat and lubricant need to be developed.

- It requires very fast cooling rate due to the requirement of a high writing rate, the typical stay time for writing one bit is just around 1 ns.
- High field gradient (high temperature gradient) is preferred in recording process in order to avoid adjacent erasure in cross-track direction and reduce transition length in down-track direction.

For the last two challenges, the most promising method is to use a heat sink layer as discussed in the following.

One of the most important aspects needs to be considered in HAMR is thermal design. In conventional recording, the spatial and temporal variation of the recording head magnetic field $H(x,y,z,t)$ is dominant. In HAMR, however, the recording field gradient is dominated by the thermal gradient [23] which will be discussed in the following section. The high writing field gradient in HAMR will give two advantages. First, adjacent erasure in cross track and magnetization transition length in down track may be minimized. Second, the heat can be targeted on one bit and used in high efficiency without wasting in the area around the bit.

The use of pulsed laser has also been shown to significantly reduce the time averaged optical power in order to achieve the same temperature compared with the continuous heating [23]. Generally, these advantages make the HAMR a promising approach to high areal density magnetic recording.

As mentioned preciously, the promising approaches to extend the areal density up to 10 Tbits/in^2 are TDMR, BPM and HAMR. However, all of these options currently face their own technical challenges.

An alternative approach is to combine some of the above techniques. For example, SWR itself can be applicable to 2 Tbits/in^2 with conventional PMR. However, a theoretical areal density up to 10 Tbits/in^2 may be achieved by combined with 2-D magnetic recording [19]. BPM and HAMR can also work together to further increase the areal density.

1.3 A REVIEW OF HIGH ANISOTROPY $L1_0$ FEPT FOR HAMR

1.3.1 OVERVIEW OF HIGH ANISOTROPY MATERIALS

A list of the high anisotropy materials is shown in Table 2. In this table, each grain was assumed to be a 10 nm tall pillar or column when estimating the smallest thermal stable grain with the diameter of D_P. The Co-based alloy has shown good properties in the conventional magnetic recording. However, the small magnetic anisotropy constant limits their potential in further increasing the areal density beyond 1 Tbits/in^2. The Co/Pt material with multilayered structure possess relative high anisotropy, which originates from the interfacial anisotropy [25],[26]. It was reported that the anisotropy of 1×10^7 erg/cc can be obtained in the multilayer structured Co/Pt [26]. Although these materials exhibit good recording performance, the relative low

gain in anisotropy in these materials limits their potential in further extending the high areal density up to 5-10 Tbits/in^2.

The material with the highest magnetic anisotropy is $SmCo_5$. Highly perpendicular textured $SmCo_5$ film could be prepared using magnetron sputtering on Cu/Ti dual underlayer [27]. In the optimized condition, a magnetic anisotropy of 4×10^7 erg/cc was obtained. It was also reported that granular and magnetically decoupled grains can be obtained using Cu-Ta_2O_5 granular underlayer [27]. Recently, epitaxial $SmCo_5$ thin films with strong perpendicular magnetic anisotropy of 7.6×10^7 erg/cc have been fabricated with pulsed laser deposition on heated Ru buffered Al_2O_3 (0001) substrates [28]. However, $SmCo_5$ has low corrosion resistance due to its rare-earth content. Although the corrosion resistance could be improved slightly with Cu seedlayer, it is still not compatible with the practical application [29].

Table 2. A list of high anisotropy materials (The smallest thermal stable size (diameter: D_p) to maintain the magnetic state for 10 years is estimated by assuming a cylinder with the thickness of 10 nm at room temperature of 300 K; A=10^{-6} erg/cm is the exchange coupling constant) (Courtesy of D. Weller [30], T. Klemmer [31] and M. H. Kryder [23])

Alloy system	Material	K_1 (10^7 erg/cm^3)	M_s (emu/ cm^3)	$H_k=2K_u/M_s$ (kOe)	T_C (K)	$D_c=5.6\cdot(A\cdot K_u)^{1/2}/M_s^2$ (largest single domain particle size)(nm)	$D_p=(60k_BT/K_u)^{1/3}$ (nm) (τ=10 years)
Co-alloys	$CoCr_{20}Pt_{15}$	0.3	330	18.2	-	-	10.3
	Co_3Pt ($L1_2$)	2	1100	36.4	-	208	4.0
	$(CoCr)_3Pt$	1	800	25.0	-	-	5.6
	$CoPt_3$	0.5	300	33.3	600	-	8.0
Co/Pt (Pd) multilayer	Co2/Pt9	1	360	55.6	500	-	5.6
	Co2/Pd9	0.6	360	33.3	500	-	7.3
$L1_0$ phase	FePd	1.8	1100	32.7	760	197	4.2
	FePt	7	1140	122.8	750	345	2.1
	CoPt	4.9	800	122.5	840	613	2.5
	MnAl	1.7	560	60.7	650	714	4.3
Rare-earth alloy	$Fe_{14}Nd_2B$	4.6	1270	72.4	585	234	2.6
	$SmCo_5$	20	910	439.6	1000	964	1.3

Among the high anisotropy materials, $L1_0$ FePt (with the second highest magnetic anisotropy in Table 2) is considered as the most promising material due to its relative high anisotropy, high corrosion resistance and intermediate T_C. However, considerable challenges remain. The high temperature required to induce the chemical ordering makes it difficult to obtain small grains since high temperature may promote grain growth. The thermal design in controlling (001) texture and the isolation of grains also warrant careful consideration in the section c.

1.3.2 $L1_0$ FePt

a. The structure of $L1_0$ FePt

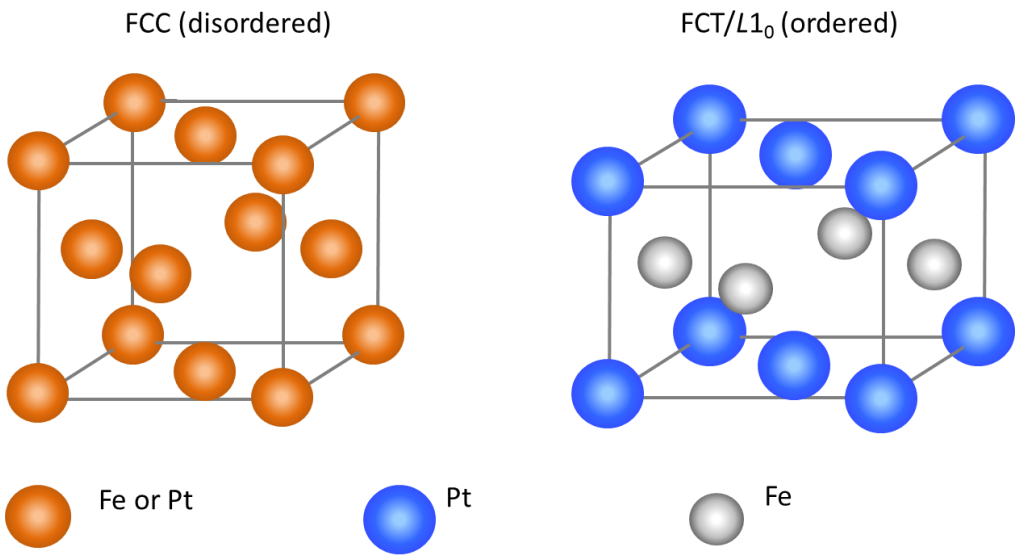

Fig. 4. Atomic structures of FCC (left) and FCT (right) phases for FePt

The $L1_0$ FePt phase belongs to the P4/mmm space group, with the configuration of alternating layers of Fe and Pt atoms stacked along the [001] direction, is classified as a face centered tetragonal (FCT) phase (Fig. 4). The disordered phase is a face centered (FCC) structure with Fe and Pt atoms randomly distributed on the lattice sites (Fig. 4). The transition temperature from FCC to FCT is as high as 1300 ^{o}C [32]. Therefore as-deposited FePt films without *in-situ* heating showed chemically disordered FCC phase and were magnetically soft [33]. In order to obtain the $L1_0$ FePt, *in-situ* heating or post-deposition annealing is required to overcome the energy barrier for atom diffusion. Several approaches such as element addition, strain or stress induced $L1_0$ ordering and irradiation-induced ordering may be used to promote the ordering which will be discussed in the following.

The long range chemical order parameter S represents the probability of correct site occupation in the $L1_0$ phase, which is given by

$$S=r_\alpha+r_\beta-1=(r_\alpha-x_A)/y_\beta=(r_\beta-x_B)/y_\alpha \quad (1\text{-}4)$$

where x_A and x_B are the atom fractions of the two components, y_α and y_β are the fractions of the lattice site types α and β in the ordered structure, and r_α and r_β are the fractions of each type of lattice site occupied by the correct types of atom (A on α and B on β). S as determined here represents the volume average long range order parameter. The maximum order parameter for the given film composition is given by $S_{max}=1-2\Delta x$, where Δx is the compositional deviation in atom fraction from the equiatomic composition 50 at. % [34].

b. The origin of high anisotropy

The understanding of the origin of high anisotropy in $L1_0$ FePt is very crucial for tuning and optimizing the magnetic properties for application. The origin of high anisotropy in $L1_0$ FePt has been studied. Simulation works based on the first-principle calculations [35] showed that the large magnetocrystalline-anisotropy energy (MAE) originated from the combined effects of a tetragonal structural distortion, the exchange splitting, and the spin-orbit splitting of Pt. However, a detailed experimental work for this system has not been carried for a full understanding of its origin. It is believed that the interface of Fe-Pt atomic planes plays an important role in the origin of high magnetic anisotropy. A study on Co-Pt interface in a similar system which

consists of Co/Pt multi-layers using X-ray magnetic circular dichroism (XMCD) measurements [36] showed that the Pt 5d-Co 3d hybridization could strongly enhance the perpendicular Co orbital moment, thus the high perpendicular magnetic anisotropy (PMA). From both theoretical and experimental studies, it would be concluded that the spin-orbital interaction of Pt played an important role in inducing the PMA in $L1_0$ structure.

Temperature-dependent anisotropy was also investigated by several groups. Experimental works showed that in $L1_0$ FePt, the anisotropy exhibited an unusual temperature dependence of $K_u^{eff} \propto M^2$ [37],[38]. Simulation interpreted this unusual exponent with the methods of *ab initio*, Langevin dynamics and constrained Monte Carlo [39],[40]. Asselin *et al.* found an easy-plane anisotropy which is an order of magnitude weaker than the easy-axis two-ion anisotropy. The existence of these two competing anisotropies gives rise to the unusual scaling exponent. Despite numerous experimental and theoretical studies, a full understanding of PMA and its temperature dependence has not yet been achieved.

c. Structural requirements of $L1_0$ FePt for HAMR

i. chemical ordering

The chemical ordering of $L1_0$ FePt can be achieved by several methods. These methods are mainly based on the concept that the atoms are given certain energy and then they can step over the potential barrier to achieve the chemical ordering state, which is more stable than the chemical disordered state at room temperature.

- The ordering temperature may be reduced by doping with different elements such as Ag [41], Cu [42],[43] Cr [44], *etc.*. Ordering temperature could be reduced to 340 ^{o}C by introducing a Cr top/bottom layer and a 0.2 nm thick Cu interlayer [44]. The reduction in ordering temperature could be due to the deviation of the FePt composition from equiatomic composition rather than the doping element [44].
- Ion irradiation has been used to promote ordering processes and to modify the magnetic properties of magnetic thin films [45],[46]. The introduction of vacancies by ion irradiation reduced the ordering temperature without undesirable grain growth. Chemical ordering in thin FePt film was induced by He^{+} ion irradiation by introducing energy to step over phase transition energy barrier [45]. Sun *et al*. reported that the ordering was significantly enhanced by bombarding with H ion [46]. The activation energy for Fe and Pt vacancies calculated using first-principle showed a much smaller value than order-disorder transition energy [47].
- Alternate deposition of monatomic FePt thin film yielded high degree of ordering with acceptable texture. The anisotropy as high as 6 x 10^{7} erg/cc was achieved [48]. However, this approach cannot be used in industrial application due to its slow process and low yield.
- The heat treatment of multilayered FePt films could reduce the processing temperature because of the enhancement in inter-diffusion among the thin

layers. However, it led to dispersion of crystalline orientation since the thickness of each film was too thin to attain the (001) orientation [49].

- Suzuki *et al.* [50] demonstrated that chemical ordering was obtained using high Ar sputtering pressure. It was suggested that compressive stress along the *c*-axis promoted the chemical ordering. By using CrRu as the underlayer and MgO as the intermediate layer, the ordering temperature was significantly reduced to around 350 ^{o}C [51],[52]. This was mainly attributed to the optimized lattice mismatch between the CrRu, MgO and $L1_0$ FePt. Hsiao *et al.* investigated the effects of initial stress/strain state on the order-disorder transformation of FePt thin films. It showed that strong tensile stress in the in-plane direction facilitated the nucleation of $L1_0$ FePt [53].

ii. Texture

The (001) texture is preferred in perpendicular magnetic recording. However, the as-deposited FePt at room temperature usually exhibits (111) orientation. There are mainly two methods to induce the (001) texture. One is of the control of FePt (001) texture by epitaxy. For example, using the epitaxial relation FePt (001) <100> || MgO (100) <001>, good (001) texture was obtained [54],[55]. Multilayered structure $[Fe/Pt]_n$ could also be used to control the (001) texture during its annealing process. The annealing time, temperature and thickness of Fe or Pt were very crucial in control of the FePt (001) texture [56],[57].

iii. Grain size

Grain size could be reduced by doping with C [52], Au [58] and Ag [59] or some other oxide such as SiO_2 [60], Ta_2O_5 [61] and MgO [62] since these amorphous materials can easily diffuse to the grain boundary and hence isolate grains. However, this method does not provide a precise control of the grain size and the grain size distribution. Furthermore, many doping materials may deteriorate the magnetic properties [62]. A pinning type FePt perpendicular media was introduced by Suzuki *et al.* [63]. With Ag pinning layer, it showed pinning sites could obstruct the movement of domain wall and hence reducing exchange coupling [64]. Recently, Zhou *et al.* reported the fabrication of (001) textured anisotropy graded FePt films (grain size 5.3 $\pm$1.1 nm) doped with TiO_2 [65]. With the doping TiO_2 concentration of 12.5 %, the films exhibited the highest switching field and approached the S-W reversal mode, implying the existence of the exchange decoupled grains.

The isolation of grains was related to the lower surface energy of doping materials that easily diffused to the grain boundaries. Chen *et al.* [61] compared three dopant materials of C, TiO_2 and Ta_2O_5. Among these materials, Ta_2O_5 showed better ability in isolating grains.

d. Thermal requirements of $L1_0$ FePt for HAMR

i. Curie temperature

As discussed previously, high T_C not only has effects on the materials used for overcoats and lubricants but also put forward a claim to the heating source, thus reducing T_C is very crucial for application of HAMR. Curie temperature can be

reduced by doping with transition elements such as Ni [37], Cu [66]. However, the reduction in Curie temperature will deteriorate the anisotropy. Therefore, a tradeoff between anisotropy and Curie temperature should be made.

It is known that the Curie temperature is determined by the spin-spin exchange interaction and closely related to the so-called magnetic order in magnetic materials. The reduction of the Curie temperature of $L1_0$ FePt by doping Ni and Cu may be attributed to the change of local atomic environment and thus the spin-orbital interaction.

Curie temperature has a proportional relation with the grain size. It is because that the ratio of surface atoms to internal atoms becomes larger and larger when grain size decreases. The surface layer contains atoms with coordination number imperfection comparable to that of the bulk. Lu *et al.* [67] reported the size dependent ordering temperature and Curie temperature. It showed that the Curie temperature decrease significantly when the grain size is smaller than 5 nm.

It was also reported that the Curie temperature can be reduced by doping with B_2O_3 [68]. The grain size decreased from 25 nm to 15 nm with doping concentration of 0 and 25 %. But the grain size is larger than 5 nm, its properties still approaches bulk. In their conclusion, observed phenomena originated in the variation of the exchange interaction parameters with the changes in the *c*/*a* ratio. The change of *c*/*a* ratio is due to the stress from doping materials.

ii. Field gradient

The high effective field gradient in HAMR is not due to the recording head, but rather the thermal design of the magnetic recording media material [23]. This may be understood by using the simple relation:

$$\frac{dH_k}{dx} \sim \frac{dH_k}{dT} \cdot \frac{dT}{dx} \tag{1-5}$$

Here dH_k/dT is the slope of the temperature-dependent anisotropy field H_k near T_C. Typically, the recording field gradient has an enhancement of 3-20 times due to thermal gradient compared to that only due to conventional anisotropy field gradient [23]. However, the Curie temperature has a distribution in reality. Knight *et al.* [69] investigated the HAMR adjacent track stability in the presence of a medium Curie temperature distribution. The results showed that Curie temperature distribution had little effects on adjacent track erasure. However, it would widen the transition width.

iii. Lattice and magnetic dynamics with laser pulse heating

Since the new degree of freedom – temperature is involved in the writing process of HAMR, the heating/cooling issues have been identified as the most crucial factor for HAMR media in both static and dynamical aspects [23]. In this thesis, the concern was given to $L1_0$ FePt. Although many static thermal studies have been done for $L1_0$ FePt to reduce Curie temperature with doping materials [37],[70] and to enhance the cooling rate with the heat sink layer, the real writing process involving dynamical aspect have still not been comprehensively addressed in details. As a result, the 4th

dimension - time must be emphasized in the current research to have a practical study in a real-time, real-place and real-material situation.

1.4 THE OBJECTIVE OF THIS RESEARCH

HAMR is a proposed technique which has the potential in further increasing the areal density beyond 1Tbits/in^2. The realization of HAMR relies on many aspects, such as the control of laser [71] -[73] and the choice of media materials. $L1_0$ FePt is a very promising media material to be applied in HAMR as it was reported possessing high corrosion resistance and high magnetic anisotropy [31]. The high anisotropy allows FePt films to accommodate very small magnetically stable grains to delay the superparamagnetic limit. The Curie temperature of $L1_0$ FePt is as high as 750 K [68]. For HAMR media application, the media needs to be heated up to approach the Curie temperature for reversal dynamics. However, this high Curie temperature would also put a stringent demand on the thermal system, overcoat and the lubricant. Therefore, the reduction of Curie temperature is essential. Reduction of Curie temperature is usually accompanied by a decrease of anisotropy. A tradeoff between these two intrinsic properties should be made.

In this thesis, the thermal properties of $L1_0$ FePt on both the static and dynamic aspects were investigated in order to have a better knowledge on the equatomic $L1_0$ FePt. The effects of a heat sink layer (such as Ag) were also considered. The effects of dopant, *i.e.* 3d transition metal (Mn), 4d transition metal (Rh) and even the rare earth element (Nd) in $L1_0$ FePt on Curie temperature were studied. In this thesis,

doping is referred to incorporating another element in the FePt. The detailed investigations on both macro properties (crystallographic structure, magnetic properties, thermal effects, *etc.*) and micro properties (spin and orbital moments, local atomic environment, directional short-range order, *etc.*) were pursued for better understanding.

1.5 THE OUTLINE OF THESIS

There are total 7 chapters in this thesis. Chapter 1 gives an introduction to the current status of HDDs and future techniques proposed to extend the areal density beyond 1 Tbits/in^2. A review of high anisotropy $L1_0$ FePt is also given. Chapter 2 describes the experimental methods used in this thesis. An investigation on the composition effects of FePt is reported in the chapter 3. Nd, Mn and Rh doping effects on FePt are addressed and discussed in details in Chapter 4, 5 and 6, respectively. In Chapter 7, the conclusion is derived and the future work is also addressed.

II. EXPERIMENTAL METHODS

2.1 MAGNETRON SPUTTERING

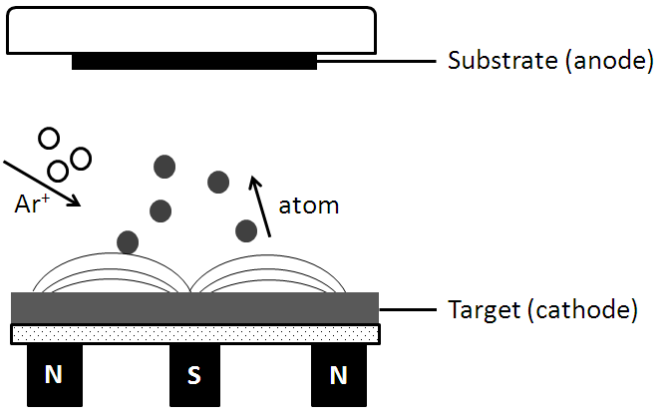

Fig. 5. An illustration of the magnetron sputtering process

As shown in Fig. 5, the sputtering system composes of a pair of planar electrodes. The top surface of the cathode is covered with a target material and the substrate is placed on the anode. Once the chamber is kept in sputtering gas (in this thesis using Ar) at a certain pressure and a voltage of several kilovolts is applied between the electrodes, the glow discharge is initiated. The charged plasma particle Ar ions then are accelerated towards the cathode to sputter the target, resulting in the deposition of thin film on the substrate. With the magnetic field as shown, the electrons proceed with helical path around the magnetic field line. The probability of collision of Ar with electron is enhanced. However, the stray field from the ferromagnetic materials will disturb the magnetic field. Therefore, the stronger permanent magnet should be used for the targets such as Fe or FePt.

Compared with other deposition methods such as chemical vaporizing deposition (CVD), the advantage of magnetron sputtering is that it can deposit most of materials including conducting metal, insulating materials, oxides and especially the high melting-point material.

Direct current (DC) and radio frequency (RF) magnetron sputtering can be used for sputtering where DC sputtering is for sputtering conducting materials. On the other hand, RF sputtering is used for insulating targets such as carbon and oxides to avoid accumulating surface charge.

In this thesis, the samples were deposited by magnetron co-sputtering of two or three elemental targets in a commercial sputter system (AJA International).

2.2 STRUCTURAL CHARACTERIZATION METHODS

2.2.1 X-RAY DIFFRACTION (XRD)

XRD is a non-destructive detection method to obtain the information about the crystallographic structure including phase, lattice constant, grain size and strain. The basic principle of XRD follows Bragg's law:

$$2d\sin\theta = n\lambda \ (n = 1, 2, 3, \dots) \tag{2-1}$$

Where d is the distance between two lattice planes; θ known as Bragg angle is a half of the angle between the incident and diffracted X-ray; n is the order of diffraction, λ represents the wavelength of the X-ray, Cu K_α with the wavelength of 1.54056Å is used for the normal XRD measurements in this thesis study.

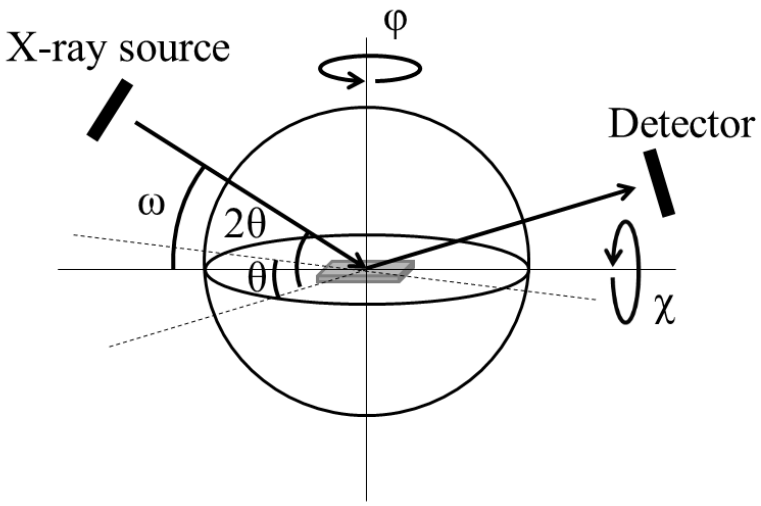

Fig. 6. An illustration of the XRD measurement and the definition of the angles used in the text, φ is the rotation axis in the normal direction of sampling placing, χ is the rotation axis in both sampling placing plane and diffraction plane.

An illustration of the XRD measurement is shown in Fig. 6. Here 2θ is the angle between the incident X-ray direction and the detector direction as shown. ω is the angle between incident X-ray direction and the sampling placing. φ is the rotation axis in the normal direction of sampling placing, χ is the rotation axis in both sampling placing plane and diffraction plane. Different methods of measurements will be described and discussed.

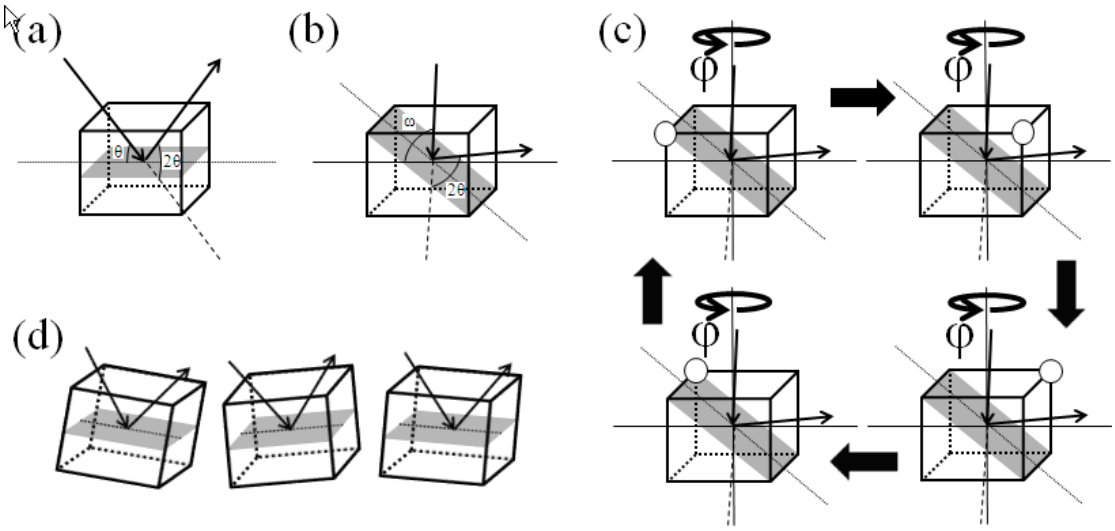

Fig. 7. XRD measuring configurations for (a) θ-2θ; (b) ω-2θ; (c) φ-scan and (d) Rocking curve (RC)

(i) θ-2θ measurement

The configuration is shown in Fig. 7a, here $\omega=\theta$ and θ varies consistently with the 2θ, which is the angle between the incident X-ray direction and the detector direction as shown. In this configuration, only the normal direction of lattice planes in the perpendicular direction will show the diffracted peaks.

(ii) ω-2θ measurement

The difference of ω-2θ from θ-2θ scans is that ω is not always equal to θ during measurement. A usual configuration can be seen in Fig. 7b. This configuration can give the information on the lattice planes which is not perpendicular with the sample surface.

(iii) φ-scan

Basing on ω-2θ scan, the φ-scan can be conducted by rotating the sample with respect to φ angle. The lattice symmetry can be derived from φ-scan, *e.g.* four-folded symmetry for tetragonal lattice as shown in Fig. 7c. Generally, the φ-scan may also involve the rotation of angle χ.

(iv) Rocking curve (RC)

By fixing 2θ, ω can be varied to conduct the ω scan, which is also known as the rocking curve scan. This can give the information about the texture of the orientation of grains as shown in Fig. 7d. Normally, the degree of texture can be represented by the Full Width at Half Maximum (FWHM) of the RC.

XRD can be incorporated with an oven to have the high temperature measurement, which is known as high temperature XRD (HTXRD). In HTXRD, the ambient temperature can be changed to high temperature in vacuum to have the *in-situ* study on the dynamic process such as phase transitions, crystallite growth, thermal expansion *etc.*. The vacuum can be pumped down to 10^{-5} Pa with a mechanical pump as fore pump and molecular pump as secondary pump. The temperature can be tuned from room temperature to the highest temperature at about 1100 ^{o}C. Utilizing this method, the temperature-dependent evolution of the crystallographic microstructure of sample can be derived.

2.2.2 X-RAY REFLECTIVITY (XRR)

XRR is a non-destructive detection method to obtain the information of thin film such as thickness, roughness, *etc.*. The crystal structure is not essential in this method. The specular geometry is usually used for XRR. Once the incident angle exceeds the total external reflection angle, the reflections from the top and the bottom surfaces of the film will interfere with each other and give the periodic interference. The period and the decrease of the amplitude directly related with the film thickness and the roughness [74],[75]. In this thesis, XRR was employed to investigate the thickness of single layer using the following equation [76]:

$$t = \frac{(m-n)\lambda/2}{\sqrt{\sin^2\theta_m - \sin^2\theta_c} - \sqrt{\sin^2\theta_n - \sin^2\theta_c}} \quad (2\text{-}2)$$

Where *m* and *n* are integers, represent the peak number from the critical angle for total reflection θ_c. θ_m and θ_n in angle correspond to the peak positions of peak *m* and *n*, respectively. (*m*-*n*) represents the number of period considered for calculation. A range of 12 periods were used for estimating the thicknesses in this thesis in order to minimize the error.

2.2.3 EXTENDED X-RAY ABSORPTION FINE STRUCTURE (EXAFS)

a. Basic principle

Extended X-ray absorption fine structure (EXAFS), ranged from ~ 50 to 1000eV above the absorption edge in the X-ray absorption spectroscopy (XAS), can yield the information about the local atomic environment around the absorbing atoms. The energy range above the absorption edge (~ 50eV), known as X-ray Absorption Near

Edge Structure (XANES), can give the information about the electronic properties of absorbing atoms. The origin of EXAFS signal may be explained as in the following: The core electron of the absorbing atom can be excited to a state above Fermi energy by X-ray. At above the absorption edge, the outgoing photoelectron with a certain kinetic energy will be scattered by surrounding atoms as shown in Fig. 8. The change of phase and magnitude with scattering depends on many factors such as elemental type, distance and thermal vibration. The scattered and outgoing photoelectron wave will interfere with each other constructively and destructively, which will be reflected in the X-ray absorption signal since the probability of emission is directly proportional to the absorption probability. The energy ranges for pre-edge, XANES and EXAFS are shown in Fig. 9.

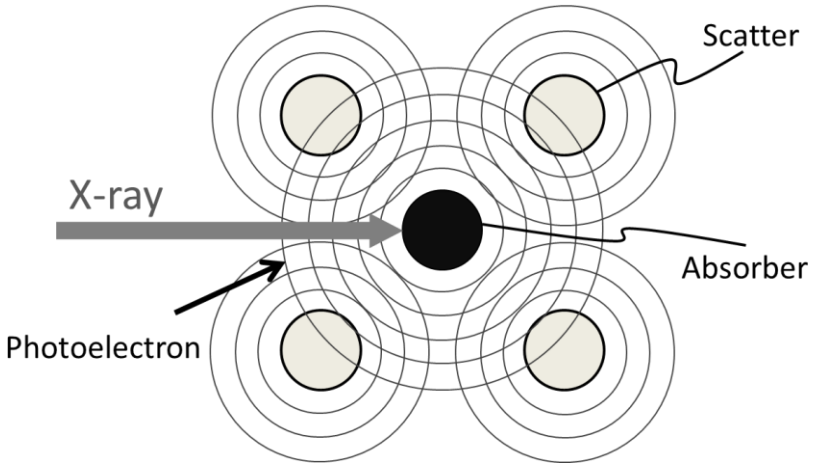

Fig. 8. Illustration of the basic principle of EXAFS

The equation used to analysis the EXAFS data is [77],[78]:

$$\chi(k)=\sum\chi_i(k)=\sum\frac{(N_iS_0^2)F_i(k)}{kR_i^2}\sin(2kR_i+\varphi_i(k))\exp(-2\sigma_i^2k^2)\exp(-2R_i/\lambda(k)) \qquad (2\text{-}3)$$

Where $R_i=R_0+\Delta R$, $k^2=2m_e(E-E_0)/\hbar$. R_0 (ΔR) is the initial (deviation of) path length. $F_i(k)$ is the effective scattering amplitude, $\varphi_i(k)$ is the effective scattering phase shift, $\lambda(k)$ is the mean free path, R_0 is the initial path length. Parameters needed for constructing models and will be determined from fittings are: N_i is the degeneracy of path, S_0^2 is the passive eletron reduction factor, E_0 is the energy shift, ΔR is the change in half-path length, σ_i^2 is the mean squared displacement. By constructing a proper model for the fitting, the local atomic environment of absorbing atom can be determined.

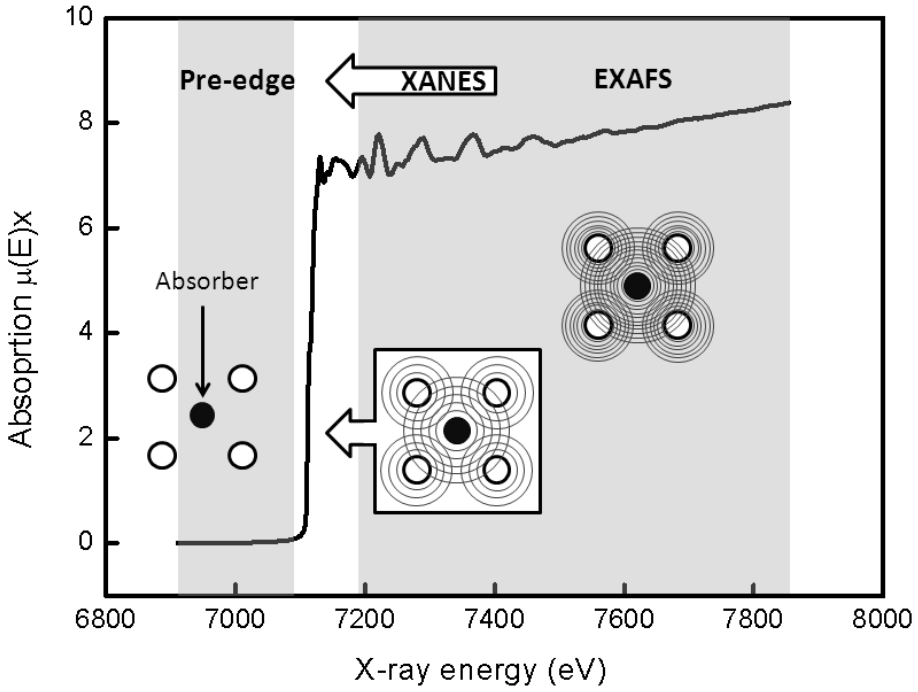

Fig. 9. An illustration of pre-edge, XANES, EXAFS ranges in the absorption spectra for Fe foil and their corresponding forward and backward photoelectron waves

The X-ray from synchrotron for EXAFS measurements is linear polarized in the horizontal plane. Due to this property, we carried two measurements with electric field of X-ray (E) perpendicular ($\perp$) and parallel ($\parallel$) with the (001) plane of sample surface for each edge. The reason is that the atoms with radial vectors perpendicular to E vector may not contribute to the EXAFS signal. Two directional measurements are very help in determining the local atomic environment for anisotropic system like $L1_0$ FePt.

It should be noted that the above discussion only considers the simplest case of scattering with single path scattering. The analysis of EXAFS from experiment should also consider the multiple scattering. The multiple scattering corresponds to the scattering paths containing one or several bounces off one or more intermediate atoms. It would overlap with the signal from the single path scattering and make the analysis more complicated. In particular, its contribution to the EXAFS would be important if the scattering angle is 0^o or 180^o. Normally, the multiple scattering only exists beyond the path length of first shell.

b. EXAFS data reduction

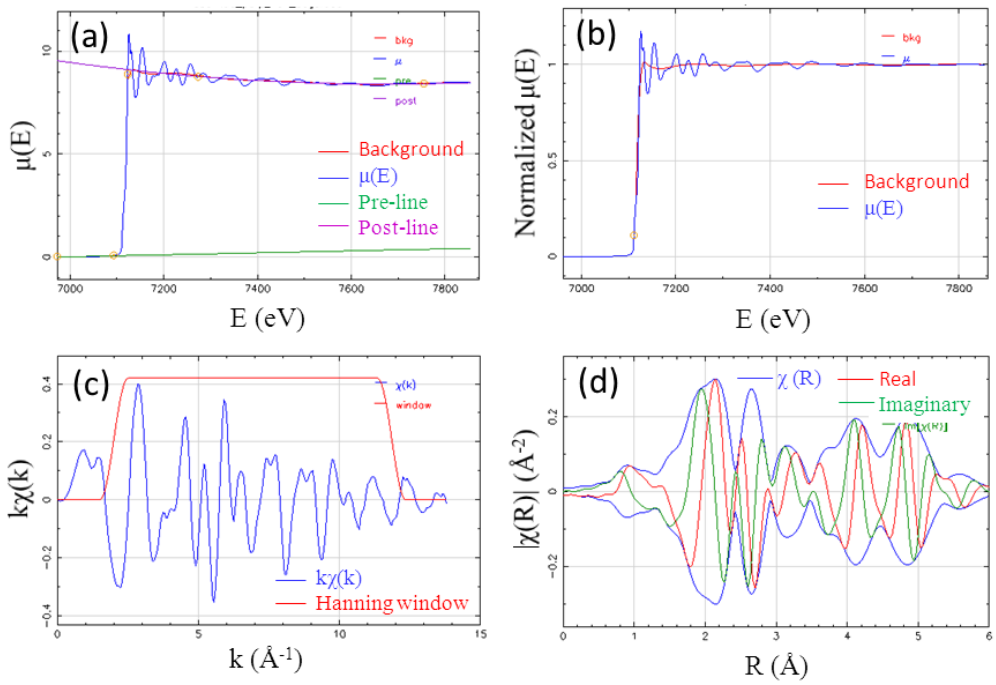

Fig. 10. An analysis example of (a) raw date $\mu(E)$ (pre edge line, post edge line and background are also shown); (b) nolmalizated data $\mu(E)$; (c) $\chi(k)$ in k space (Hanning window for Fourior transformation is also shown) and (d) $\chi(R)$ consisting of real and imaginary parts in R space.

Normalization was conducted with the standard process by choosing proper pre-edge line, post-edge line and edge step [79]. The isolation of the signal only from the local atomic environment normally can be performed by using the following equation [80]:

$$\chi(E) = \frac{\mu(E) - \mu_0(E)}{\Delta\mu} \tag{2-4}$$

Where μ(E) is the raw data while μ_0(E) is the background which needs to be removed. $\Delta\mu$ is the edge step, which should be 1 for the normalized data. Normally, the background is simulated with a spline line containing evenly distributed knots. The number of knots can be determined by the parameter R_{bkg} and Δk with the equation $2 \cdot R_{bkg} \cdot \Delta k/\pi+1$. Δk is the k range in k space used for Fourior transformation. The $\chi(k)$ in k space can be derived from $\chi(E)$ in E space with the equation $k = \frac{\sqrt{2m(E-E_0)}}{\hbar}$. After Fourior transformation, $\chi(R)$ is derived. An illustration of the data processing in different spaces are shown in Fig. 10. The choice of R_{bkg} is used to cut off the unrealistic signal below R_{bkg}, which corresponds to eliminating the low frequency ossicilation originating from the noise in k space. Δk corresponds to the k-range of data filtered by the Haning window as shown in Fig. 10c for the Fourior transformation. By choosing proper Δk and R_{bkg}, the number of knots can be determined and the noise from the measurement can be minimized and the signal from only the local atomic environment is isolated. In this thesis, the Δk and R_{bkg} of 9 and 1.6 with knots of 8 were chosen for isolating the signal from the local atomic environment, respectively. Further analysis based on comparing $\chi(R)$ with the theoretical $\chi_{cal}(R)$ calculated from the assumed model with FEFF [81] to have the best fit.

2.3 MAGNETIC PROPERTY CHARACTERIZATION METHODS

2.3.1 VIBRATING SAMPLE MAGNETOMETER (VSM)

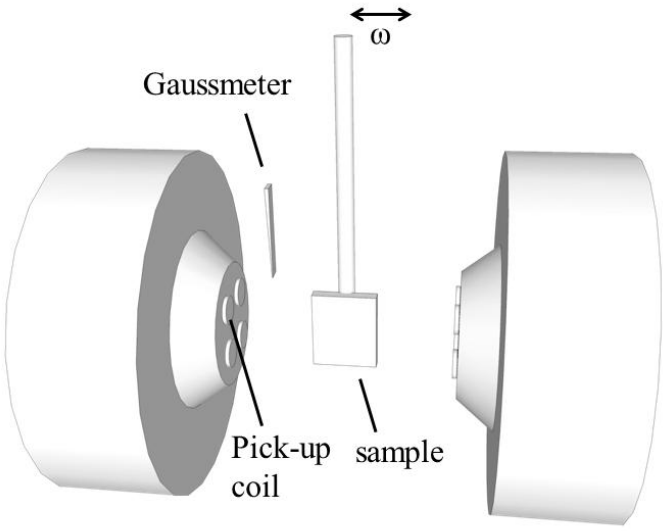

Fig. 11. An illustration of VSM measurement configuration

VSM is widely used for measuring magnetic properties. In the process of measurement, a sample is placed in a uniform magnetic field produced by electromagnet to magnetize it. At the same time, the sample is physically vibrated in sinusoidal motion with the frequency of ω as shown in Fig. 11, typically through the use of a piezoelectric material. Due to this vibration, the magnetic flux through the pickup coils varies sinusoidally. This will then result in the induced voltage in the coil which is proportional to the magnetic moment of the sample. The magnetic field at

the electromagnet gap may be measured with a Gauss meter simultaneously. By plotting the obtained magnetic moment versus magnetic field, the hysteresis loop may be obtained.

Currently, a study stated that finite size has effect on the moment calibration of VSM [82]. The reason is that the voltage induced in the pick-up coils depends not only on the magnetic moment of the sample, but also on its size and the distance from pick-up coils. In order to avoid this issue, a Nickel strip with the similar shape to our sample was used for calibrating magnetic moments every time before measurement. This will give accurate information about magnetic moment for comparison.

2.3.2 MAGNETIC FORCE MICROSCOPY (MFM)

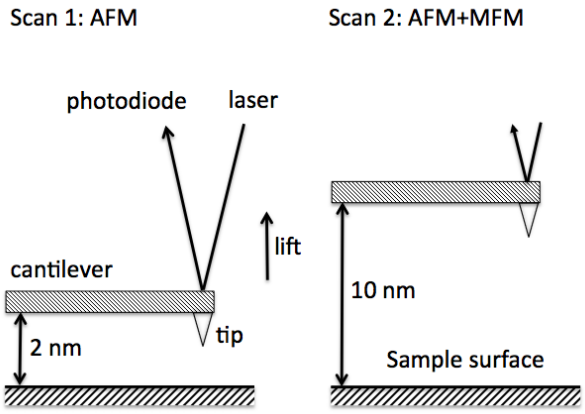

Fig. 12. An illustration of MFM measurements configuration [34]

MFM is a variety of atomic force microscopy (AFM) and can be used to measure the surface domain structure of magnetic sample. It consists of a flexible cantilever and a tiny magnetized tip mounting on the free end as sown in Fig. 12. In this thesis,

tapping mode was used for operation. During operating, the cantilever is oscillated at its fundamental resonance frequency. When the tip has a force interacting with the sample surface, the amplitude, phase as well as frequency will be affected. These changes can then be detected and used for determining the force between the tip and sample surface. The resolution of MFM is highly related to the lift scan height (LSH) and the properties of the tip including the tip size and its material. Generally, the smaller LSH can give the higher resolution. However, when LSH is smaller than 10nm, van der Waals forces, electrostatic forces, Casimir forces, *etc.* will overlap the magnetic force signal. For the experiments in this thesis, each line was scanned twice as shown in Fig. 12. LSH was 2 nm and 10 nm for the first and second scan, respectively. After the two scans, the magnetic domain image, originating from the interaction with the stray field from the surface of magnetized sample, was obtained by subtracting the topographic image (AFM) from the overlapped AFM+MFM image.

2.3.3 SUPER CONDUCTING QUANTUM INTERFERENCE DEVICES (SQUID)

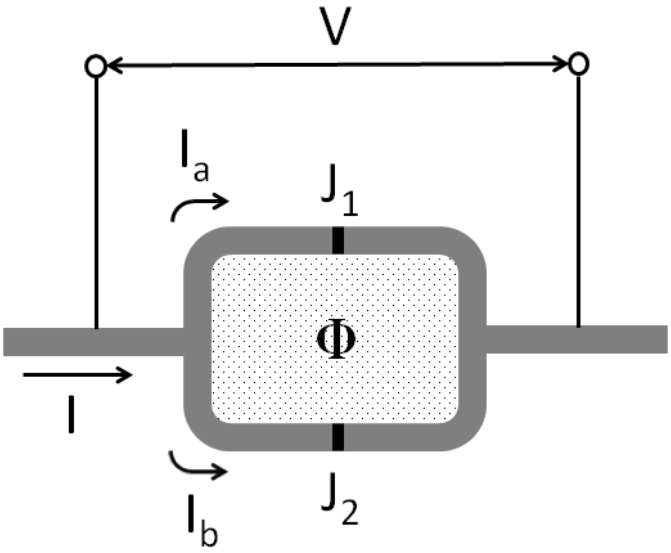

Fig. 13. An illustration of the principle of DC SQUID

SQUID has been widely used as a highly sensitive magnetometer due to its high sensitivity of around 10^{-10} to 10^{-15} Tesla. The key part in this device is a superconducting loop containing Josephson junctions. SQUID generally can be divided into two types: DC SQUID and RF SQUID. In RF SQUID, there is only one Josephson junction. The sensitivity of this type is relative lower. The basic principle of DC SQUID can be seen in Fig. 13. The DC SQUID is mainly due to Josephson effect and magnetic flux quantization. Josephson effect describes the quantum tunneling effect between two superconductors separated with a several angstrom thick insulator. This can be described with two equations:

$$\mathrm{U(t)} = \frac{\hbar}{2e}\frac{\partial \phi}{\partial t} \tag{2-5}$$

$$\mathrm{I(t)} = I_c \sin(\phi(t)) \tag{2-6}$$

Where U(t) and I(t) are voltage and current respectively. ϕ(t) is the phase difference of the two wave functions between two superconductors. I_c is the critical current, which is temperature and magnetic field dependent. The voltage occurs once the current exceeds I_c. Magnetic flux quantum $\Phi_0 = \frac{\hbar}{2e}$ (~2×10^{-15} Wb) here indicates the sensitivity of SQUID. As shown in Fig. 13, there are two Josephson junctions (J_1 and J_2) paralleled in a superconducting loop. Due to the magnetic flux quantization, which means only integral multiples of Φ_0 can get through the loop, screening current I_s occurs to either screen the magnetic flux > $n\Phi_0$ & < $(n+1/2)\Phi_0$ to maintain $n\Phi_0$ or >$(n+1/2)\Phi_0$ &< $(n+1)\Phi_0$ to maintain $(n+1)\Phi_0$. Since the superconducting current is constant and equals to the sum of I_s and I_c, thus I_s as well as I_c are the periodic function of magnetic flux with a period of Φ_0. The magnetic flux and electrical signal can then be related together at a very high resolution.

2.3.4 X-RAY MAGNETIC CIRCULAR DICHROISM (XMCD)

a. Right/left polarized X-ray from synchrotron radiation

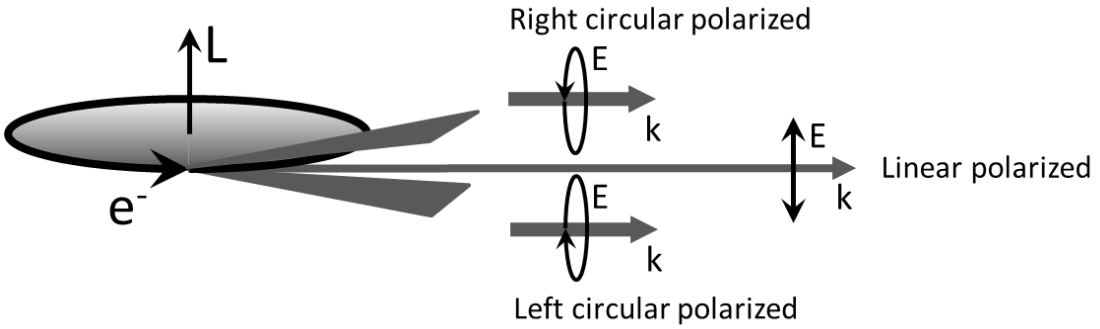

Fig. 14. The origin of polarized synchrotron radiation from a bending magnet source (Courtesy of J. Stohr [83])

In synchrotron radiation, electrons are accelerated in a circle and possess an angular momentum *L*. Both angular momentum and energy can be transferred from the accelerated electrons to the emitted photons. As shown in Fig. 14, the emitted X-ray from the same plane as the electron orbit will have $L_z = 0$. L_z is projection of angular momentum in z direction. This will give a linear polarized X-ray. If the emitted X-ray is from the emission direction below the electron orbit, it will possess L_z = -h and give a left circular polarized X-ray. Correspondingly, The emitted X-ray from the emission direction above the electron orbit will possess L_z = h and give a right circular polarized X-ray.

b. Basic principle of XMCD

XMCD is a good choice to measure magnetic properties as well as the electronic structure of element in complex system due to its element-specific and shell-selective properties [84]. The XMCD effect, originating from the difference of transition probabilities with left and right circular polarized X-rays taken in a magnetic field, is directly related to the atomic magnetic moment. As shown in Fig. 15, the absorption intensities at the L_3 and L_2 edges are related to the transitions from the $2p_{3/2}$ and $2p_{l/2}$ into the empty 3d bands by following the charge sum rule, which links the measured

averaged X-ray absorption resonance intensity of a core to valence transition to the number of empty valence states N_h per atom.

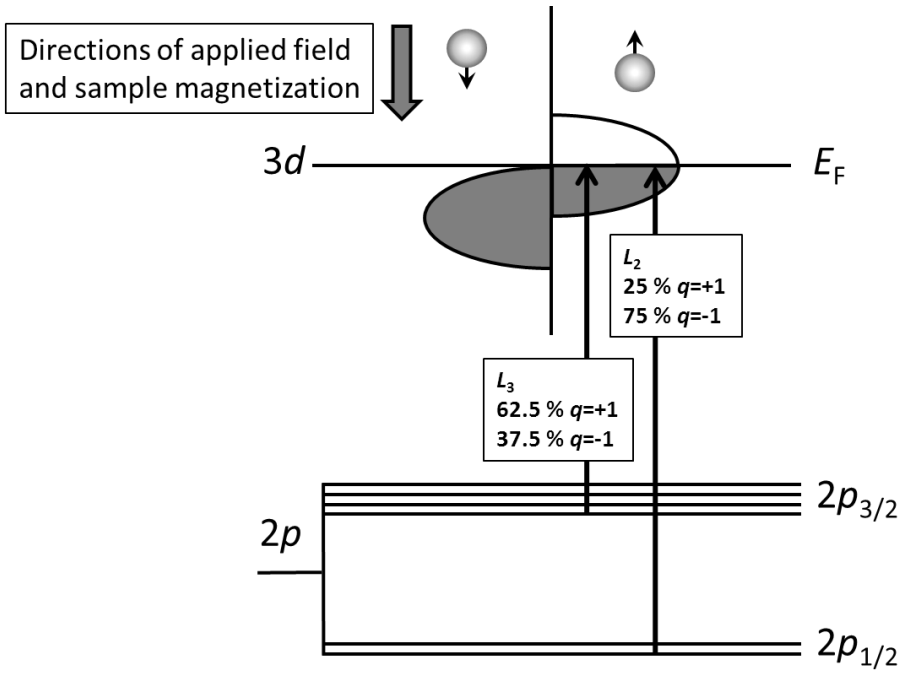

Fig. 15. The L-edge X-ray absorption processes of circularly polarized photons with angular momentum q = ±1 (in units of $\hbar$) to illustrate the origin of XMCD effect (Courtesy of J. Stohr [83])

The sum rule usually is used to derive the elemental spin and orbital magnetic moments from the detected XMCD spectra. The general form of sum rule has been given in the previous studies [85],[86]:

$$\frac{\int_{j_+ + j_-} d\omega(\mu^+ - \mu^-)}{\int_{j_+ + j_-} d\omega(\mu^+ + \mu^- + \mu^0)} = \frac{1}{2}\frac{l(l+1)+2-c(c+1)}{l(l+1)(4l+2-n)}\langle L_z \rangle \quad (2\text{-}7)$$

$$\frac{\int_{j+} d\omega(\mu^+ - \mu^-) - \left[\frac{c+1}{c}\right]\int_{j-} d\omega(\mu^+ - \mu^-)}{\int_{j+j-} d\omega(\mu^+ + \mu^- + \mu^0)} =$$

$$\frac{l(l+1)-2-c(c+1)}{3c(4l+2-n)}\langle S_z\rangle + \frac{l(l+1)[l(l+1)+2c(c+1)+4]-3(c-1)^2(c+2)^2}{6lc(l+1)(4l+2-n)}\langle T_z\rangle \quad (2\text{-}8)$$

Where μ is the absorption coefficient, + (-) denotes right (left) circular polarized signal, 0 denotes white line, *c* (excited state) and *l* (ground state) are the azimuthal quantum number. $<L_z>$, $<S_z>$ and $<T_z>$ represent orbital angular momentum operator, spin operator and magnetic dipole operator, respectively.

The detailed application of sum rule in XMCD analysis will be described in the individual part in this thesis since its exact form for different transition in different element is different. In this thesis, the cases for Fe 2p-3d and Nd 4f-5d transitions will be discussed in details.

c. XMCD data reduction

The raw data consisting of absorption sepectra measured with both left and right circular polarized X-rays is shown in Fig. 16a. In order to derive the spin and orbital moments from XMCD spectra, a reduction of XMCD data is needed from each analysis. Firstly, the normalization is done by making the baseline flat and aligning it at y = 0. The white line is deived by averaging the spectra measured from both left and right circular polarized X-ray as shown in Fig. 16b. A step-like line [87] is used to substract the background as shown in Fig. 16c to determine the integrated intensity of XAS. Further by integrating the XMCD spectra, the spin and orbital moments can be calculated from the sum rules [85],[86].

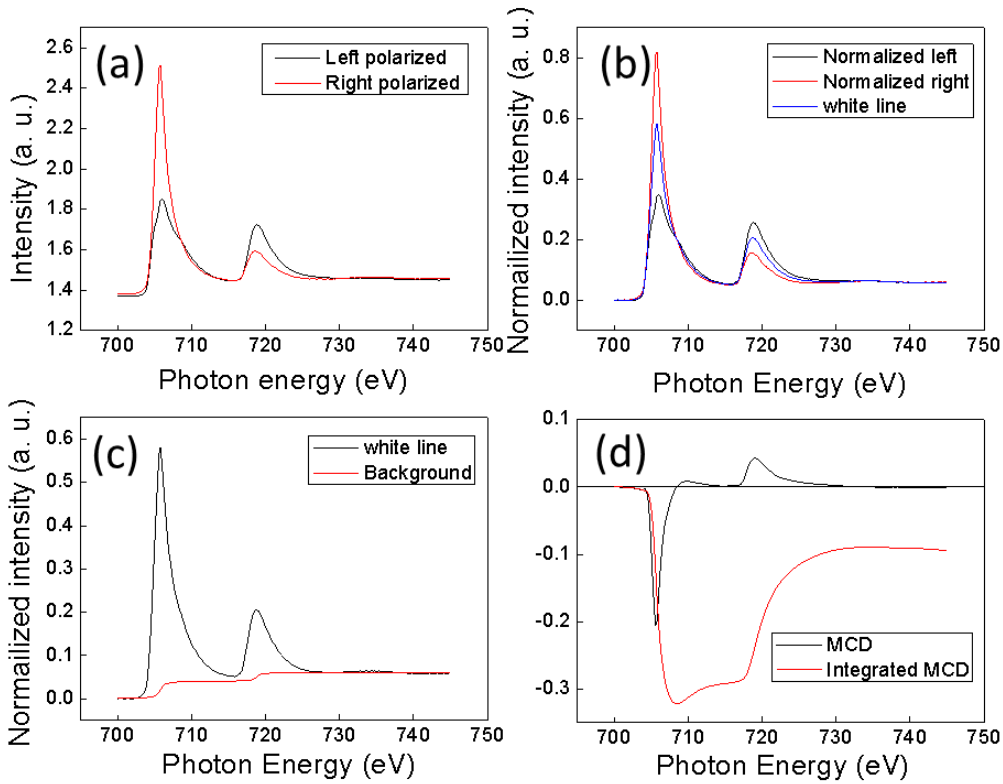

Fig. 16. The analysis example of (a) raw date; (b) nolmalizated data; (c) background substraction with step-like background and (d) integrating the MCD spectra with photon energy

III. THE INVESTIGATION OF FEPT AND ITS COMPOSITIONAL EFFECTS

3.1 FEPT AND ITS COMPOSITIONAL EFFECTS AT ROOM TEMPERATURE

3.1.1 EXPERIMENTAL METHODS

FePt films were directly deposited onto single crystal MgO (001) substrates at the substrate temperature of 550 ^{o}C by co-sputtering the elemental targets. Here a series of Fe_xPt_{100-x} thin films with different Fe compositions (40, 45, 50, 55, 60 at. %) was investigated. The MgO substrates, which were pre-cleaned by using acetone, alcohol and de-ionized water sequentially, were held at the above specified temperature for 20 min prior to deposition. After that, relatively low deposition rate 0.2 ~ 0.5 Å/s was used. The thickness of each film was fixed to 50 nm by adjusting the deposition time from the measured deposition rate. The base pressure before deposition and the Ar gas pressure during deposition were 3 ~ 9×10^{-8} Torr and 15 mTorr, respectively. The compositions of these films were controlled by adjusting the deposition power with previously measured deposition rate and final compositions were measured by energy-dispersive x-ray spectroscope (EDX).

Structural properties were measured by using x-ray diffraction (XRD) with a Cu-K_α radiation. Vibrating sample magnetometer (VSM) and super-conducting quantum interference devices (SQUID) were used to measure the in-plane and

out-of-plane hysteresis loops to determine the magnetic properties such as M_s, H_c and K_u at room temperature and the elevated temperatures.

3.1.2 ORDERING PARAMETER AND LATTICE PARAMETER DETERMINATION

One important parameter that can be calculated from XRD spectrum is long-range chemical ordering parameter *S*. *S* represents the probability of correct site occupation in the $L1_0$ phase. The maximum ordering parameter for a given film composition is given by $S_{max} = 1-2\Delta x$, where Δx is the compositional deviation in atomic fraction from the equiatomic composition. In fully ordered $L1_0$ (FCT) FePt, $\Delta x = 0$ and $y_\alpha = y_\beta = 0.5$. However, if $\Delta x \neq 0$ and $x_A < x_B$ are assumed, $x_A = 1-x_B = 0.5-\Delta x$, then $r_\alpha = x_A/y_\alpha = 1-\Delta x/0.5$, thus $S = (r_\alpha - x_A)/ y_\beta = 1-2\Delta x$ [34].

Ordering parameter *S* can be derived by taking the ratio of the integrated intensities of (001) and (002) peaks in θ-2θ scan as follows,

$$\frac{I_{(001)}}{I_{(002)}} = \frac{F^2_{(001)}(LPe^{-2M})_{(001)}}{F^2_{(002)}(LPe^{-2M})_{(002)}} \tag{3-1}$$

Where *I* is the total integrated intensity of the given peak and obtained by multiplying the integrated intensity obtained from the θ-2θ scan by the full width at half maximum (FWHW) of its corresponding rocking curve. The absorption correction due to the attenuation of X-ray in the film was realized by using the correction factor $[1-\exp(-2\mu \times t)/\sin\theta]$ to multiply with the total integrated intensities, where μ is the weighted averaging linear absorption coefficient, *t* is the film thickness, and θ is the Bragg angle of the given reflection [54]. *F* is the structure factor and is given by *F*

= $4(x_A f_A + x_B f_B)$ for the fundamental peaks, here (002), and $F = 2 \cdot S(f_A - f_B)$ for the superlattice peaks, here (001) or (003), where x_A and x_B are mole fractions of the chemical species Fe and Pt, respectively. f_A and f_B are the atomic form factors for the given species and reflection. L and P are the Lorentz factor and polarization factor, respectively. M is the Debye-Waller factor, $M = (Q\sigma)^2/2$, where σ is displacement amplitude and $Q = (4\pi/\lambda)\sin\theta$ is the scattering factor for wavelength λ and Bragg angle θ. It was demonstrated that σ is less than 0.02 nm [88] and a typical value of 0.014 nm from experiment was used in this measurement [89]. The calculation details can be found in the book of Cebollada *et al.* [34]. The ordering parameter S calculated for $L1_0$ Fe_xPt_{100-x} was shown in Table 3. The table also lists the lattice parameter c and whether the in-plane c variant is present or not. Here the presence of in-plane c variant means that the c-axis is in the film plane rather than perpendicular to the film plane, which also resulted in the presence of the (200) or (020) peaks in θ-2θ scans.

In order to improve the accuracy of lattice constant determination, Nelson-Riley function was used to describe the systematic error [90].Therefore, the Bragg condition for a tetragonal lattice may be expressed by the following equation,

$$\sin^2\theta = A(k^2 + h^2) + Bl^2 + C\left\{10\sin^2 2\theta\left(\frac{1}{\sin\theta} + \frac{1}{\theta}\right)\right\} \qquad (3\text{-}2)$$

Where $A = \lambda^2/4a^2$, $B = \lambda^2/4c^2$ and C = constant. θ for respective plane index (hkl) can be obtained from the XRD θ-2θ results.

3.1.3 M_S AND K_U DETERMINATION FROM HYSTERESIS LOOPS

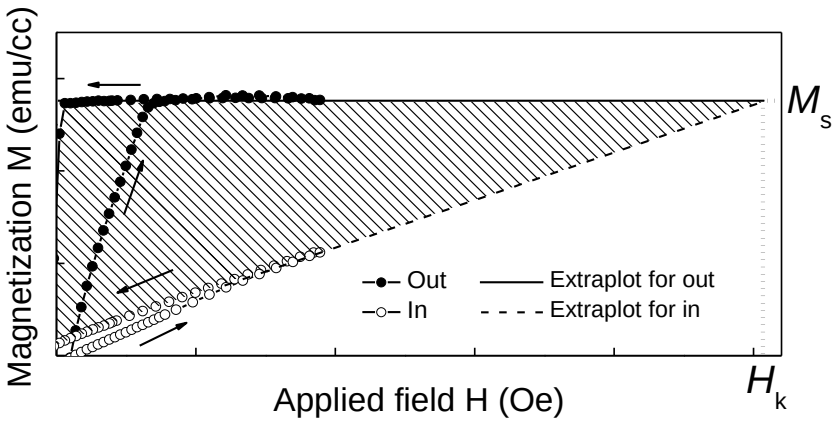

Fig. 17. An illustration of K_u determination from out-of-plane (out) and in-plane (in) hysteresis loops

The out-of-plane and in-plane *M-H* curves in the first quadrant are shown in Fig. 17. M_s was taken from the average value of the saturation part of out-of-plane magnetization curve where the magnetization curve became flat at high field (*i. e.* saturation) as shown in Fig. 17. The value of K_u was evaluated by taking the area enclosed between the in-plane and the out-of-plane magnetization curves in the first quadrant of *M-H* loops when the film was saturated in both directions. In this thesis, the in-plane hysteresis loops were not fully saturated for some cases. Therefore the saturation field of the in-plane was obtained by extrapolating the in-plane and the out-of-plane hysteresis loops corresponding to the anisotropy field H_k as shown in Fig. 17. Then K_u was calculated by using this equation

$$K_u = K_{eff} + 2\pi M_s^2 \tag{3-3}$$

Where $K_{eff} = \frac{1}{2} H_k M_s$, $2\pi M_s^2$ represents the demagnetization energy.

3.1.4 GROWTH OF $L1_0$ (001) Fe_xPt_{100-x} EPITAXIAL FILMS

In this experiment, single crystal MgO with the surface plane of (001) was used as the substrate to realize epitaxial growth of $L1_0$ FePt. The epitaxial growth relation was investigated by measuring the φ-scans of the substrate and FePt film. φ -scan for $L1_0$ $Fe_{50}Pt_{50}$ {112} planes illustrated in Fig. 18 showed a 4-fold symmetry and coincided with the 4-fold peaks for MgO {224} planes. Therefore, it can be inferred that the relation for epitaxial growth was MgO (001) <100> // $L1_0$ FePt (001) <100>.

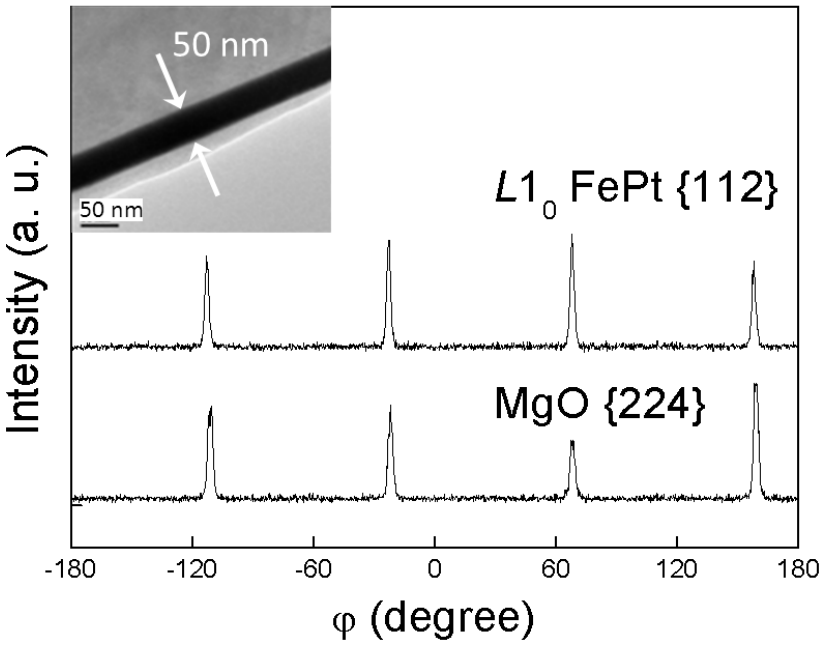

Fig. 18. φ-scans for {112} planes of $L1_0$ $Fe_{50}Pt_{50}$ film and {224} planes of MgO substrate. Inset shows that the film with uniform thickness of 50 nm was formed

3.1.5 CRYSTALLOGRAPHIC STRUCTURE

The θ-2θ scans for $L1_0$ Fe_xPt_{100-x} with the nominal compositions x = 40, 45, 50, 55, 60 at. % are shown in Fig. 19. The compositions of these films were then confirmed by EDX attached in the scanning electron microscope (SEM). EDX results

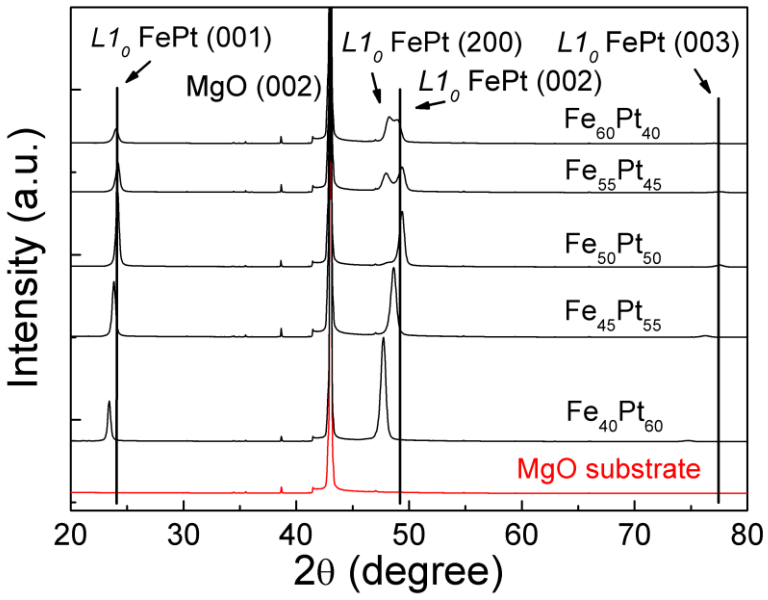

Fig. 19. XRD θ-2θ spectrum of Fe_xPt_{1-x} with x = 40, 45, 50, 55, 60 at. % and single crystal MgO substrate

showed that x = 38.3, 47.7, 49.7, 57.9, 62.7 at. %, respectively. Considering that the accuracy of EDX from SEM is ± 5 at. %, these values were consistent with the nominal compositions. Here nominal composition was used as the notation of composition. The full width at half maximum (FWHM) of rocking curves for fundamental peaks (002) were all around 0.8^{o} (Table 3), which were comparable to that of the high quality molecular beam epitaxial (MBE) grown films reported in the literature [91]. Therefore, (001) texture had been obtained in these thin films. In Fig. 19, clear superlattice peaks (001) and (003) could be found for all films and they were indicative of the presence of the long-range chemically ordered $L1_0$ phase in the films. Consequently, this indicated that chemically ordered $L1_0$ FePt films with good (001) texture were epitaxially grown on (001) single crystal MgO substrates.

It should be noted that in Fig. 19, $L1_0$ FePt (200) peaks began emerging when Fe content exceeded 50 at. %. At the same time, the intensities of (001), (002) and (003) peaks began to decrease. It indicated that the excess Fe content would deteriorate the epitaxial growth and cause the presence of in-plane *c* variant. Furthermore, it was found that the (001), (002) and (003) peaks shifted to higher angle with increase of Fe content. The lattice parameter *c* with different Fe contents were calculated by using equation 3-2 and shown in Table 3. Lattice parameter *c* decreased significantly from 3.812 Å to 3.692 Å with Fe content increasing from 40 at. % to 50 at. %. Further increasing of Fe content to 60 at. % resulted in slight increase of the lattice parameter *c*. As in $L1_0$ structure, lattice parameter *c* was smaller than that in FCC structure. The

atomic radius of Pt atom was larger than that of Fe atom. Therefore the decrease of the lattice parameter *c* may be related to the increase of chemical ordering and decrease of Pt content. The subsequently slight increase in lattice parameter *c* may be attributed to the decrease of the chemical ordering as shown in Table 3.

The full width at half maximum (FWHM) of the rocking curves for the (001) and (002) reflections, the measured and maximum ordering parameters, *S* and S_{max}, respectively, and whether in-plane *c*-axis variants were present or not are listed in Table 3. As can be seen, the ordering parameter *S* as high as 0.929 was obtained at the composition of $Fe_{50}Pt_{50}$. When the concentration of Fe increased from 40 at. % to 60

Table 3. The full width at half maximum (ω_{50}) of the rocking curves for the (001) and (002), the measured and maximum ordering parameters, *S* and S_{max}, respectively, the lattice parameter *c* and whether in-plane *c* variant presents or not for Fe_xPt_{100-x}

Composition	ω_{50}**(001)**	ω_{50}**(002)**	S_{max}	***S***	***c*(Å)**	**In-plane *c***
$Fe_{40}Pt_{60}$	1.160 ^{o}	0.701 ^{o}	0.8	0.61	3.812	No
$Fe_{45}Pt_{55}$	1.305 ^{o}	0.894 ^{o}	0.9	0.78	3.747	No
$Fe_{50}Pt_{50}$	1.174 ^{o}	0.861 ^{o}	1	0.92	3.692	No
$Fe_{55}Pt_{45}$	1.784 ^{o}	1.126 ^{o}	0.9	0.88	3.695	Yes
$Fe_{60}Pt_{40}$	1.335 ^{o}	0.884 ^{o}	0.8	0.65	3.719	Yes

at. %, *S* increased and then decreased, and the highest value was found at Fe 50 at. %. This was consistent with the results of VSM, which will be discussed in the following sections. At Fe 55 at. %, *S* decreased slowly, suggesting that excess Pt had a greater effect in deteriorating the chemical ordering than excess Fe.

3.1.6 MAGNETIC PROPERTIES AT ROOM TEMPERATURE

Both in-plane and out-of-plane hysteresis loops measured using VSM at room temperature with maximum applied field of 20 kOe are shown in Fig. 20. When the Fe content was 50 at. % and below, the film showed a good perpendicular anisotropy. With Fe content increased to 55 at. %, in-plane coercivity was larger than out-of-plane coercivity. This increase in the in-plane coercivity was mainly due to the presence of in-plane c variant. Further increasing of Fe content up to 60 at. % resulted in isotropic property due to the increase of the in-plane *c* variant.

For $Fe_{50}Pt_{50}$, M_s was 1158 emu/cc, which was consistent with the bulk value 1140 emu/cc reported by Klemmer *et al.* [31]. The M_s increased first and then decreased with Fe concentration. The highest value could be obtained in the film with Fe composition of 50 at. %. The first increase in M_s with Fe concentration was due to larger magnetic moment of Fe atom (2.9 μ_B/atom) comparing with induced magnetic moment of Pt atom (0.3 μ_B/atom) by the Fe-Pt hybridization [92]. The reason for the further decrease of M_s with Fe concentration larger than 50 at. % was not clear.

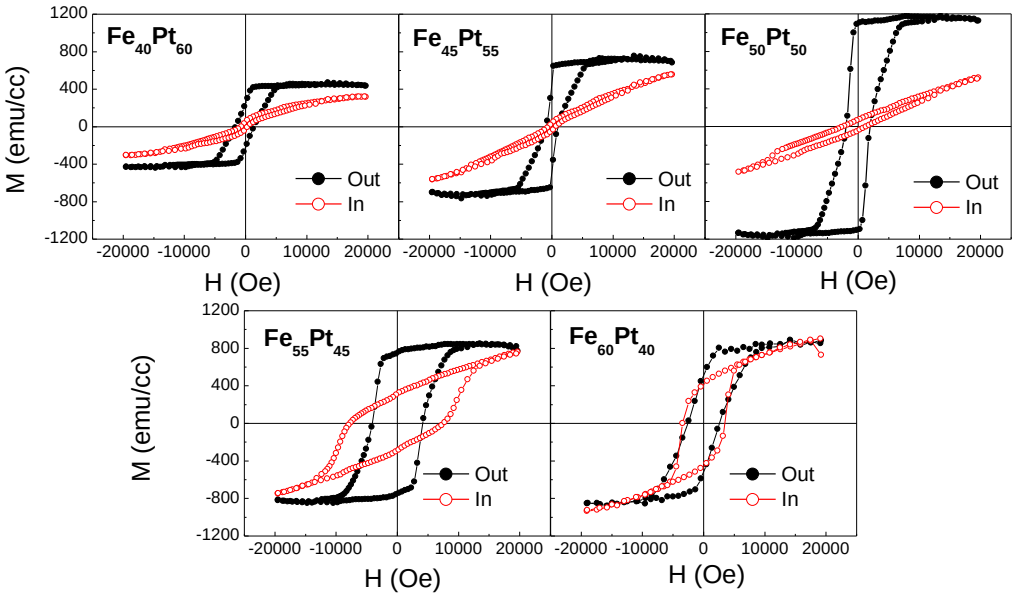

Fig. 20. In-plane and out-of-plane hysteresis loops for (a) Fe_xPt_{100-x} (x = 40, 45, 50, 55 and 60 at. %) measured with VSM at room temperature.

3.2 STATIC THERMAL INVESTIGATION ON FE_XPT_{100-X}

In order to investigate the temperature-dependent magnetic properties such as M_s and K_u, the SQUID was utilized to measure the in-plane and out-of-plane hysteresis loops at elevated temperature from 300 K to 750 K for every 50 K. The temperature-dependent saturation magnetization (M_s) for different Fe concentrations is shown in Fig. 21a. From this figure, it can be seen that the saturation magnetization decreased monotonically with temperature. Curie temperature is defined as the temperature where M_s approaching zero. Thus the Curie temperature with various Fe

concentrations could be obtained and shown in Fig. 21b. It showed that the highest Curie temperature could probably be achieved at the Fe concentration between 50 at. % and 55 at. %. The Curie temperature of $Fe_{50}Pt_{50}$ was around 750 K, which was very close to the bulk value 753 K [32]. When the concentration of Fe increased from 50 at. % to 60 at. %, T_C began to decrease. The reason for this decrease was that the ordering degree underwent a significant decrease from 50 at. % to 60 at. % as shown in Table 3. The decrease of ordering degree would deteriorate the Fe-Fe exchange interaction. It also could be seen that excess Pt had more effect in decreasing T_C than excess Fe, which was due to the fact that occupation of excess Pt atoms on Fe site would reduce the exchange interaction in the Fe atomic planes.

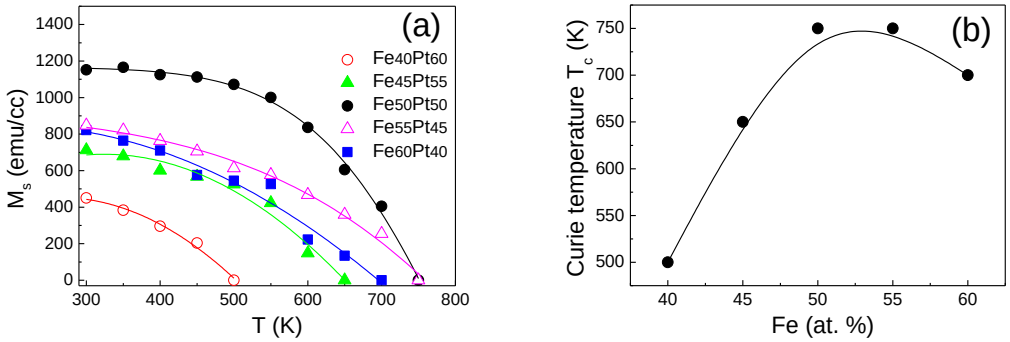

Fig. 21. (a) M_s of Fe_xPt_{100-x} films with the temperature varying from 300 K to 750 K (b) T_C with various Fe concentrations in Fe_xPt_{100-x}. The fitting lines are drawn to guide the eye.

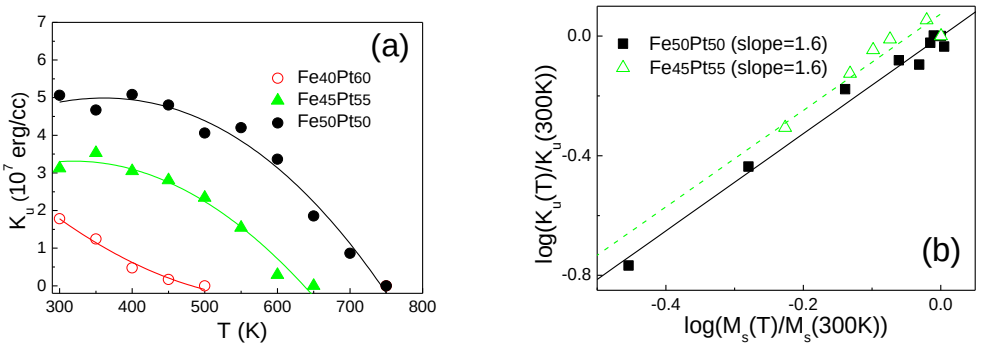

Fig. 22. (a) K_u of Fe_xPt_{100-x} with the temperature varying from 300 K to 750 K (b) Plots of $\log(K_u(T)/K_u(300\ K))$-$\log(M_s(T)/M_s(300\ K))$. The fitting lines are drawn to guide the eye

Fig. 22a shows the change of anisotropy K_u with temperature for Fe_xPt_{100-x} (x = 40, 45, 50 at. %). The K_u of $Fe_{55}Pt_{45}$ and $Fe_{60}Pt_{40}$ were not calculated due to the presence of in-plane *c* variant. Compared to M_s, the anisotropy K_u decreased faster with temperature. From a numerical fit of this data according to:

$$K(T)/K(300K) = [M_s(T)/M_s(300K)]^n \qquad (3\text{-}4)$$

A value of n ≈ 1.6 was obtained for $Fe_{45}Pt_{55}$ and $Fe_{50}Pt_{50}$ over a large temperature range as shown in Fig. 22b. Here $Fe_{40}Pt_{60}$ film was not used for fitting due to likely uncertainty caused by the small temperature range.

The temperature-dependent anisotropy for simple pure ferromagnets such as Gd (Uniaxial) and Fe (Cubic) follows the Callen-Callen theory [37],[93]:

$$K(T)/K(0) = [M_s(T)/M_s(0)]^n \quad (3\text{-}5)$$

Here $n = l(l+1)/2$, l is the order of the spherical harmonics describing the angular dependence of the local anisotropy (l=2 for uniaxial, l=4 for cubic). This theory is based on simple spin disorder model where both temperature-dependent anisotropy and spontaneous magnetization are due to that the magnetization is thermally distributed over a small angle range about some direction on the energy surface. Therefore, the temperature dependence of the anisotropy in this model is related to the symmetry of the anisotropy energy surface. The sharper the curvature of the energy surface, the higher value of *n*. However, in this thesis, a value of around 1.6 was found for *n*. Some works also showed that an approximate exponential value of 2 was found for $L1_0$ FePt with uniaxial anisotropy [38]. There are two possible reasons. One is that the magnetic moments in $L1_0$ FePt are itinerant, but the Callen-Callen relation is only quite suitable for localized moments. For pure transition metals where magnetic moments are less well localized, it is only partially successful. The other reason may be related to the alternatively stacking of two atomic layers. The anisotropy in this structure is due to an ion-ion anisotropic exchange interaction, thus its temperature-dependent anisotropy is not just simply due to the thermal disturbance of magnetization. Furthermore, based on its unusual structure, simulation work implied that there existed in-plane anisotropy and the change of *n* was due to the competition between the easy-axis anisotropy and in-plane anisotropy when considering the temperature effects [40]. Though several simulations managed to

interpret this phenomenon [39],[40], the origin of anisotropy in $L1_0$ FePt and its temperature-dependence are still not fully understood. Therefore, a detailed physical model is needed for better understanding and controlling of the temperature-dependent anisotropy in $L1_0$ FePt.

3.3 DYNAMICAL THERMAL INVESTIGATION OF FEPT HAMR MEDIA DURING LASER PULSE HEATING

In HAMR, the heating process using pulsed laser is a dynamic process with considering the rotation of disk. To extend the static thermal investigations of $L1_0$ FePt to HAMR, the time dimension must be considered. The thermal design in HAMR media demands that heating and cooling of the media occur within ~ 1 ns in order to achieve the necessary data rate and to generate a large thermal gradient for sharp bit edge definition. This can be achieved by introducing a heat sink layer. In particular, Ag is used as a heat sink layer to tune the thermal properties since it not only has high thermal conductivity but also can induce the (001) texture in $L1_0$ FePt with epitaxial growth [94]. Recently, the fundamental challenges in HAMR media are to spatiotemporally tailor the lattice dynamics and the process of nanoscale thermal transport in FePt/Ag system under laser heating within the time domain of tens to hundreds of picoseconds.

Both static and dynamic aspects of thermally-dependent magnetic properties have been reported in experiments [37],[70] and simulation [24]. For the thermally-dependent lattice structure of HAMR media FePt/Ag, previous studies only

focused on static properties such as thermal conductivity [95] and epitaxial growth [94]. The time resolved lattice dynamics and nanoscale thermal transport, which are essential in the real writing process and would play a crucial role for realizing HAMR as final application, have not yet been investigated in details. In this part, the nanoscale thermal transport involving lattice dynamics was investigated using time-resolved X-ray diffraction (TR-XRD). The Ag sink layer provided a fast cooling and lowered the maximum lattice expansion and temperature of FePt. A method to fit the decay of thermally-induced lattice expansion was investigated.

3.3.1 SAMPLES DESCRIPTION AND FUNDAMENTAL CHARACTERIZATIONS

In this experiment, Ta (2 nm)/FePt (30 nm)/Ag (80 nm), Ta (2 nm)/FePt (30 nm) and Ta (2 nm)/Ag (80 nm) films were grown on (001) MgO single crystal substrates (1 cm × 1 cm × 0.5 mm) using magnetron sputtering at elevated temperatures [94]. The deposition temperature and pressure for Ag, FePt, Ta were 250 ^{o}C, 400 ^{o}C, room temperature and 1.5 mTorr, 10 mTorr, 10 mTorr, respectively. A 2 nm Ta layer was then deposited at room temperature as a capping layer to avoid oxidization.

The X-ray diffraction (XRD) θ-2θ scans in Fig. 23 show that Ag with (001) texture along the film normal was successfully deposited on the MgO substrates. The existence of superlattice peaks (001) in Ta/FePt/Ag/MgO and Ta/FePt/MgO samples suggested that the $L1_0$ ordered FePt with (001) texture was achieved on both Ag (002) and MgO (002). The X-ray rocking curves of Ag (002) and FePt (002) had the full

width at half maximum (FWHM) of 0.252^{o} and 1.434^{o}, respectively. Consistently, the in-plane and out-of-plane VSM hysteresis loops at room temperature (Fig. 23 inset) revealed high perpendicular anisotropy of the $L1_0$ FePt layer. Here the in-plane hysteresis loop was not saturated due to the extremely high anisotropy field of $L1_0$ FePt, which is typically around 70 ~ 80 kOe.

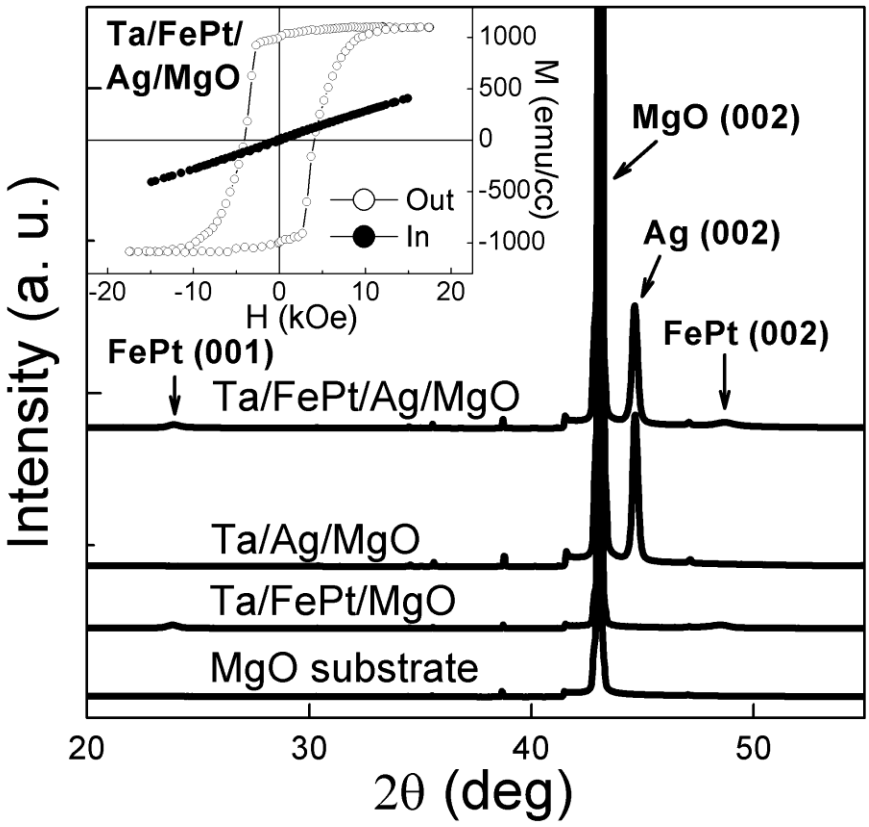

Fig. 23. θ-2θ XRD scans for Ta/FePt/Ag/MgO, Ta/Ag/MgO, Ta/FePt/MgO and MgO substrate. The inset shows the out-of-plane and in-plane hysteresis loops for Ta/FePt/Ag/MgO measured with VSM at room temperature. *M* and *H* represent magnetization in emu/cc and magnetizing field in kOe, respectively.

3.3.2 STATIONARY TIME-RESOLVED SPECULAR X-RAY DIFFRACTION MEASUREMENT WITH FIXED θ

Ultrafast X-ray diffraction, defined as using XRD to detect the lattice spacing variation with time in a resolution of fs or ps, is one of the most appropriate methods to detect non-equilibrium heat transport since it gives not only information about crystallographic structure but also the transient lattice expansion as a function of time in the film system. In particular, it shows a good capability to observe structural dynamics in real-time on atomic-scale motions [96]. Recently, a facility developed at the Advanced Photon Source (APS) demonstrated the possibility to measure TR-XRD with a picosecond time resolution [97].

In this experiment, a local area on the sample surface illuminated by the laser pulse with an elliptical spot (~ 120 μm) was probed by an X-ray beam (5 μm) with $\theta = 20^{o}$ as shown in Fig. 24a. The pulsed laser with a width of 200 femtosecond (fs) was derived from the output of Ti-sapphire laser system at a repetition rate of 272 kHz which matched the single bunch repetition rate of the APS storage ring. The laser pulse was synchronized with a particular X-ray pulse and a Pilatus area detector was gated to collect the diffraction data from this pulse. The X-ray beam from the synchrotron was focused to 5 μm diameter with a Kirkpatrick-Baez mirror system. During the measurement, the sample was spun with a spinner designed for disk testing

to avoid multishot degradation. Each set of scans were repeated 2 or 3 times to ensure data reproducibility and the averaged data were used for final discussion.

Unlike the traditional θ-2θ XRD measurement, we measured the perpendicular lattice spacing by fixing θ at 20^{o} and varying the X-ray energy (9300 ~ 10400 eV for FePt and 8800 ~ 9200 eV for Ag). The X-ray energy was selected using a Si (111) monochromator with an energy resolution of about 1.5 eV. A schematic diagram in reciprocal space for our measurement is shown in Fig. 24b. By using this configuration, the relative directions of X-ray, laser and sample were fixed. The effects from misalignment due to sample motion and an unstable X-ray signal due to a varying cross-sectional area of the X-rays on the sample surface were eliminated. In this configuration, the Bragg diffraction condition would be fulfilled when $G_h = \frac{2\pi}{d} = 4\pi\left(\frac{E}{12.4}\right)\sin\theta$, where G_h is momentum transfer in $Å^{-1}$, d is the mean distance of atomic layers, E is the incident X-ray energy in keV and θ is the angle of X-ray from the film surface.

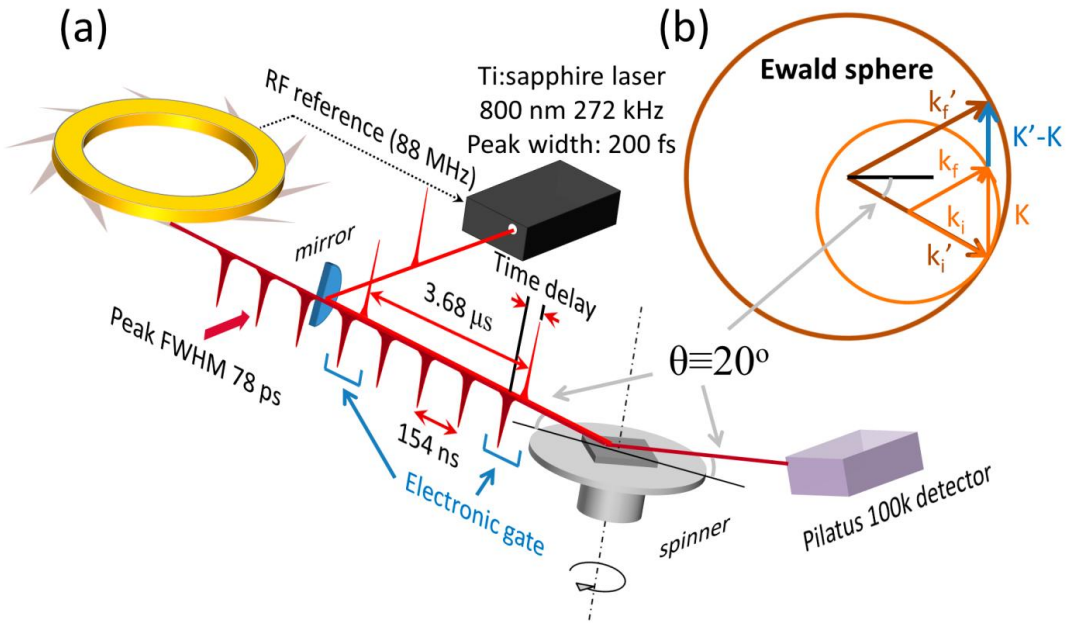

Fig. 24. The set-up of TR-XRD measurements. (a) An illustration of the set-up for TR-XRD measurement in real space. Timing changes are made by shifting phase of radio frequency reference used in laser feedback loop. (b) An schematic diagram for TR-XRD measurement in reciprocal space, here θ was fixed at 20 °and photon energy of X-ray was varied for measurement. Where $\boldsymbol{K}$ ($\boldsymbol{K'}$) is a reciprocal lattice vector, $\boldsymbol{k_i}$ ($\boldsymbol{k_i'}$) and $\boldsymbol{k_f}$ ($\boldsymbol{k_f'}$) are the wave vectors of the incident and the diffracted beams at photon energy of E (E'), respectively. They fulfill the relations $\boldsymbol{K} = \boldsymbol{k_f} - \boldsymbol{k_i}$, $\boldsymbol{K'} = \boldsymbol{k_f'} - \boldsymbol{k_i'}$ and E < E'. The diffraction occurs only when reciprocal lattice vector $\boldsymbol{G} = \boldsymbol{K'} - \boldsymbol{K}$. Here the time spacing between pulses is only for illustration, the time scales for laser and X-ray pulses are different.

3.3.3 SEPARATION OF ELECTRON AND PHONON THERMAL CONDUCTANCES

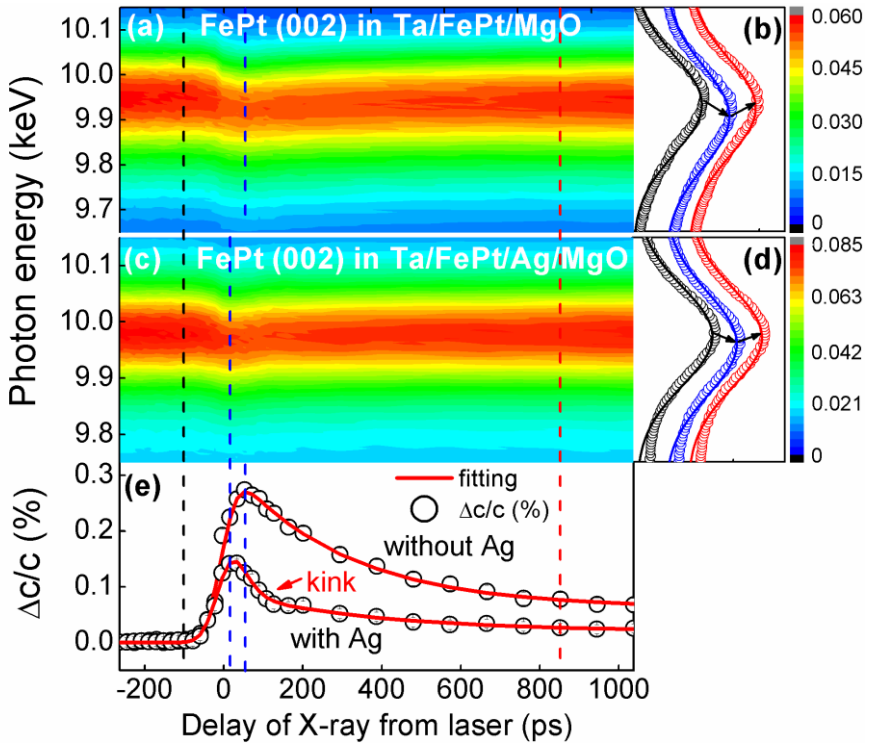

Fig. 25. Lattice dynamics as a function of X-ray delay from laser for FePt (002) in Ta/FePt/MgO and Ta/FePt/Ag/MgO. The contour plots are the FePt (002) diffractions in (a) Ta/FePt/MgO and (c) Ta/FePt/Ag/MgO as a function of X-ray delay from laser. (b),(d) XRD curves together with the Gaussian fittings at three time delays as marked in dash lines with corresponding colors. (e) The lattice expansion of FePt (002) in Ta/FePt/MgO and Ta/FePt/Ag/MgO as a function of X-ray delay from laser and its corresponding fitting lines as described in the text. Here error bars were derived from Gaussian fitting.

The contour plots of the FePt (002) diffraction peak for Ta/FePt/MgO and Ta/FePt/Ag/MgO as a function of the time delay between X-ray and laser pulses from -264 picoseconds (ps) to 1038 ps are shown in Figs. 25a and 25c. Figs. 25b and 25d show the diffraction curves at three marked time delays with corresponding colors, presenting a clear evidence for an energy position shift when the laser was applied. The diffraction peaks were fitted with Gaussian curves as shown in solid lines in Figs. 25b and 25d to obtain quantitative information about the diffraction energy position and peak integrated intensity. The lattice expansions derived from the energy shifts in Figs. 25a and 25c are shown in Fig. 25e.

When the film surface is exposed to an ultra-short laser pulse, the laser pulse initially interacts with the electrons generating hot carriers in film by transferring the photon energy to the kinetic energy of electrons. This process is typically finished within a few 100 fs. After about 0.1 ~ 1 ps, most of the energy is transferred from the hot electrons to the lattice (phonons) and equilibrium is reached between them. Several studies showed that the hot electron diffusion before transferring the energy to lattice cannot be ignored. These studies showed for an Au film the heat could be transferred with electron diffusion at a velocity close to the Fermi velocity of electrons [98] and for Al film it could reach a depth of around 70 nm before transferring energy to the lattice [99]. In our experiment the penetration depth of 800 nm laser in FePt is ~ 15 nm and hence the heat energy can be easily transferred through the entire FePt film within a few picoseconds by considering the electron

diffusion. Considering the minimum time step size (~ 18 ps) in our measurement, this may be treated as an instantaneous heating of the whole FePt film once the laser pulse is applied. The subsequent thermal decay process may be treated as the heat diffusion from the entire thermally equilibrated top layer into the underlayer/substrate.

In this section, the thermal decay process is interpreted based on a two-layer model where heat is diffused from the top layer into the underlayer/substrate through a thermal resistance by assuming a uniformly heated top layer. This model is suitable to our case since the whole FePt layer was uniformly heated in the first few ps as discussed and the subsequent thermal decay process was mainly dominated by heat diffusion. In order to quantitatively interpret the nanoscale thermal transport in the interface, a decay function from a heat diffusion equation $\frac{\partial^2 T_s}{\partial z^2} = \frac{1}{\alpha_s}\frac{\partial T_s}{\partial t}$ (here T_s is the temperature of the underlayer/substrate, α_s is the thermal diffusivity and $\alpha_s = \frac{k_s}{\rho_s c_s}$, where k_s is the thermal conductivity of the underlayer/substrate, ρ_s the mass density of the underlayer/substrate, c_s the heat capacity of the underlayer/substrate) was derived. This derivation fulfilled the conservation of heat flux condition at interface and the thermal resistance condition at interface by using the method of Laplace transformation at the limit where interface resistance is dominant [100]. It also assumed the thermal expansion coefficient is a constant ($\Delta T \propto \frac{\Delta a}{a}$):

$$(\frac{\Delta a}{a})_t = (\frac{\Delta a}{a})_{t=0} \cdot \exp[-t \cdot (\frac{\rho_f c_f d_f}{G_{th}})^{-1}] \quad (3\text{-}6)$$

Where $(\frac{\Delta a}{a})_{t=0}$ is lattice expansion at t = 0 ps, while $(\frac{\Delta a}{a})_t$ is the lattice expansion at *t* in ps, here the denominator *a* is the corresponding lattice parameter before expansion. $\tau_i = \frac{\rho_f c_f d_f}{G_{th}}$ is the exponential time-constant in ps, where ρ_f the mass density of the top layer, c_f the heat capacity of the top layer, d_f the thickness of the top layer. G_{th} is the thermal conductance of interface.

The exponential decay equation used in Plech *et al.*'s study [101] showed a good capability to calculate the interface heat transfer coefficient for Ag nanoparticles embedded in Au matrix. Generally, the decay function can be described as $f(t) = \sum_i (\frac{\Delta a_i}{a})_{t=0} \cdot \exp(-\frac{t}{\tau_i})$ for the independent decay paths ($A \rightarrow B,C...$). By further convolution of the exponential decay function with the Gaussian-like X-ray temporal profile $G(t) = \frac{1}{\sqrt{2\pi}\sigma} \exp(-\frac{t^2}{2\sigma^2})$, where $\sigma = \frac{1}{2\sqrt{2\ln 2}} \cdot FWHM$, σ = 33.1 ps for the 24-bunch operation mode of the APS, the final fitting equation may be derived for parallel decay paths by summing all paths:

$$(\frac{\Delta a}{a})_{data} = \sum_{i=1,2,3} \left\{ \frac{1}{2} \cdot (\frac{\Delta a_i}{a})_{t=0} \cdot \exp(\frac{\sigma^2}{2\tau_i^2} - \frac{t}{\tau_i}) \cdot [erf(\frac{t}{\sqrt{2}\sigma} - \frac{\sigma}{\sqrt{2}\tau_i}) + 1] \right\} \quad (3\text{-}7)$$

Where $(\frac{\Delta a}{a})_{data}$ is the lattice expansion measured in the experiment broadened by X-ray temporal profile, $(\frac{\Delta a_i}{a})_{t=0}$ is the lattice expansion after deconvolution at t = 0 ps where t is the time delay of X-ray from laser in ps. $\sigma = \frac{1}{2\sqrt{2\ln 2}} \cdot FWHM$. The thermal conductance G_{th} for the interface can be derived from $G_{th} = \frac{\rho_f c_f d_f}{\tau_i}$, where τ_i is the exponential time-constant in ps. *erf*(x) is the error function, $erf(x) = \int_0^x \exp(-t^2)dt$. The decay curves for FePt (002) in Ta/FePt/MgO and Ag (002) in Ta/Ag/MgO and Ta/FePt/Ag/MgO were also fitted with equation 3-7 for comparison.

The fitting plots are shown in Fig. 25e as red curves. A constant background, which was probably due to the long time scale heat diffusion into the MgO, was included in the fitting. Except for this, one relaxation time was needed for fitting of FePt (002) in Ta/FePt/MgO. While for FePt (002) in Ta/FePt/Ag/MgO, an obvious kink, implying a two-step relaxation, can be seen from Fig. 25e. By choosing two relaxation times, a good fit was achieved within the error bars of the experimental data points. The thermal conductance was then calculated and is shown in Table 4 using the typical values (FePt: ρ = 15 g/cc, c = 50 J mol^{-1} K^{-1}, d = 30 nm; Ag: ρ = 10.5 g/cc, c = 25.4 J mol^{-1} K^{-1}, d = 80 nm).

Table 4. Exponential time-constants as well as corresponding values of thermal conductance for the single or multiple interfaces thermal transports in different layer structures from the fittings. Standard error bars were derived during fitting with equation 3-7.

Layer structure	**Lattice plane**	**Interface**	**Exponential time-constant (ps)**	**Thermal conductance ($W\ m^{-2}\ K^{-1}$)**
Ta/FePt/Ag/MgO	FePt (002)	FePt/Ag	23.79 ± 7.0	$3.77 \pm 1.2 \times 10^{9}$
		Ag/MgO	367.19 ± 115.3	$5.38 \pm 1.9 \times 10^{8}$
Ta/FePt/MgO	FePt (002)	FePt/MgO	289.58 ± 26.9	$3.09 \pm 0.3 \times 10^{8}$
Ta/Ag/MgO	Ag (002)	Ag/MgO	244.28 ± 68.3	$8.09 \pm 2.5 \times 10^{8}$

The origin of these two relaxation times in Ta/FePt/Ag/MgO is discussed as follows. It is expected that the thermal conductance at a metal/metal interface will be high because both sides have many free electrons that can transfer their thermal energy at a velocity close to Fermi velocity [98]. This is called the electron-dominated thermal transport as shown in Fig. 26b as red line. The contribution of phonons to thermal transport in metal is typically below 10 % although there is still no agreement on a precise value [102],[103]. The situation becomes complicated when considering the thermal transport through a metal/dielectric interface such as Ag/MgO or FePt/MgO interface since phonon may play a more important role. In this case, two mechanisms are proposed to describe the thermal transport: a. electrons and phonons

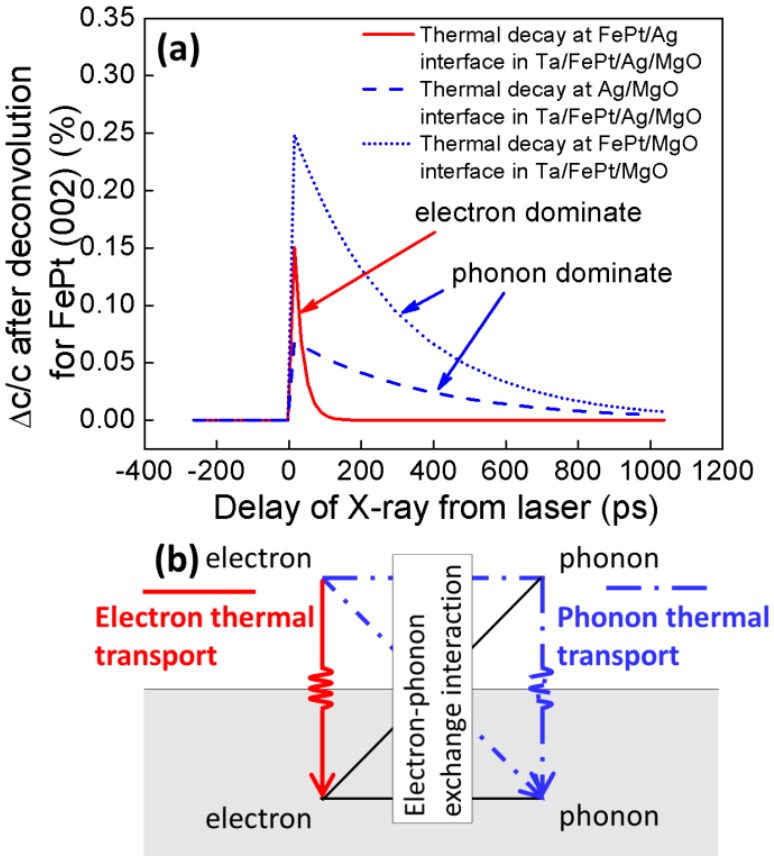

Fig. 26. Separated electron and phonon thermal transports in terms of deconvoluted exponential decays. (a) Deconvoluted exponential decay curves plotted with the parameters derived from the fitting curves in Fig. 25e. (b) A schematic diagram for electron and phonon thermal transport at interface. The electron-phonon interactions in the same layer and at the interface are treated as electron-phonon exchange interaction.

are coupled at the interface through anharmonic interactions [104],[105]; b. electrons and phonons exchange the thermal energy in the metal film first, then transfer the

energy from metal to dielectric material via phonon-phonon interaction [106]. Both processes shown in Fig. 26b as blue lines are considered as phonon-dominated thermal transport. Electron-dominated and phonon-dominated thermal transport at the FePt/Ag and Ag/MgO interfaces yielded the two relaxation processes in our measurement. For comparison, the thermal conductance for a Al/Cu interface is 3×10^{9} W m^{-2} K^{-1}, while that for Cu/Al_2O_3 is 2×10^{8} W m^{-2} K^{-1} at room temperature [107]. This is consistent with our results for FePt/Ag and Ag/MgO interfaces, respectively. The small increase in G_{th} compared with previous reported values for Al/Cu and Cu/Al_2O_3 interfaces is probably due to the relatively high temperatures reached in the measurements. The increase of thermal conductance with temperature has also been reported [108]. The deconvoluted data for two relaxation processes during thermal decay of FePt (002) for Ta/FePt/Ag/MgO together with that of FePt (002) for Ta/FePt/MgO are shown in Fig. 26a.

This thesis shows the possibility of separating the electron and phonon contributions to the thermal transport in various interfaces during a single measurement. This gives a potential opportunity to investigate the electron and phonon thermal transport separately. Nowadays, heat dissipation in modern electronic devices with high performance, high density and high reliability becomes increasingly important in device miniaturization. However a good understanding of thermal transport especially at the interface at the nanoscale is still highly desired [108]. The above method could be a potentially powerful tool for heat dissipation investigations

in modern electronic devices, where heat dissipation involves various interfaces including metal-metal, metal-semiconductor, and metal-dielectric.

3.3.4 AG HEAT SINK EFFECTS ON NANOSCALE THERMAL TRANSPORT

A melting and recrystallization of Ag at FePt/Ag interface is observed from the percentage change of the integrated intensity as shown in Fig. 27a. A similar phenomenon also was observed in Chen *et al.*'s study [108]. In their study, "the steep decrease", "Arrhenius expression-type increase" and "slow decrease" in integrated intensity of Au (111) was attributed to "melting", "grain formation" and "mosaic block crystal formation", respectively. A good match was reached between the experimental and the simulation results based on a two-temperature model and with the assumption of melting of only the surface atomic layers. The apparent time scale for this process was a little longer in our measurement due to its convolution with the X-ray temporal profile during the measurement.

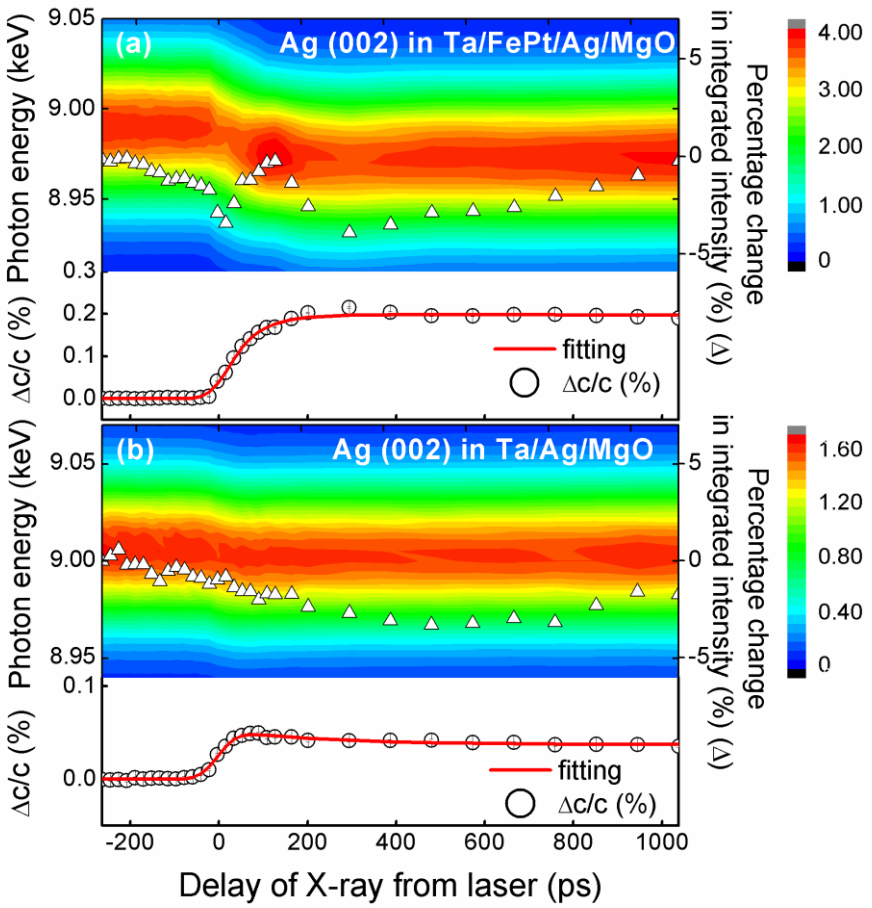

Fig. 27. Lattice dynamic as a function of X-ray delay from laser for Ag (002) in Ta/FePt/Ag/MgO and Ta/Ag/MgO. Contour plots, percentage change in integrated intensity and variations of lattice expansion with fitting lines for Ag (002) in (a) Ta/FePt/Ag/MgO and (b) Ta/Ag/MgO as a function of X-ray delay from laser. Here error bars were derived from Gaussian fitting.

The instant melting of Ag layer was mainly attributed to the higher temperature reached in Ag layer between FePt and MgO. It can be seen that the expansion of Ag lattice in Ta/FePt/Ag/MgO was much larger than that in Ta/Ag/MgO

as shown in Figs. 27a and 27b. A rough estimation of the temperature was made from the equation $T = 300K + \frac{\Delta a}{a} \cdot \frac{1}{\alpha}$ (Here α is thermal expansion coefficient for Ag). By using a typical bulk value of 18×10^{-6} K^{-1} for α, the maximum temperatures of Ag in Ta/Ag/MgO and Ta/FePt/Ag/MgO were estimated to 328 K and 419 K, respectively. This rough estimation ignores the temperature-dependent α. Note that this temperature was the average temperature over step size 18 ps rather than the actual momentary maximum temperature. The higher expansion of Ag in Ta/FePt/Ag/MgO was due to two reasons. One is that the heated Ag layer in Ta/FePt/Ag/MgO was confined between the FePt layer and the MgO substrate. It was difficult to dissipate heat since both FePt and MgO have relative low thermal conductivities (bulk values for comparison, Ag: 429 W m^{-1} K^{-1}, Fe: 80.4 W m^{-1} K^{-1}, Pt: 71.6 W m^{-1} K^{-1}, MgO: 30 W m^{-1} K^{-1}). Another is that the complex reflective index of sliver for the laser (λ = 800 nm, E = 1.55 eV) is $\hat{n} = 0.14 + 5.29i$ [109], while that of FePt is $\hat{n} = 3 + 4.5i$ (for photon λ = 633nm) [110]. A calculation using Fresnel equations [111] shows that the reflectivity at Ag and FePt surfaces with θ = 20^{o} are 97 % and 65 %, respectively. Here the minor effect from 2 nm Ta capping layer was ignored and a non-polarized laser was assumed. More photon energy was reflected from Ta/Ag interface in Ta/Ag/MgO sample.

The oscillation of expansion with time delay was observed in many studies involving metal [112] and semiconductor [113] thin films and nanoparticles [114]. The origin of this oscillation is due to phonons (strain wave) that travel through the

film reflecting from back and front surfaces and interfering within the film. However, the oscillations with time delay were not obvious in our measurement. This is mainly due to that the acoustic impedances (Z = ρc, where ρ is mass density, c is sound velocity) of FePt (~ 3.0×10^{6} g s^{-1} cm^{-2}), Ag (~ 2.7×10^{6} g s^{-1} cm^{-2}) and MgO (~ 2.3×10^{6} g s^{-1} cm^{-2}) are similar. This resulted in a small acoustic reflection at the interface between metal and substrate.

It can be seen from Fig. 26a that the maximum expansion of lattice parameter of FePt (002) was reduced by about half when 80 nm Ag heat sink layer was used. Meanwhile, the time duration of lattice expansion of FePt (002) above a certain temperature (constant expansion coefficient was assumed) was also significantly reduced. It was shown that magnetization can be reversed within 10-100 ps when heating in the vicinity or above T_C [24]. However, the overall writing process would be slower if counting also the time scale for recovery of magnetization [115]. By using the typical bulk thermal expansion coefficient (Fe: 11.8×10^{-6} K^{-1}, Pt: 8.8×10^{-6} K^{-1}, FePt (average of Fe and Pt): 10.3×10^{-6} K^{-1}), the maximum temperature of FePt in Ta/FePt/MgO would be also roughly estimated to be approximately 591 K from the equation $T = 300K + \frac{\Delta a}{a}\cdot\frac{1}{\alpha}$. When using Ag heat sink layer, the maximum temperature was around 450 K. The duration of the high temperature was significantly reduced. For example, the lattice expansion above 0.1 % for FePt without the Ag heat sink layer was 300 ps, while it was only 50 ps for FePt with the Ag heat sink layer. The use of the Ag heat sink layer increased the cooling rate, but at

the same time reduces the highest temperature attained and the duration at that high temperature, both of which are essential for reversing and the recovery of dynamic magnetization.

3.4 SUMMARY

Compositional effects on structure and temperature-dependent magnetic properties in $L1_0$ FePt epitaxial thin films were studied. XRD and VSM were used to determine the structure and magnetic properties at room temperature. θ-2θ scans showed a change of lattice parameter c due to composition change. The highest chemical ordering S, saturation magnetization M_s and anisotropy K_u were all found at the equiatomic composition. The thermal magnetic properties were measured using a SQUID with the temperature changing from 300 K to 750 K. Our results showed that excess Pt had a more profound effect on reducing T_C than the excess Fe.

Further dynamical investigation with time-resolved laser-pump X-ray-probe XRD on equatomic FePt film extended our understanding on its application in HAMR. This was also the first *in-situ* study of nanoscale thermal transport involving lattice dynamics on the magnetic recording media FePt/Ag films. Our findings showed that the cooling rate could be enhanced with the Ag heat sink layer. However, the highest temperature and the duration at high temperature were reduced at the same time. A tradeoff between these should therefore be made or an adjustable thermal control at the interface is required. This could be achieved by tailoring the electron and phonon transport properties of the interfaces. Further tailoring of electron and phonon

transport could be achieved by using thermal control layer such as MgO between recording media layer and heat sink layer. The investigation of thermal control layer is warrantied.

IV. ND DOPING EFFECTS ON FEPT

In order to modify the structural and magnetic properties of $L1_0$ FePt for its application in HAMR, Nd element was chosen to be doped into FePt. It was reported that the high magnetic anisotropy originated from the spin-orbital coupling and the hybridization of Pt 5d bands with highly polarized Fe 3d bands [116]. The addition of Nd should make a significant influence on the electronic structure of FePt. The exchange interaction in rare earth-iron based permanent materials has also been widely investigated [117]. It was shown that the exchange interaction between rare earths and iron mediated by the rare earth 5d band was essential to stabilize the magnetic order [117].

4.1 EXPERIMENTAL METHODS

The $Fe_{50}Pt_{50-x}Nd_x$ films (x = 0, 6 and 12 at. %) were hetero-epitaxial grown by co-sputtering elemental targets at ~500 ^oC on single crystal MgO (002) substrate to achieve (001) texture in $L1_0$ FePtNd films. The Ar gas pressure during deposition was 10 mTorr. After deposition, the samples were cooled to room temperature and then *a* 2 nm Ta capping layer was deposited *in-situ* before being exposed to atmosphere in order to avoid oxidization. The composition of the $Fe_{50}Pt_{50-x}Nd_x$ films was controlled by adjusting the deposition power, and further verified using energy-dispersive X-ray spectroscopy (EDX) with an accuracy of ±2 at. %. The crystallographic texture of the films was measured with x-ray diffraction, and the magnetic properties at room temperature were probed using a VSM. The X-ray magnetic circular dichroism

(XMCD) measurements were conducted at the $L_{3,2}$ edges of Fe and $M_{5,4}$ edges of Nd with an applied field of 5 T; the element specific XMCD hysteresis loops were measured at the L_3 edge and M_4 edge for Fe and Nd with an applied field varying from 5 T to -5 T. All measurements were conducted at a temperature of 10 K with the $Fe_{50}Pt_{50-x}Nd_x$ films aligned along the surface normal and at an angle of 0 ° with respect to the incident photon beam and magnetic field. The XMCD measurements were conducted at beamline 4-ID-C at the Advanced Photon Source (APS) in Argonne National Laboratory (ANL) using Total Electron Yield (TEY) detection. The X-ray Absorption Near Edge Structure (XANES) spectra of the Pt L_3 edge were measured at beamline 20-ID-B at the APS at room temperature using fluorescence mode detection.

4.2 THICKNESS DETERMINATION

The thicknesses, derived from the averaged period of XRR by considering the critical angle for total reflection θ_c as shown in the inset of Fig. 28, were 60.0 nm, 53.6 nm and 59.7 nm for $Fe_{50}Pt_{50}$, $Fe_{50}Pt_{44}Nd_6$ and $Fe_{50}Pt_{38}Nd_{12}$ films, respectively. The equation 2-2 was used for determining the thickness and a range of 12 periods were used for estimating the thicknesses in our case in order to minimize the error.

4.3 CRYSTALLOGRAPHIC STRUCTURE

X-ray diffraction (XRD) θ-2θ scans using Cu K_α radiation for $Fe_{50}Pt_{50}$, $Fe_{50}Pt_{44}Nd_6$, $Fe_{50}Pt_{38}Nd_{12}$ films, and single crystal (002) MgO substrate are shown in Fig. 28. The presence of superlattice peaks (001) and (003) in $Fe_{50}Pt_{50}$ and

$Fe_{50}Pt_{44}Nd_6$ implied the formation of $L1_0$ ordered phase with (001) direction in film normal. Ordering parameters S were 0.95 and 0.99 for $Fe_{50}Pt_{50}$ and $Fe_{50}Pt_{44}Nd_6$ from calculation, respectively. The calculation was conducted by considering the superlattice peak (001) and the fundamental peak (002) in Fig. 28 together with their corresponding full-width of half-maximum (FWHM) of the rocking curves. Both of them approached the fully ordered $L1_0$ phase. For the $Fe_{50}Pt_{38}Nd_{12}$ film, all (00k) (k = 1, 2, and 3) peaks disappeared, whereas for $L1_0$ FePt, the (200) peak existed. This indicated that higher doping concentration of Nd could deteriorate the perpendicular (001) texture. The emergence of this (200) peak could also be found in the $Fe_{50}Pt_{44}Nd_6$ film. Here, a slight shift of (00k) (k = 1, 2, and 3) peaks to larger angles was observed for $Fe_{50}Pt_{44}Nd_6$ compared with the corresponding peak positions of $Fe_{50}Pt_{50}$. This indicated the shrinking of the lattice in the perpendicular direction with 6 at. % of Nd doping. Due to the localized properties of 4f electrons as discussed later in the simulation part, 6s electrons will be drawn to the nucleus, which normally gives a smaller radius of Nd, known as the lanthanide contraction. The smaller radius of Nd compared with Pt contributed to the shrinking.

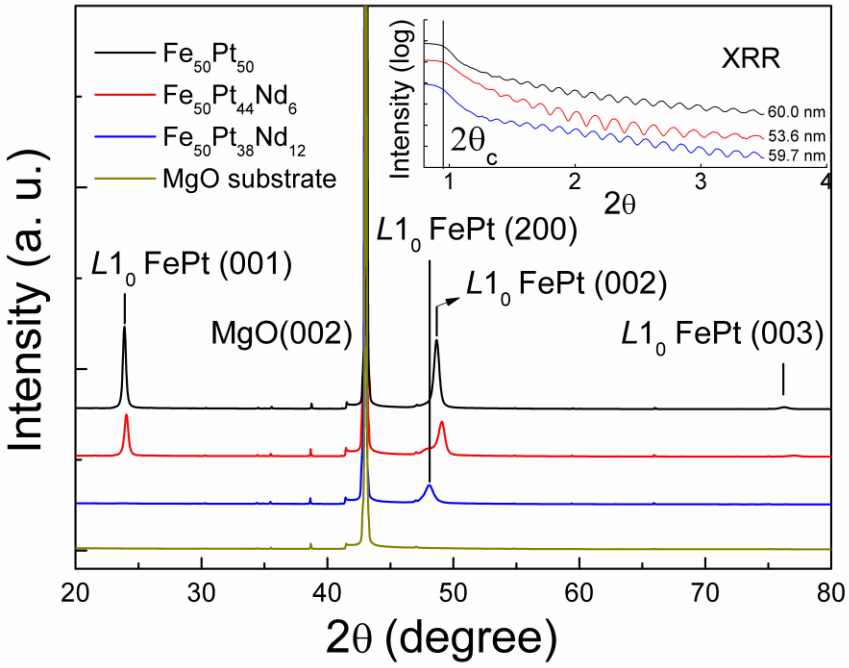

Fig. 28. θ-2θ XRD and XRR scans (inset) for $Fe_{50}Pt_{50-x}Nd_x$ (x = 0, 6 and 12 at. %) films measured at room temperature. The θ-2θ XRD scans for MgO single crystal substrate was also illustrated for comparison.

4.4 MACROSCOPIC MAGNETIC PROPERTIES

In-plane and out-of-plane hysteresis loops measured with a VSM between -2 T and 2 T at room temperature are shown in Fig. 29. Both the high magnetic anisotropies of $Fe_{50}Pt_{50}$ and $Fe_{50}Pt_{44}Nd_6$ films were consistent with the ordered and (001) textured $L1_0$ structure from XRD results in Fig. 28. For $Fe_{50}Pt_{38}Nd_{12}$ films, in-plane (002) variants, indicated as (200) peaks in Fig. 28, led to an in-plane magnetic anisotropy as shown in Fig. 29. The M_s of $Fe_{50}Pt_{50}$ was ~1128 emu/cc,

which was consistent with the previously reported value [54]. For $Fe_{50}Pt_{44}Nd_6$, the M_s was ~1335 emu/cc, indicating an 18.4 % enhancement compared to that of $Fe_{50}Pt_{50}$. The mechanism for the observed large enhancement of the total magnetic moment in $L1_0$ ordered $Fe_{50}Pt_{44}Nd_6$ films using elemental sensitive XANES and XMCD was investigated.

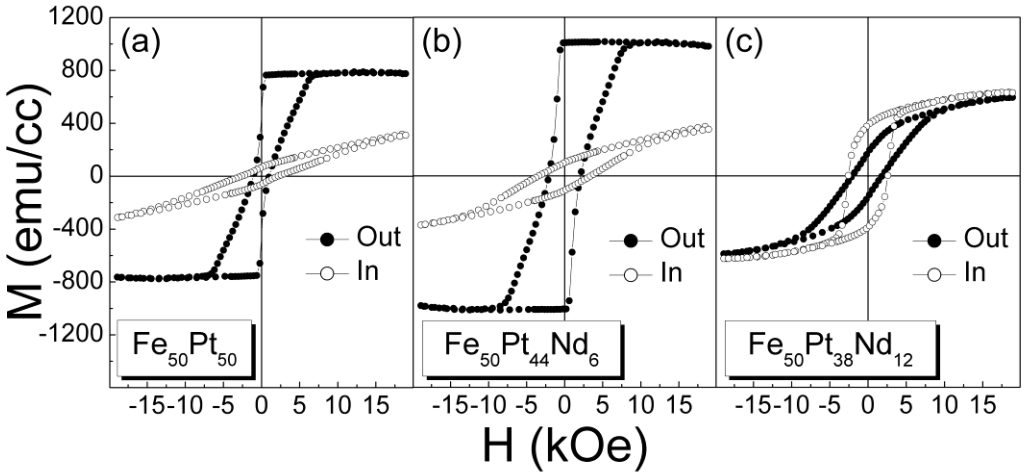

Fig. 29. In-plane and out-of-plane hysteresis loops for (a) $Fe_{50}Pt_{50}$, (b) $Fe_{50}Pt_{44}Nd_6$ and (c) $Fe_{50}Pt_{38}Nd_{12}$ measured with VSM at room temperature.

4.5 XANES INVESTIGATION

The normalized Pt L_3 edge XANES spectra μ(E) (Fig. 30c) and their derivatives (Fig. 30d) showed almost no change for $Fe_{50}Pt_{50}$ and $Fe_{50}Pt_{44}Nd_6$ films. As the XANES is sensitive to the both local structure and electronic state [118], a close

resemblance of the XANES spectra of these two films indicated that the electronic state of Pt did not change significantly with 6 at. % Nd doping. This suggestd that Fe and Nd could play the dominant roles in the observed large enhancement of total magnetic moment in $L1_0$ ordered $Fe_{50}Pt_{44}Nd_6$ films. Therefore, it would be essential to investigate the individual contribution of spin and orbital moments of Nd and Fe to the total magnetic moment, and also the exchange interaction of Fe and Nd magnetic moment. In the following part, the Fe $L_{3,2}$ edge and Nd $M_{5,4}$ edge XMCD spectra were utilized to investigate the spin and orbital moment of Fe and Nd in the films. Elemental specific hysteresis loops at the Fe L_3 edge and Nd M_4 edge were employed to investigate the exchange interaction between Nd and Fe magnetic moments.

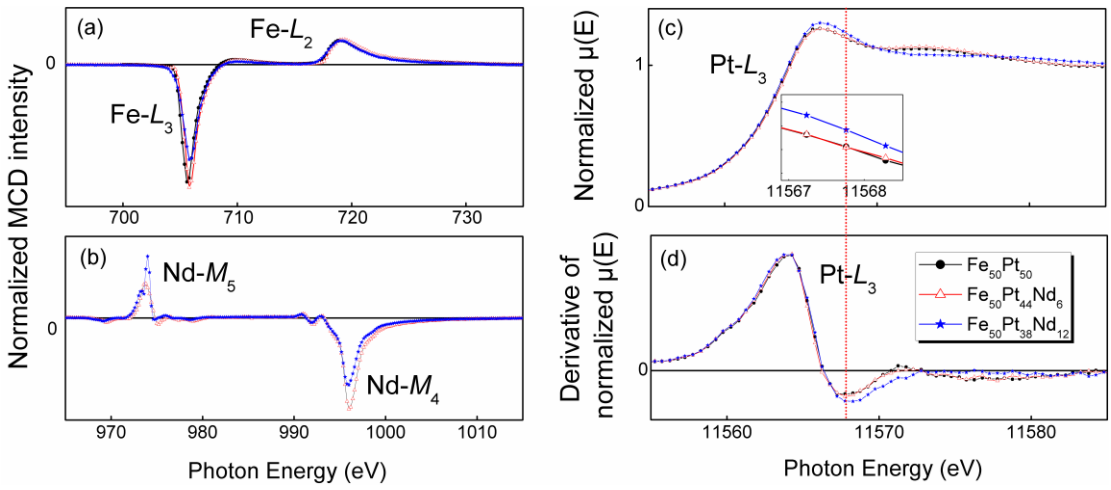

Fig. 30. XMCD spectra for (a) Fe $L_{3,2}$ (x = 0, 6 and 12 at. %) and (b) Nd $M_{5,4}$ (x = 6 and 12 at. %), (c) normalized XANES spectra and (d) their derivatives for Pt L_3 (x = 0, 6 and 12 at. %) in $Fe_{50}Pt_{50-x}Nd_x$ films.

4.6 ELEMENTAL SPECIFIC XMCD INVESTIGATION ON SPIN AND ORBITAL MOMENTS

XMCD spectra conducted at Fe $L_{3,2}$ (706.8, 719.9 eV) and Nd $M_{5,4}$ (980.4, 1003.3 eV) edges are shown in Figs. 30a and 30b for all three samples. A more significant change of MCD signal at the Nd $M_{5,4}$ edges between the Nd doping concentration of 6 and 12 at. % was observed compared with that at the Fe $L_{3,2}$ edges. In order to make a quantitative comparison, the spin and orbital moments of Fe (2d-3p transition) were quantitatively derived from sum rules, neglecting the magnetic dipole operator $<T_z>$ [85],[86]:

$$\frac{A_3 + A_2}{A} = \frac{3L_z}{10-n} P\cos\theta \tag{4-1}$$

$$\frac{A_3 - 2A_2}{A} = \frac{2S_z}{10-n} P\cos\theta \tag{4-2}$$

where A_3 and A_2 are the integrated areas of XMCD spectra at the L_3 and L_2 edges of Fe, respectively. $<L_z>$ and $<S_z>$ are the orbital angular momentum operator and spin operator in the z direction, respectively. A denotes the integrated area of the white line defined by $A = \frac{1}{2}\int(\mu^+ + \mu^-)$. P is the degree of circular polarization, and has been measured to be 0.98. θ is the photon incident angle with respect to the magnetic field direction (0). The background was approximated by a 2:1 double step-like increase of the intensity as shown in Fig. 31a to extract the spectrum contribution due to the

excitations from the $2p_{3/2}$ and $2p_{1/2}$ to the 3d states [87]. The minimum between the two edges was set as the boundary. Here, the d-electron number n was set as 6.61 from calculations [119]. The uncertainty of determining spin moment m_s and orbital moment m_l from the boundary determination and background subtraction was estimated to be ± 5 %. The resulted m_s, m_l and their ratio m_l/m_s are summarized in Table 5.

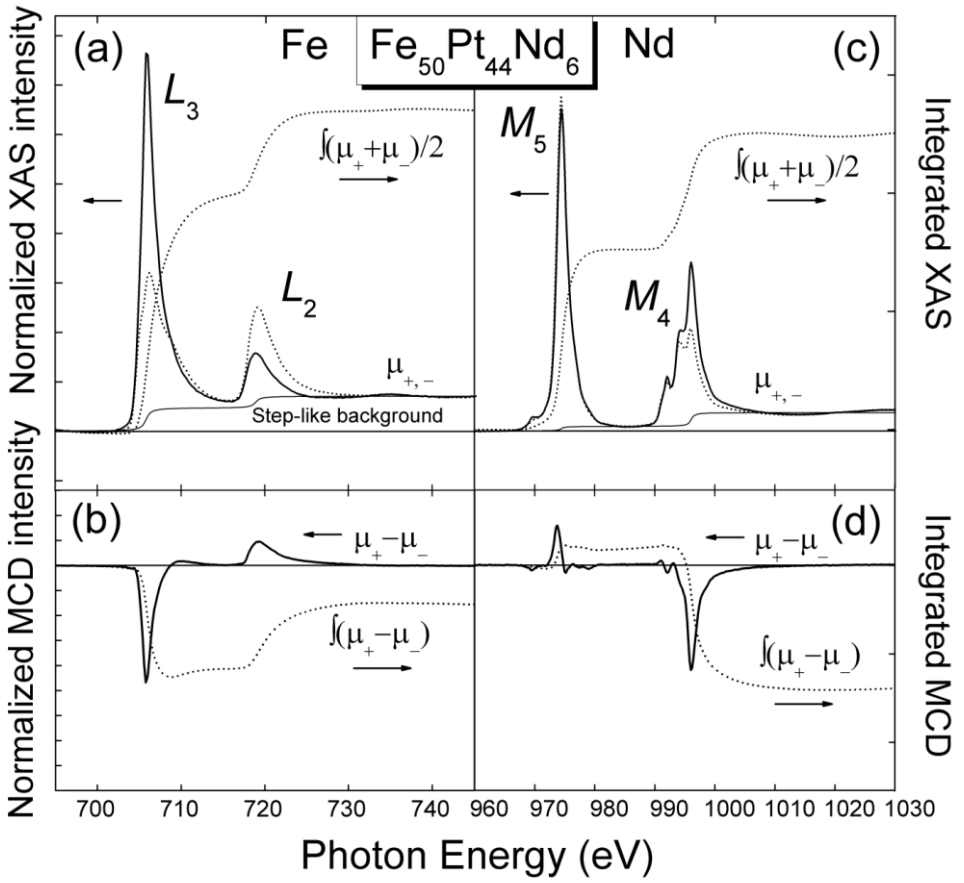

Fig. 31. Analysis of XMCD spectra with sum rules for (a-b) Fe $L_{3,2}$ and (c-d) Nd $M_{5,4}$ in $Fe_{50}Pt_{44}Nd_6$.

(a)(c) Normalized XAS using left (μ_+) and right (μ_-) circularly polarized X-rays at the Fe ($L_{3,2}$) and Nd ($M_{5,4}$) and the integration of white line ($\int(\mu_+ + \mu_-)/2$). Double step-like backgrounds are also shown as described in text. (b)(d) XMCD signals derived from the difference of normalized XAS using left and right circularly polarized X-rays ($\mu_+ - \mu_-$) and their integrations ($\int(\mu_+ - \mu_-)$).

For the rare earth element Nd, the sum rule for the 3d-4f transition can be expressed as [85],[86]:

$$\frac{A_5 + A_4}{A} = \frac{L_z}{14 - n} P\cos\theta \tag{4-3}$$

$$\frac{A_5 - \frac{3}{2}A_4}{3A} = [\frac{2S_z}{3(14-n)} + \frac{2T_z}{(14-n)}]P\cos\theta \tag{4-4}$$

where A_5 and A_4 are the integrated areas of the XMCD spectra at the M_5 and M_4 edges of Nd, respectively. The background was also approximated by a double step-like increase of the intensity, while the ratio was determined from the height of the minimum between the two edges as shown in Fig. 31c, since the statistical ratio of 3:2 does not hold due to the 3d-4f interaction [120]. However, the spin sum rules cannot be directly used for rare earth elements such as Nd. The deviation, originating from the 3d-4f exchange and 3d core spin orbital interactions, causes the intermixing of intensity between the M_5 and M_4 edges [121]. In order to take this effect into account,

a correction factor as well as the $<T_z>/<S_z>$ ratio from simulation was utilized in the calculation based on an atomic model assumption [121]. The resulting $<L_z>$, $<S_z>$ and m_l/m_s for Nd are also summarized in Table 5.

Table 5. Summary of magnetic properties derived from room temperature VSM and 10 K XMCD measurements. M_s from VSM for all three compositions. XMCD derived spin moment (m_s), orbital moment (m_l) and their ratio (m_l/m_s) were calculated from sum rules at the $L_{3,2}$ edges of Fe.The calculated $<S_z>$, $<L_z>$ and m_l/m_s at the $M_{5,4}$ edges of Nd in $Fe_{50}Pt_{44}Nd_6$ and $Fe_{50}Pt_{38}Nd_{12}$ are also tabulated. Calculation results are shown in brackets for comparison.

Composition	M_s	m_s	m_l	m_l/m_s	$<S_z>$ **or** m_s	$<L_z>$ **or** m_l	m_l/m_s
Element			Fe			Nd	
Unit	**emu/cc**	μ_B	μ_B	-	μ_B	μ_B	-
$Fe_{50}Pt_{50}$	1128	2.40	0.210	0.0875	-	-	-
		(2.925)	(0.066)	(0.0226)	-	-	-
$Fe_{50}Pt_{44}Nd_6$	1335	2.49	0.271	0.109	-0.0260	0.114	-2.192
		(2.853)	(0.072)	(0.0252)	(m_s: d(0.12) f(-1.57))	(m_l: d(0.008) f(3.82))	(d(0.067), f(2.433))
$Fe_{50}Pt_{38}Nd_{12}$	1034	2.31	0.234	0.101	-0.0217	0.0645	-1.486

The results in Table 5 show that the highest m_s and m_l of Fe were obtained with 6 at. % of Nd doping. However, the m_s and m_l of Fe decreased with 12 at. % of Nd doping. This yielded direct evidence that the doping of 6 at. % Nd in $L1_0$ FePt significantly influenced the electronic structure of Fe. An enhancement of above 25 % for m_l/m_s in $Fe_{50}Pt_{44}Nd_6$ compared with that of $Fe_{50}Pt_{50}$ also implied a significant effect on the electronic structure of Fe with Nd doping. However, the derivative of the normalized μ(E) for the Pt L_3 edge derived from XANES measurements in Fig. 30d shows that the electronic state of Pt did not change significantly with 6 at. % Nd doped. Further investigation on Nd showed that a very consistent m_l/m_s of -2.2 was obtained as compared with Nd in CoNd alloy (-2.2) [122] and atomic value of Nd from calculation (-2.4) [121].

Analyzing the x-ray magnetic circular dichroism spectra at the $L_{3,2}$ edges of Fe and $M_{5,4}$ edges of Nd in $Fe_{50}Pt_{44}Nd_6$ films, a significant contribution of Nd orbital moment was found, in addition to the slightly increased Fe spin and orbital moments as compared to that of $Fe_{50}Pt_{50}$ films. However, question remains as to why the $Fe_{50}Pt_{44}Nd_6$ films exhibited a high magnetic moment, whereas the total magnetic moment of $Fe_{50}Pt_{38}Nd_{12}$ decreased. What was the nature of the interaction of Fe and Nd moments in these two films and how would it impact the total magnetic moment?

4.7 ELEMENTAL SPECIFIC HYSTERESIS LOOPS INVESTIGATION WITH XMCD

To further investigate the relations between Fe and Nd in $Fe_{50}Pt_{44}Nd_6$ and $Fe_{50}Pt_{38}Nd_{12}$ films, the elemental specific hysteresis loops were determined by

measuring the areas of XMCD peaks at the L_3 and M_4 edges of Fe and Nd as a function of applied field. As shown in Fig. 32a, Fe and Nd reversed their moments at approximately the same applied field (4 kOe), implying a strong exchange interaction between these two elements in $Fe_{50}Pt_{44}Nd_6$. This exchange interaction could probably contribute to the higher m_s in Fe and higher $<L_z>$ in Nd. However, Fe and Nd in $Fe_{50}Pt_{38}Nd_{12}$ exhibited weak exchange interaction where Fe reversed its moment at an applied field of around 3 kOe while Nd reversed near 0 field as shown in Fig. 32b. This decrease of m_s of Fe and $<L_z>$ of Nd was consistent with a weak exchange interaction.

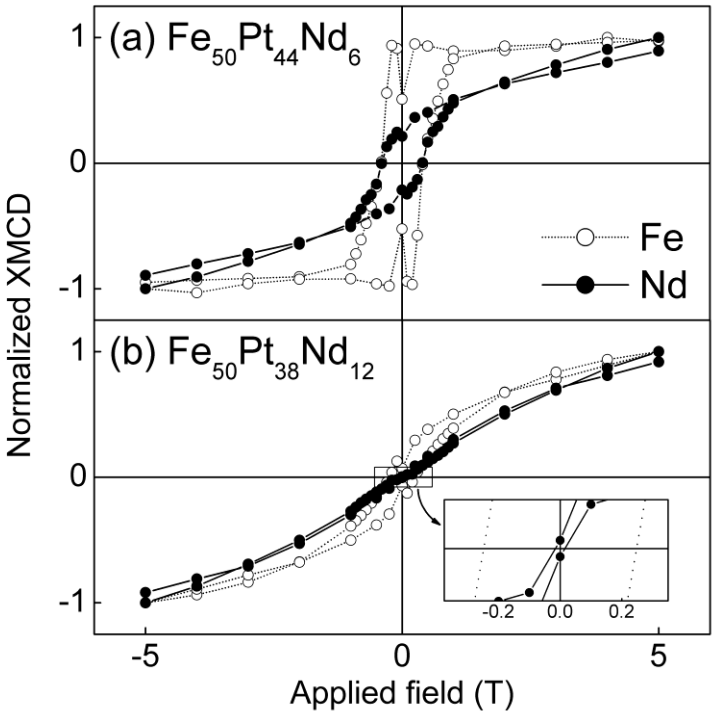

Fig. 32. XMCD magnetization hysteresis loops measure at Fe L_3 and Nd M_4 for (a) $Fe_{50}Pt_{44}Nd_6$ and (b) $Fe_{50}Pt_{38}Nd_{12}$ with XMCD. Half loop was measured in the experiment and whole loop was obtained by reversing half loop with respect to lines x = 0 and y = 0.

It has been reported that the exchange interaction between transition metal (TM) and rare earth (RE) is the main contribution to the enhanced M_s in TM-RE intermetallic and borides, such as Co-RE [123] and $Nd_2Fe_{14}B$ [124],[125]. In Co-RE system, an enhanced orbital moment of Co was observed and the corresponding magnetic anisotropy was also increased [123]. However, the origin of this enhanced orbital moment in Co-RE system is still unclear.

Antiferromagnetic coupling in spin moments and ferromagnetic coupling in orbital moments have been found for Fe and Nd in $Nd_2Fe_{14}B$ [125], which were the same as the present case. Here the orbital moments of Nd were larger than the spin moments, thus the total moments still exhibited ferromagnetic coupling as shown in Table 5. In both samples with Nd doping, $<S_z>$ was quite similar while $<L_z>$ in $Fe_{50}Pt_{44}Nd_6$ was much higher than that in $Fe_{50}Pt_{38}Nd_{12}$, suggesting that the magnetic moment in $Fe_{50}Pt_{44}Nd_6$ was much higher than that in $Fe_{50}Pt_{38}Nd_{12}$. It thus can be concluded that both Fe and Nd contributed to the enhancement of M_s in $Fe_{50}Pt_{44}Nd_6$.

4.8 FIRST PRINCIPLE CALCULATIONS

The first principle density functional calculations of the spin and orbital moments of pure FePt and Nd doped FePt systems were attempted. To simulate a 6 % doping situation a 2x2x2 supercell having 8 Fe and 8 Pt atoms with one Pt replaced by Nd was considered. The calculations were performed using Vienna ab-initio simulation package (VASP) code [126],[127] that used a plane wave basis within a projector augmented wave formalism. Perdew-Burke-Ernzerhof generalized gradient approximation was used for the exchange-correlation potential. The *f* states of Nd were treated in the valence but were shifted down in energy by Hubbard *U* interactions with Coulomb parameter *U*=7.5 eV and exchange parameter *J*=1 eV,

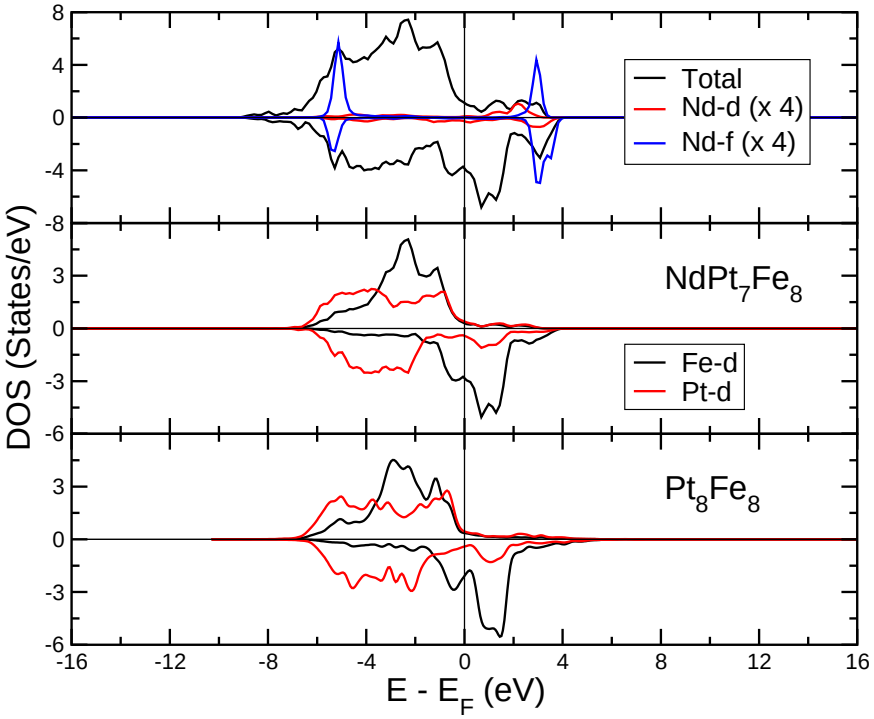

Fig. 33. Calculated spin polarized density of states for (upper) Nd-d and Nd-f orbitals along with the total DOS of the unit cell, (middle) averaged Fe and Pt DOS in the doped system and (lower) same as the middle panel but for undoped FePt. E_F indicates the Fermi level.

values obtained from literature [128]. The volume of the unit cell was fixed at the experimental one and all atoms were relaxed to obtain the optimized geometry due to Nd doping until the force on each atom reduced to 0.01 eV/Å. For pure FePt, the calculated spin and orbital moments of Fe were 2.925 and 0.066 μ_B respectively, whereas they were 0.33 and 0.051 μ_B respectively for Pt. The calculated spin and orbital moments of Fe were comparable to reported values [129]. The deviation from experimental values arose from the arbitrary choosing of n_h and uncertainty in the analysis process as discussed above. Due to Nd doping, the average spin and orbital moments of Fe became 2.853 and 0.072 μ_B, respectively; whereas for Pt, the calculated values were 0.422 and 0.073 μ_B, respectively. Considering the uncertainty ($\pm$ 5 %) from XMCD analysis, the small variation of calculated Fe moments with Nd doping was consistent with the above experimental results. The Nd doping influenced the geometry and electronic structure in such a way that there was an enhancement of orbital moments of both Fe and Pt along with an increase in Pt spin moment. The absolute values of spin and orbital moments of Nd were 1.57 and 3.82 μ_B for f-shell whereas the contributions from the d-shell are quite small (0.12 and 0.008 μ_B for spin

and orbital moments, respectively). Note that the calculated orbital moments for the f-shell should be dealt with care within a one-electron theory as crystal field effects were neglected. Nevertheless, the directions of the spin and orbital moments came out to be opposite as observed in experiments (see Table 5) with a relatively larger orbital component than the spin. Fig. 33 shows the spin-resolved density of states of pure and doped systems. In the upper and middle panels, the Density of states (DOS) of the doped system is shown. The localized f-orbitals were seen to be located around 5-6 eV below the Fermi level whereas the d-orbitals were more delocalized. Comparison of the DOS of doped and pure systems was done by observing the averaged DOS of Fe and Pt in the middle and lower panels. As mentioned before, the change in Pt DOS was insignificant whereas some features had changed in the Fe projected DOS. As expected, Pt *d*-states had a bigger bandwidth than the Fe *d*-states.

4.9 SUMMARY

In summary, the Nd doped $L1_0$ ordered $Fe_{50}Pt_{50-x}Nd_x$ thin films were studied. A large enhancement of magnetic moment was observed for Nd at x=6 at. %. Analysis of the XMCD spectra at the $L_{3,2}$ edges of Fe and $M_{5,4}$ edges of Nd in $Fe_{50}Pt_{44}Nd_6$ films indicated a significant contribution of the Nd orbital moment. The origin of the large enhancement of magnetic moment was attributed to the effect of ferromagnetic coupling of the total magnetic moments between Fe and Nd. Further first-principle calculations also supported this observation.

Room temperature crystallographic structure showed that the [002] texture began to be deteriorated at around 6 at. % of Nd doping and completely disappeared at 12 at. % Nd. In order to retain the high perpendicular magnetic anisotropy when reducing the T_C, the (002) texture must be maintained during the doping process. Further temperature-dependent investigations were focused on 3d transition metal Mn and 4d transition metal Rh doping due to their minor effects on deteriorating the texture and perpendicular magnetic anisotropy, as discussed in Chapters 5 and 6, respectively.

V. MN DOPING EFFECTS ON FEPT

It is known that the magnetic intrinsic properties depend strongly on the local atomic environment. It is thus expected doping with other elements will alter its intrinsic properties. T_C could be significantly reduced by doping with Cu [130] and Ni [37]. In Thiele *et al.*'s report, T_C was reduced to 500 K by doping with 30 at. % of Ni. However, the anisotropy K_u also decreased to 1×10^7 erg/cc [37]. For HAMR application, it is desirable to reduce the Curie temperature and retain the magnetic anisotropy as large as possible. The doping effects of Mn on the crystallographic structure and temperature-dependent magnetic properties in $L1_0$ FeMnPt (001) epitaxial films were investigated.

5.1 SAMPLE PREPARATION AND EXPERIMENTAL METHODS

FeMnPt films with Mn concentrations of 0 at. %, 5 at. %, 10 at. %, 15 at. %, 20 at. % were directly deposited onto single crystal MgO (100) substrates at 550 ^oC. Polished (100) surface of MgO substrate was sequentially cleaned by acetone, alcohol and de-ionized water. Before deposition, the base pressure was ~10^{-8} Torr. A relatively low deposition rate of 0.2~0.5 Å/s was used for deposition at Ar pressure of 15 mTorr and the thickness was fixed at 50 nm. The composition and thickness were controlled by adjusting the deposition power and time. After deposition, the films were cooled down to room temperature in the sputtering chamber under high vacuum. The compositions were then measured by EDX from SEM. The compositional results were consistent with those estimated based on the sputter rate.

Crystallographic structure was measured using XRD with Cu-K_α radiation. Long-range chemical ordering parameter S (the probability of correct site occupation in the $L1_0$ phase) was calculated. VSM and physical property measurement system (PPMS) were used to measure the in-plane and out-of-plane hysteresis loops to determine the magnetic properties such as M_s, H_c and K_u at room temperature and low temperature, respectively. SQUID was used to measure those samples at elevated temperatures using oven attachment in the temperature range up to 800 K. The value of K_u was approximated by taking the area enclosed between in-plane and out-of-plane magnetization curves in the first quadrant of M-H loops at saturation as discussed in section 3.1.3.

5.2 CHARACTERIZATIONS WITH XRD AND VSM

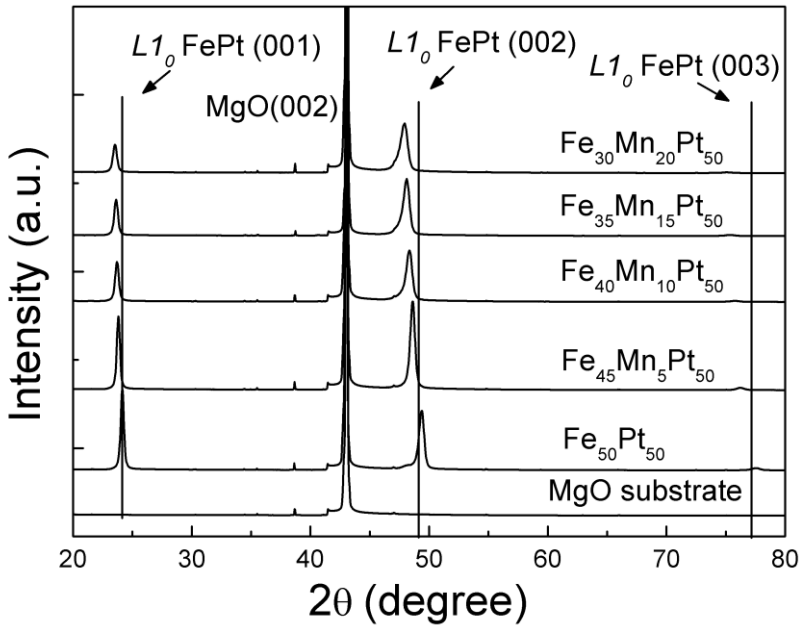

Fig. 34. XRD θ-2θ spectrum of $Fe_{50-x}Mn_xPt_{50}$ with Mn concentrations x=0, 5, 10, 15 and 20 at. %.

XRD θ-2θ spectrum for $Fe_{50-x}Mn_xPt_{50}$ films with different Mn concentrations (x=0, 5, 10, 15, 20 at. %) is shown in Fig. 34. The presence of the superlattice peaks (001), (003) was an indication that $Fe_{50-x}Mn_xPt_{50}$ grew in a same face centered tetragonal (FCT) unit cell with Mn substituting for Fe in this alloy. No other phase was found to exist. With increasing Mn concentration, (001), (002) and (003) peaks shifted to lower angles implying expansion of *c*-axis.

Table 6. The full width at half maximum (ω_{50}) of the rocking curves for the (001) and (002) peaks, the measured ordering parameter *S*, the lattice parameter *c*, saturation magnetization (M_s) at 5 K and magnetic anisotropy (K_u) at 5 K for $Fe_{50-x}Mn_xPt_{50}$

Composition	**ω_{50}(001)**	**ω_{50}(002)**	**S**	**c(Å)**	**M_s (5K) (emu/cc)**	**K_u (5K) ($\times 10^7$ erg/cc)**
$Fe_{50}Pt_{50}$	1.174 ^{o}	0.861 ^{o}	0.929	3.692	1499	6.36
$Fe_{45}Mn_5Pt_{50}$	1.064 ^{o}	0.689 ^{o}	0.805	3.747	874	4.40
$Fe_{40}Mn_{10}Pt_{50}$	1.336 ^{o}	0.981 ^{o}	0.699	3.768	804	3.11
$Fe_{35}Mn_{15}Pt_{50}$	1.263 ^{o}	0.784 ^{o}	0.690	3.787	653	1.83
$Fe_{30}Mn_{20}Pt_{50}$	1.294 ^{o}	0.857 ^{o}	0.625	3.798	626	1.46

Calculated lattice parameter *c* and ordering parameter *S* are shown in Table 6. The lattice parameter c increased from 3.692 Å to 3.798 Å as Mn concentration varied from 0 to 20 at. %. At the same time, the ordering parameter, *S*, decreased from 0.929 to 0.625. Considering that the atomic radius of Mn is almost the same as that of Fe, the decrease of ordering parameter, *S*, was mainly due to the increase of lattice parameter *c*. The order-disorder transition temperature of FePt and MnPt are 1300 ^{o}C and 950 ^{o}C, respectively. At deposition temperature, MnPt was less stable due to its

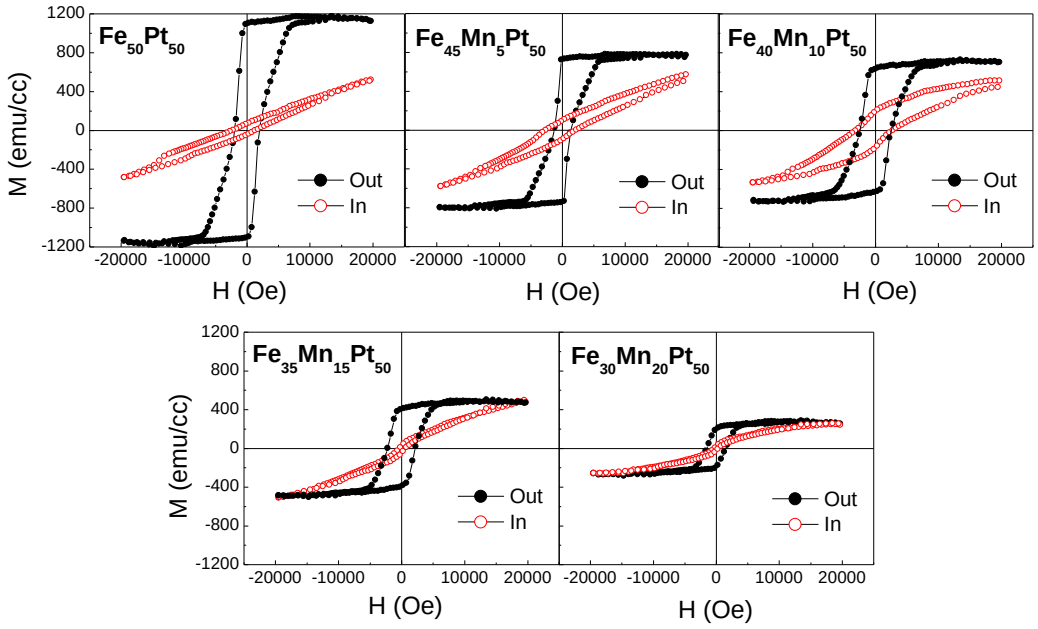

Fig. 35. Out-of-plane and in-plane M-H hysteresis loops of $Fe_{50-x}Mn_xPt_{50}$ films with Mn concentrations x = 0, 5, 10, 15, 20 at. %

lower transition energy barrier. Doping with Mn in FePt could deteriorate the chemical ordering. Since $L1_0$ phase consists of two alternate atomic layers in [001], the decrease of S could result from the mis-occupation of Pt in Fe atomic layer or Fe/Mn in Pt layer. The disruption of chemical ordering by Mn doping could affect exchange coupling and spin-orbital interaction and the resultant magnetic properties.

Figure 35 shows the out-of-plane and in-plane hysteresis loops measured with VSM at room temperature and the changes of saturation magnetization M_s and magnetic anisotropy K_u versus Mn concentration are shown in Fig. 36. The M_s for $Fe_{50}Pt_{50}$ was 1158 emu/cc, consistent with the bulk value of 1140 emu/cc reported [31]. When Mn concentration increased to 15 at. %, K_u monotonously decreased from 5×10^7 erg/cc to 1.6×10^7 erg/cc. First-principle simulation showed that the large magnetocrystalline-anisotropy energy (MAE) in $L1_0$ FePt originated from the combined effects of a tetragonal structural distortion, the exchange splitting, and the spin-orbit splitting of Pt [35]. Therefore, the observed change of K_u and S was reasonable.

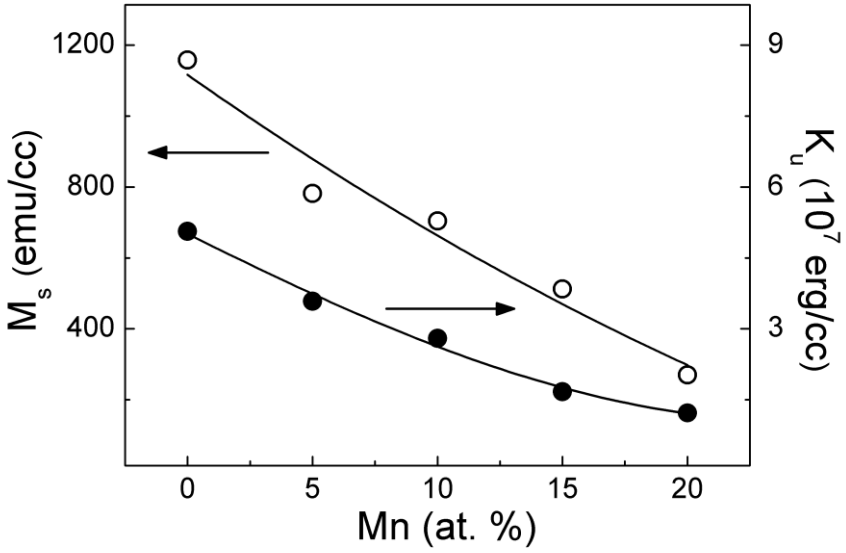

Fig. 36. The saturation magnetization (M_s) and magnetic anisotropy (K_u) as function of Mn concentration in $Fe_{50-x}Mn_xPt_{50}$ films. The solid curve is drawn to guide the eye.

5.3 MAGNETIC DOMAIN STRUCTURE

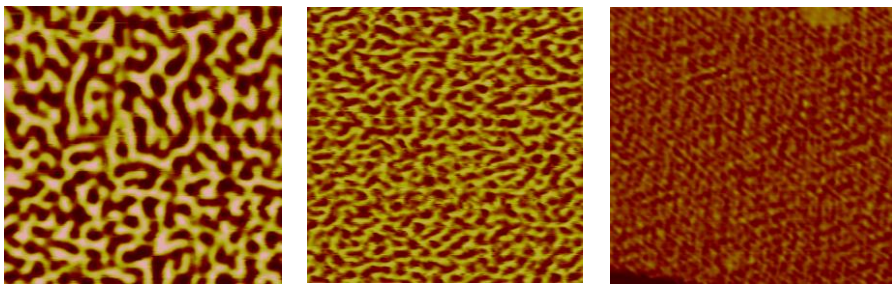

a **b** **c**

Fig. 37. MFM images of (a) $Fe_{50}Pt_{50}$, (b) $Fe_{45}Mn_5Pt_{50}$ and (c) $Fe_{30}Mn_{20}Pt_{50}$, the scan area is 5 μm ×5 μm

MFM was used to investigate the magnetic domain structure of films in the thermally demagnetized state. Before this experiment, the films were demagnetized in alternating magnetic field from VSM. The domain size is determined by the equilibrium between domain wall energy and magnetostatic energy, whereas the domain wall energy is related to the K_u of materials [54]. Fig. 37 shows the MFM images of $Fe_{50}Pt_{50}$ (a), $Fe_{45}Mn_5Pt_{50}$ (b) and $Fe_{30}Mn_{20}Pt_{50}$ (c) films. The profile was similar with that obtained by Belliard *et al*.. [131] The anisotropy could be obtained from these patterns semi quantitatively. For the simple case of film with a high perpendicular anisotropy, it resulted in purely up/down stripe domains. This can be seen in Fig. 37. With increasing Mn composition, the domain size decreased. This can be explained by using this equation [54]:

$$d \propto \frac{(\gamma l)^{1/2}}{M_s} \tag{5-1}$$

Where d is the thickness of domain, l is the thickness of the plate, M_s is the saturation magnetization and γ is the surface energy of the domain wall, which is an expression of the magnetocrystalline anisotropy. That is because the high magnetocrystalline anisotropy makes the magnetization in easy axis more stable and the domain wall should possess higher energy to rotate the magnetization from one direction to another direction. As a result, this decrease in domain size also suggested the decrease in magnetocrystalline anisotropy with Mn doping.

5.4 LOCAL STRUCTURE INVESTIGATIONS WITH XANES

5.4.1 DIRECTIONAL SHORT-RANGE ORDER (DSRO) INVESTIGATION

In this part, the investigation on DSRO was used to investigate the location of Mn in FePt. The DSRO, known as the short-range order (SRO) in a specific lattice direction, has much effect on magnetic properties [132],[133]. In this thesis, it is essential to understand the complexity of the antiferromagnetism and ferromagnetism in a system with the coexistence of AFM and FM phases such as $L1_0$ FeMnPt, known for the coexistence of the $L1_0$ FM FePt and $L1_0$ AFM MnPt phases [134].

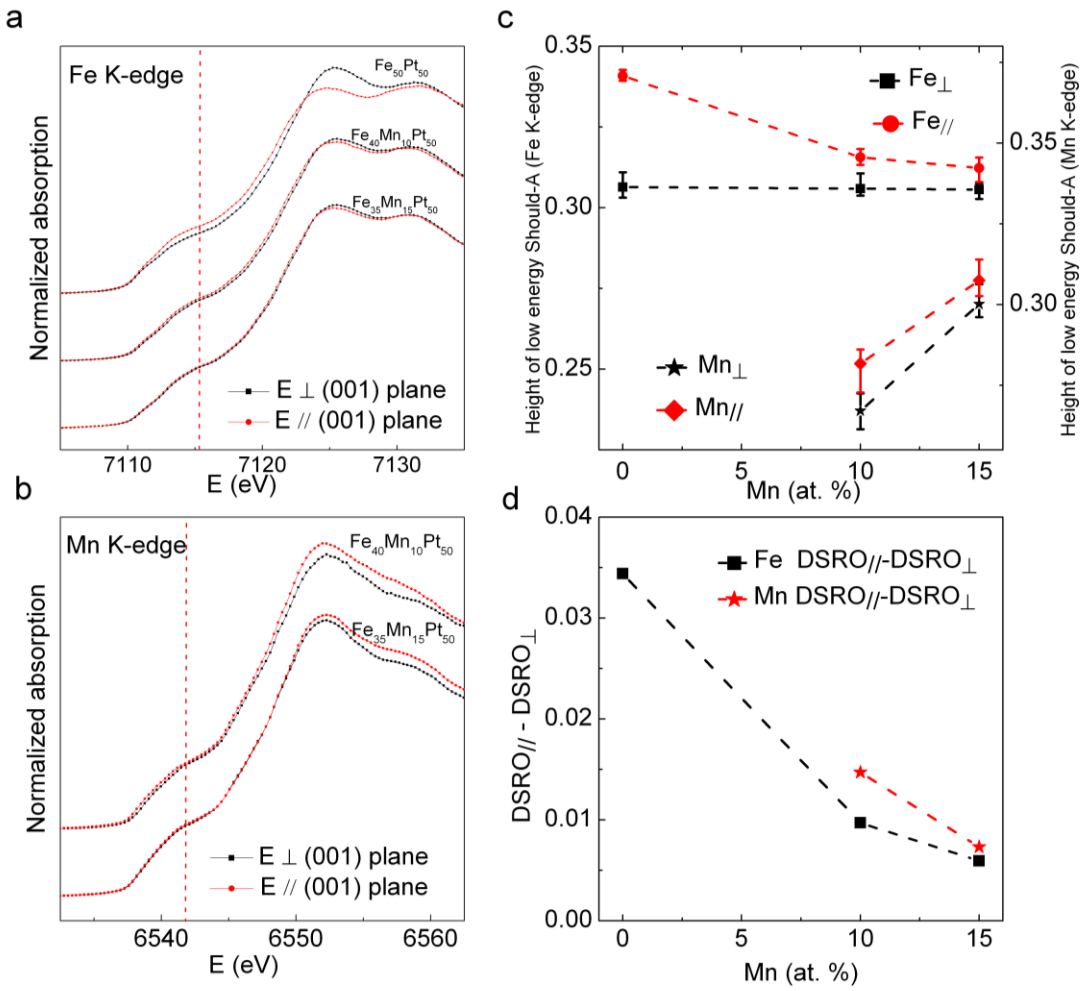

Fig. 38. Measured polarization dependent XANES spectra. a, Polarization dependent XANES spectra of FeMnPt films at the Fe *K*-edge. At least five separate measurements are used to obtain the averaged Fe XANES. b, Measured polarization dependent XANES spectra of FeMnPt films at the Mn *K*-edge. At least four separate measurements are used to obtain the averaged Mn XANES. c, The intensity of low energy shoulders as a function of the Mn composition. The error bars were obtained by comparing the averaged XANES with the individual scans. d, The difference DSRO ($DSRO_{//}$-$DSRO_{\perp}$) of Fe and Mn as a function of the Mn composition. [118]

The XANES measurements were performed using linear polarized x-rays at the undulator beamline 20-ID-B of the Advanced Photon Source (APS), Argonne National Laboratory. Details on the beamline optics and instruments can be found elsewhere [135]. In particular, the microprobe station was used to provide a focused beam size of 3 μm, allowing glancing angle measurements with x-ray polarization parallel and perpendicular to the (001) surface plane. Fe and Mn metal foils placed to intercept a scattered beam were used as an online check of the monochromator energy calibration [136]. The absorption edge positions for Fe and Mn were taken as 7110.75 eV and 6537.67 eV, respectively [137].

It has been theoretically and experimentally demonstrated that the heights of the low energy shoulder in the Fe *K*- and Mn *K*-edge polarization dependent XANES were proportional to the DSRO of Fe and Mn, respectively [118]. In principle, it can

be understood that the low energy shoulder was associated with a p-projected density of states hybridized with the 3d-states of the surrounding atoms [138],[139], the increase of the SRO of Fe-Fe or Mn-Mn would result in a decrease of the hybridization, giving rise to an increase of unoccupied states. Therefore, the height of the low energy shoulder became more pronounced.

Figure 38 displays the polarization dependent XANES measurements for the FeMnPt films at both the Fe (Fig. 38a) and Mn *K*-edges (Fig. 38b), respectively. The heights of the low energy shoulder and difference in the low energy shoulder between parallel and perpendicular XANES measurements (here parallel and perpendicular measurements represent the electric vector parallel and perpendicular to the sample surface during the measurement, respectively) are shown in Fig. 38c and Fig. 38d. While the error bars in the heights of the features for the Mn K-edge and their differences were relatively large, the results suggested that the trend of differences of DSRO in Mn as a function of Mn composition followed that of Fe, indicating that the Mn substituted into the Fe sites in the FePt films. Remarkably, subtle changes already showed up in FeMnPt films when the Mn doping increased from 10 at. % to 15 at. % for both the Mn and Fe XANES spectra. Comparing the DSRO of Mn in the $Fe_{40}Mn_{10}Pt_{50}$ and $Fe_{35}Mn_{15}Pt_{50}$ films, the difference of DSRO for Mn at $Fe_{40}Mn_{10}Pt_{50}$ films was larger than that of $Fe_{35}Mn_{15}Pt_{50}$, though the Mn doping was lower in the $Fe_{40}Mn_{10}Pt_{50}$ films as compared to that of $Fe_{35}Mn_{15}Pt_{50}$ films. These observed DSRO (Fig. 38) were consistent with a decrease of ordering parameter with

increasing Mn doping [70]. In addition, the finding that $DSRO_{\perp}$ of Fe was constant as a function of the Mn content may be understood as follows: when the Mn content increased, the $L1_0$ ordering decreased. On one hand, the decreasing of $L1_0$ ordering increased the $DSRO_{\perp}$ of Fe. On the other hand, the increasing Mn content decreased the $DSRO_{\perp}$ of Fe as a result of the decreasing of the total Fe content in the films. Consequently, the $DSRO_{\perp}$ of Fe could be constant as a function of the Mn content due to the combined effects. In a separate study of the polarization dependence of the XANES spectra of a Fe layer on the GaAs surface [140], the low energy shoulder was reduced in both parallel and perpendicular directions when the number of Fe monolayers was decreased. As reducing the number of Fe monolayers resulted in the decrease of the DSRO of Fe in both directions, the observation of decreasing of low energy shoulder with decreasing thickness of the Fe monolayer could be understood as due to a decrease of the DSRO of Fe in both directions, offering solid experimental support.

The observed magnetic properties of the FeMnPt films and the $L1_0$ ordering, obtained from LRO characterization as a function of Mn composition in this work [70], also verified the DSRO of Fe and Mn obtained by the polarization dependent XANES experiments and calculations. The theoretical calculation using first-principle theory showed that the most stable phase for $L1_0$ MnPt is an AFM phase with AFM ordering in the (001) plane, and FM order between the (001) planes [92]. $L1_0$ FePt is a FM phase with the stable status of all spins aligning perpendicular to the (001)

direction. Based on the DSRO analysis, the structural evolution as a function of Mn doping is suggested as follows: Mn substituted into the Fe site in $L1_0$ FeMnPt films and the DSRO of Mn followed the DSRO of Fe. The difference of DSRO of both Fe and Mn decreased as Mn doping increased. However the absolute amount of parallel DSRO of Mn within (001) lattice plane in $Fe_{35}Mn_{15}Pt_{50}$ was much higher than that of Mn in $Fe_{40}Mn_{10}Pt_{50}$ (Fig. 38c). The magnetic spin of Mn atom preferred to align antiferromagnetically with the magnetic spin of neighboring Mn atoms within the (001) lattice plane to minimize the total energy, thus forming the AFM phase [92]. Accordingly, the accumulation of AFM phase in the (001) plane with increasing Mn doping led to a sharp decrease of M_s [70].

5.5 DOPING EFFECTS ON TEMPERATURE-DEPENDENT MAGNETIC PROPERTIES

In HAMR, a laser is used to heat the magnetic recording media during writing process. Therefore, the thermal effects on magnetic recording media are crucial for application of HAMR since the effective writing field during heating is dominated by the gradient of thermal profile. Shown in Fig. 39a is the temperature-dependent M_s for different Mn concentrations in the range of 300 K to 750 K. Note that the films with higher Mn concentration exhibited a steeper decrease of M_s with T. The detailed mechanism for the sharp decrease of M_s was not clear. However, spin wave excitation may contribute partially to the initial decrease of M_s. Spin wave excitation caused M_s to decrease with temperature based to Bloch's $T^{3/2}$ law; and the coefficient of $T^{3/2}$ law is inversely proportional to the exchange stiffness constant A. [83] Thus sharper

decrease of M_s versus temperature at increased Mn concentration may imply that exchange stiffness constant A decreased with Mn concentration. The T_C derived from M_s-T is shown in Fig. 39b. For $Fe_{50}Pt_{50}$, T_C was 750 K, consistent with the reported value of bulk $L1_0$ FePt [32]. With Mn concentration of 15 at. %, T_C was reduced to 500 K. In Thiele's study, T_C was reduced to 500 K with Ni doping concentration of up to 30 at. % [37]. This indicated that doping with Mn was more effective in reducing T_C than Ni

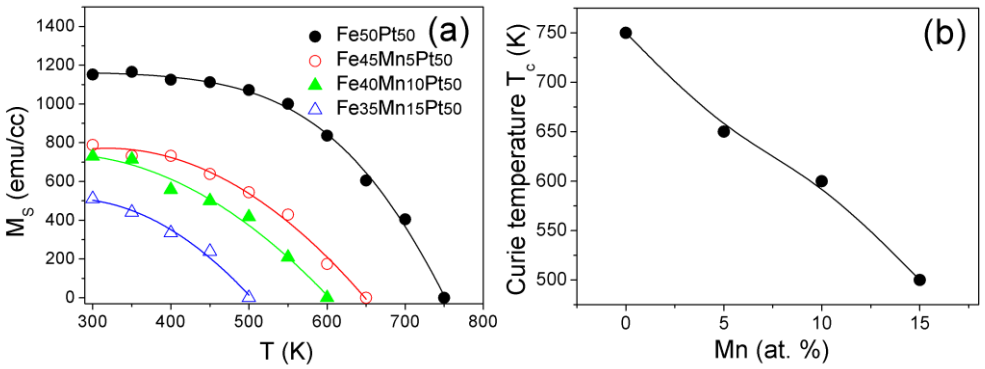

Fig. 39. (a) M_s of $Fe_{50-x}Mn_xPt_{50}$ with the temperature varying from 300 K to 750 K (b) T_C with various Mn concentrations in $Fe_{50-x}Mn_xPt_{50}$ films. The solid curve is drawn to guide the eye.

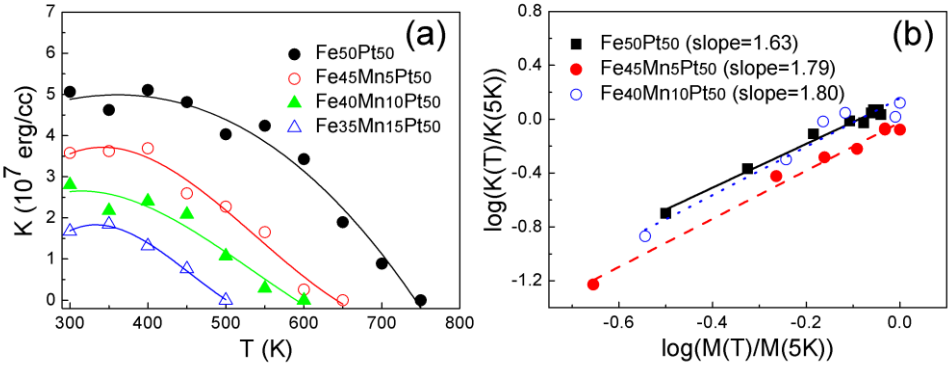

Fig. 40. (a) K_u of $Fe_{50-x}Mn_xPt_{50}$ with the temperature varying from 300 K to 750 K, the solid curve is drawn to guide the eye (b) Plots of log(K(T)/K(5K))-log(M(T)/M(5K)) and their linear fitting lines (solid line for $Fe_{50}Pt_{50}$, dash line for $Fe_{45}Mn_5Pt_{50}$, dotted line for $Fe_{40}Mn_{10}Pt_{50}$).

did. However, at Mn concentration of 15 at. %, K_u was also reduced to 1.6×10^7 erg/cc, which was similar to that of Ni doping (1×10^7 erg/cc).

Temperature-dependent K_u for different Mn concentrations in the range of 300 K to 750 K is shown in Fig. 40a. It can be seen that K_u decreased faster with temperature than M_s. From a numerical fit according to [37]:

$$K(T)/K(5K) = [M_s(T)/M_s(5K)]^n \qquad (5\text{-}2)$$

Here the values of K_u (5 K) and M_s (5 K) are listed in Table 6. It should be noted that a value of 1280 emu/cc for M_s was obtained at 5 K. This small increase in M_s at low temperature was consistent with the variation of magnetic moment of Fe atom in $L1_0$ FePt with temperature reported [141]. By fitting these points, the value of n could be

obtained. For $Fe_{50}Pt_{50}$, n = 1.63. While for $Fe_{45}Mn_5Pt_{50}$ and $Fe_{40}Mn_{10}Pt_{50}$, n were 1.79 and 1.80, respectively. Here $Fe_{35}Mn_{15}Pt_{50}$ film was not used for fitting due to likely uncertainty caused by the small temperature range. There was no significant change of n when doping with transition metal Mn. Some works also showed that an approximate exponential value of 2 was found for $L1_0$ FePt with uniaxial anisotropy [37],[38]. The value of n derived above was consistent with others' results. Thiele *et al.* also investigated this relation for $Fe_{55-x}Ni_xPt_{45}$. In their work, a value of n ~ 2 was found [37]. The physical meaning of n has been discussed previously in section 3.2 for Fe_xPt_{100-x}. For comparison, a value n = 3 was found in materials with uniaxial anisotropy system, such as the CoCrPt-based materials used in today's recording media, from simple spin disorder models [142]. In classic spin model, n was related to the symmetry of the anisotropy energy surface. It showed that the classical spin model pertinent to magnets with localized magnetic moments was not valid for $L1_0$ FePt due to its more delocalized magnetic moments. Therefore, for $L1_0$ FePt with itinerant magnetic moments, new model needs to be developed.

5.6 SUMMARY

The Mn doping effects on structure and temperature-dependent magnetic properties in $L1_0$ FeMnPt (001) epitaxial thin films were studied. θ-2θ XRD scans showed a change of lattice parameter c due to Mn doping. The thermal magnetic properties were measured using a SQUID with temperature changing from 300 K to 750 K. Our results showed that S, K_u and T_C monotonously decreased with increasing

Mn concentration. With 15 at. % Mn added, T_C could be reduced to around 500 K and the magnetic anisotropy was reduced to 1.6×10^7 erg/cc simultaneously. It indicated that doping with Mn was more effective in reducing T_C and maintaining K_u than Ni. Investigations with XANES indicated that the Mn substituted into Fe sites in the FePt films. This affected the exchange interaction between Fe and Fe and reduced the T_C.

VI. RH DOPING EFFECTS ON FEPT

$Fe_{50}Pt_{50-x}Rh_x$ films have attracted much interest recently due to their potential usage in heat assisted magnetic recording (HAMR) media and the ferromagnetic (FM) to antiferromagnetic (AFM) transition as Rh concentration is increased. Recently, Rh doped FePt has attracted much attention since it reduced T_C [143], and also formed an anti-ferromagnetic (AFM) phase when Rh was present beyond a certain concentration [143]. However, the Rh composition in $Fe_{50}Pt_{50-x}Rh_x$ for the ferromagnetic (FM) to AFM transition remains unclear. It was reported that at room temperature, a transition from FM to AFM occurred at x = 16 for $Fe_{50}Pt_{50-x}Rh_x$ [143]. In another report, the AFM at room temperature was found at $Fe_{50}Pt_{40}Rh_{10}$ [144].

Therefore, it is essential to investigate the spin and orbital moments of Fe in $Fe_{50}Pt_{50-x}Rh_x$ to understand the doping effects of Rh on the saturation magnetization M_s, the FM-AFM transition, and their correlation with MCA. In this thesis, the spin moment (m_s) and orbital moment (m_l) of Fe in $Fe_{50}Pt_{50-x}Rh_x$ films using XMCD were studied. The measurements were made in the soft X-ray region along the film normal which corresponded to the easy axis of the (001) textured $L1_0$ FePt with uni-axial magnetic anisotropy.

6.1 SAMPLE PREPARATION AND EXPERIMENTAL METHODS

A series of $Fe_{50}Pt_{50-x}Rh_x$ films (x = 0, 10, 15, 20 at. %) for XMCD and XAS study was prepared by co-sputtering elemental targets at an elevated temperature of

approximately 500 ^{o}C. The temperature was pre-calibrated with a thermocouple in contact with the sample holder. $Fe_{50}Pt_{50-x}Rh_x$ films were directly grown on (001) MgO substrates to obtain (001) texture in the out-of-plane direction. The substrates were held at the specific temperature for 20 min prior to deposition. The thickness of each film was fixed to 50 nm by adjusting the deposition time with measured deposition rate. The base pressure before deposition and the Ar gas pressure during deposition were $1\sim3.5\times10^{-8}$ Torr and 10 mTorr, respectively. A 2 nm Ta layer was then *in-situ* deposited on the surface at room temperature to avoid oxidization. The sample holder was rotated during the whole deposition process to ensure uniformity. The compositions were controlled by adjusting the deposition power and then measured with energy-dispersive X-ray spectroscopy (EDX) to be: $Fe_{50.0}Pt_{50.0}$, $Fe_{52.1}Pt_{40.0}Rh_{7.9}$, $Fe_{51.5}Pt_{34.7}Rh_{13.8}$ and $Fe_{51.8}Pt_{31.1}Rh_{17.1}$, respectively. Considering the measured compositions were within the accuracy error of EDX, the nominal composition was used for the following discussion.

The m_s and m_l of Fe in $Fe_{50}Pt_{50-x}Rh_x$ films were investigated using X-ray magnetic circular dichroism (XMCD) in the soft X-ray absorption structure (XAS) along the easy magnetization axis. XMCD is a good choice to measure magnetic properties as well as the electronic structure of element in complex system due to its element-specific and shell-selective properties. The measurements were conducted at beamline 4-ID-C at the Advanced Photon Source (APS) in Argonne National Laboratory (ANL). XMCD measurements were carried out at the L_3 and L_2 edges of

Fe at 10 K by using the total electron yield mode. Soft XAS spectra were successively measured with left and right circular polarized X-rays, the direct difference between these two spectra yielded the XMCD signal. A magnetic induction field of 5 T produced by a superconducting magnet oriented parallel to the X-ray propagation direction was *in-situ* applied perpendicular to the surface of the film as shown in the inset of Fig. 44a.

6.2 FUNDAMENTAL CHARACTERIZATIONS WITH XRD AND VSM

The macroscopic characterizations of these films were carried out with XRD and VSM at room temperature as shown in Fig. 41 and Fig. 42, respectively. The hysteresis loops measured in both in-plane and out-of-plane directions (Fig. 42) implied a large perpendicular anisotropy, which was consistent with the $L1_0$ ordered FePt (001) peaks (Fig. 41) of these films. The saturation magnetization M_s as a function of Rh concentration decreased slowly when the Rh composition was less than 15 at. %. Beyond this doping concentration, M_S showed a dramatic decrease from 663 emu/cc to 141 emu/cc when the doping concentration of Rh is 20 at. %. This sharp decrease in M_s might indicate the formation of an AFM phase. The ordering parameters S calculated from θ-2θ XRD scans and full width of half maximum (FWHM) of rocking curves (not shown here) for all samples were ~ 0.95 which was consistent with a previous report [143].

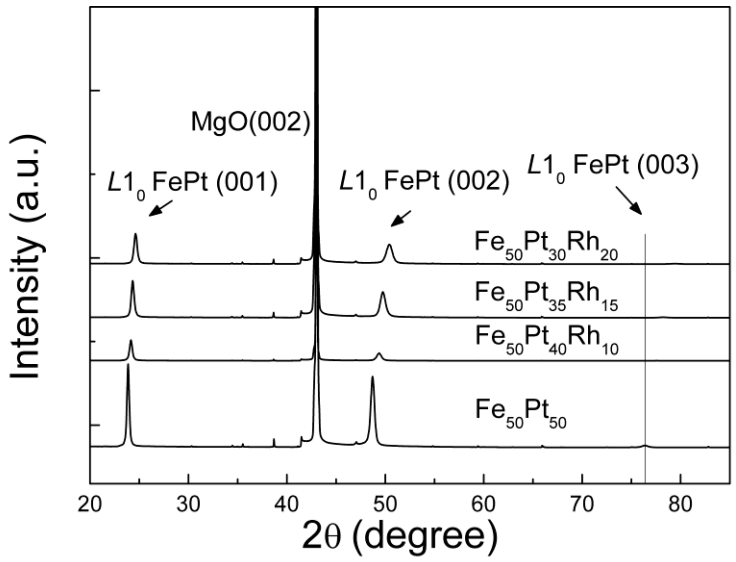

Fig. 41. θ-2θ XRD scans for $Fe_{50}Pt_{50-x}Rh_x$ (x = 0, 10, 15, 20 at. %) measured at room temperature.

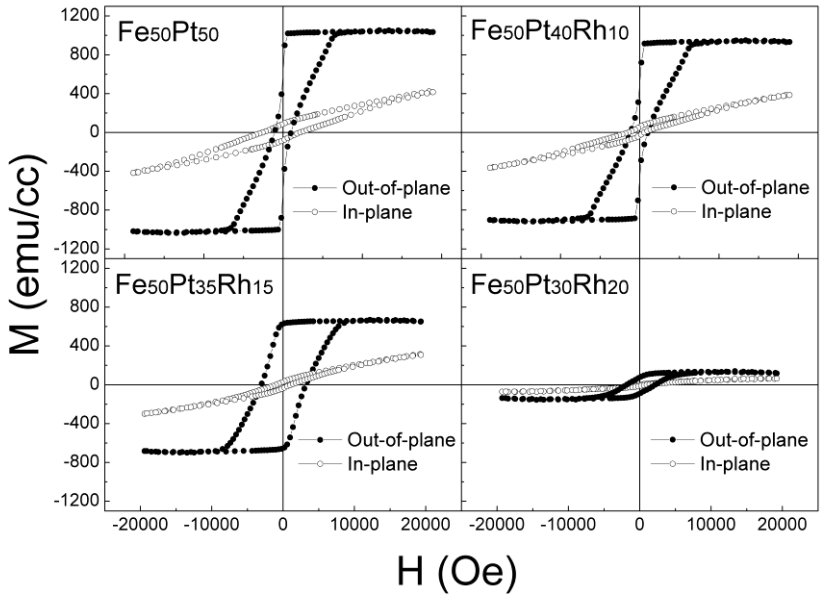

Fig. 42. In-plane and out-of-plane hysteresis loops for $Fe_{50}Pt_{50-x}Rh_x$ (x = 0, 10, 15, 20 at. %) measured with VSM at room temperature.

The crystallographic structure upon different doping concentration of Rh at room temperature was examined. In Fig. 43, the lattice constants of *c*, *a*, *c*/*a* ratio and *S* with Rh doping concentration are shown. It can be seen that *c* monotonously decrease with Rh doping. However, *a* faced an increase first and then decrease, the maximum can be found at 5. % Rh. This attributes to the deterioration of *S* at 5. % Rh where the *S* had the minimum value. It implied that the doping of Rh with low concentration could deteriorate the *S*. With further increasing the doping concentration, *S* increased again and restored the initial value and approached the fully ordered value. It indicated that the Rh doping had higher ability to maintain the ordering of $L1_0$ phase than Ni [37] and Mn [70],[118] did. It makes the substitution effects in a single phase system realizable. It also can be seen that both *S* and *c*/*a* had little change with Rh doping, which was consistent with the previous report [145].

Further investigations on magnetic properties showed that M_s and K_u underwent a dramatic change with Rh doping as shown in Figs. 45a and 45c. This implied a substantial change of electronic structure and magnetic moments as discussed in the previous report [146]. In essence, these variations should originate from the change of local atomic environment in $L1_0$ FePt, which will be discussed below.

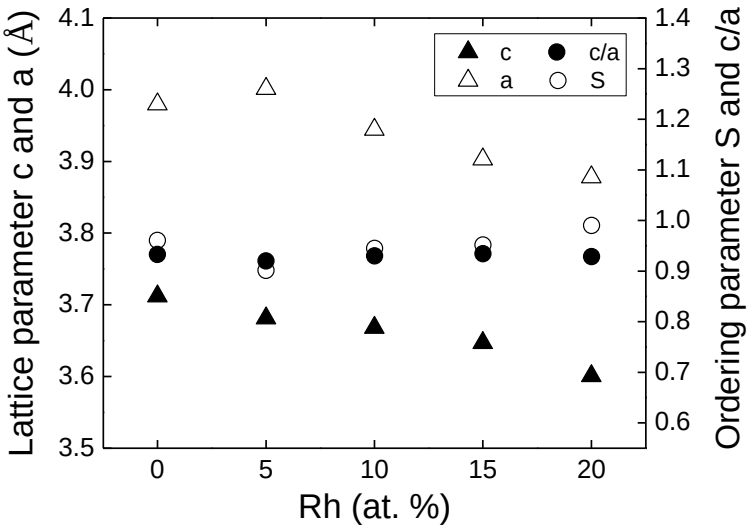

Fig. 43. The variation of *c*, *a*, *c*/*a* ratio and ordering parameter *S* with Rh doping concentration

6.3 SPIN AND ORBITAL MOMENTS INVESTIGATIONS

The normalized XAS spectra probed by left and right circular polarized X-rays are shown in Fig. 44a. The absorption intensities at the L_3 and L_2 edges of Fe were related to the transitions from the $2p_{3/2}$ and $2p_{l/2}$ into the empty 3d-like bands. Here the absence of a significant peak at a slightly higher energy than the L_3 and L_2 edges of pure Fe suggested that the film was not oxidized. The direct difference between the two normalized XAS spectra gave the XMCD spectra for different Rh doping concentrations as shown in Fig. 44d. The intensities of MCD peaks at the L_3 and L_2 edges decreased with the Rh concentration. It has been reported that the asymmetry

(dichroism divided by total absorption) ΔXMCD at Fe L_3 edge yielded direct information about the magnetic moment [147]. The ΔXMCD versus Rh concentration plotted in Fig. 44e shows a similar trend with M_s, suggesting that the change of magnetic moment of Fe played a dominant role in the macroscopic magnetization. When the doping concentration of Rh increased from 0 to 20 at. %, M_S had a reduction of 83 % while ΔXMCD had a reduction of 73 %. This may imply a minor contribution from Pt and Rh.

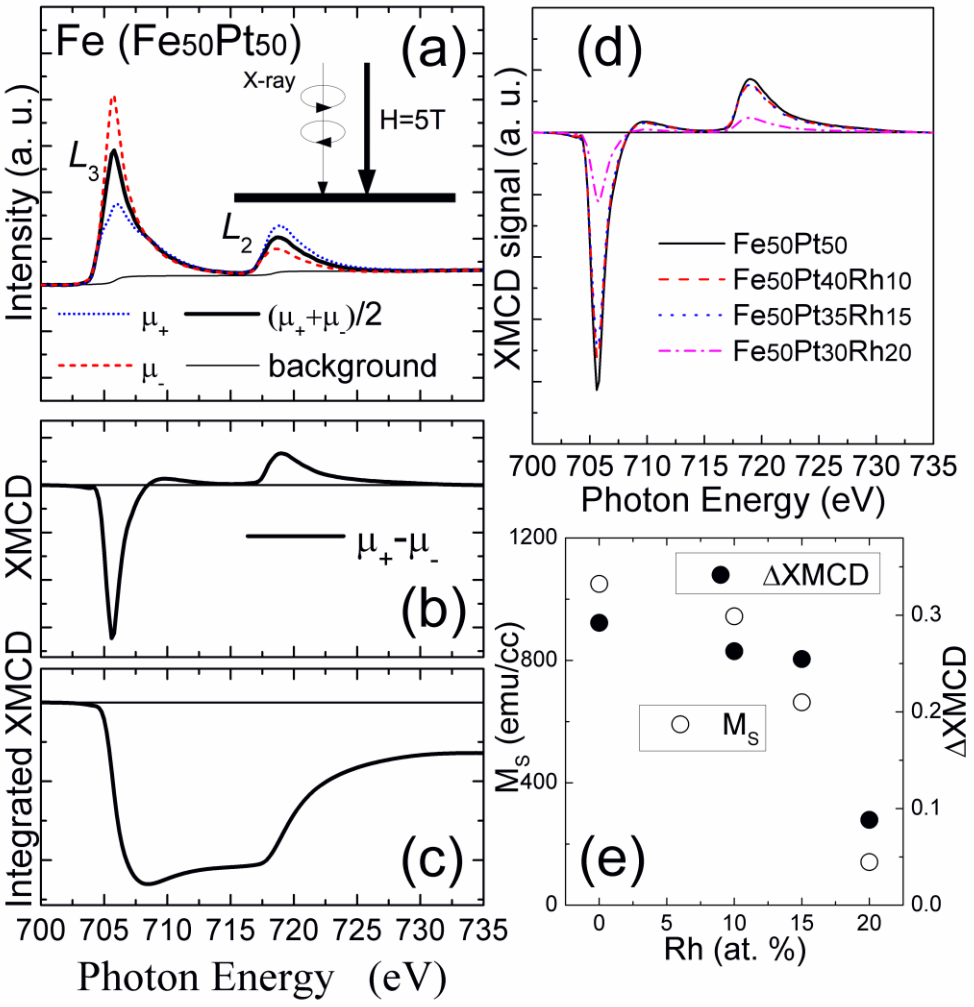

Fig. 44. (a), (b) and (c) show the analysis of XMCD spectra with sum rules for Fe $L_{3,2}$ in $Fe_{50}Pt_{50}$ film: (a) Normalized XAS using right and left circularly polarized X-rays at the L_3 and L_2 edges of Fe. An external field of 5 T parallel to the incident photon direction was applied perpendicular to the surface. White line and double step-like background are also shown; (b) XMCD signal derived from the difference of normalized XAS using right and left circularly polarized X-rays; (c) Integrated XMCD from (b). (d) XMCD spectra for Fe $L_{3,2}$ in $Fe_{50}Pt_{50-x}Rh_x$ (x = 0, 10, 15, 20 at. %). (e) The change of saturation magnetization M_S and XMCD asymmetry at the Fe L_3 edge as a function of Rh doping concentration.

The spin moment and orbital moments of Fe from $L_{3,2}$ edges (2p-3d transition) were quantitatively derived from sum rules [85],[86] with neglecting the magnetic dipole operator as proposed [148].

$$m_s = -\frac{N_h}{P\cos\theta}\frac{A_{3/2} - 2A_{1/2}}{A_d}\mu_B \tag{6-1}$$

$$m_l = -\frac{2N_h}{3P\cos\theta}\frac{A_{3/2} + A_{1/2}}{A_d}\mu_B \tag{6-2}$$

Where $A_{3/2}$ and $A_{1/2}$ are the integrated areas of XMCD spectra at the L_3 and L_2 edges, respectively. A_d denoted the integrated XAS spectra into d states, P is the polarization fraction and estimated as 0.98, θ is the photon incident angle with respect to the magnetic field direction. The background was approximated by a 2:1 double steplike

increase of the intensity as shown in Fig. 44a to extract the spectrum contribution due to the excitations from the $2p_{3/2}$ and $2p_{1/2}$ to the 3d states [87]. The white line, obtained by averaging the initial normalized XMCD spectra to obtain the nonmagnetic contribution, is also shown in Fig. 44a. The minimum between two edges was set as the boundary. Here, the d-hole number N_h was set as 3.39 from calculations [119]. The uncertainty of determining m_s and m_l was estimated to be ~10 % which resulted from the boundary determination and background subtraction.

Table 7. Measured m_s and m_l from XMCD spectra derived from sum rules analysis for $Fe_{50}Pt_{50-x}Rh_x$ (x = 0, 10, 15, 20 at. %)

Composition	**$m_s(\mu_B)$**	**$m_l(\mu_B)$**	**m_l/m_s**
$Fe_{50}Pt_{50}$	2.40	0.21	0.0875
$Fe_{50}Pt_{40}Rh_{10}$	2.15	0.19	0.0884
$Fe_{50}Pt_{35}Rh_{15}$	2.10	0.17	0.0810
$Fe_{50}Pt_{30}Rh_{20}$	0.67	0.08	0.1194

The m_s and m_l of Fe determined from the sum rules analysis are shown in Table 7. The m_l for Fe in $Fe_{50}Pt_{50}$ was 0.21 μ_B, while theoretical calculations gave a value of m_l = 0.06~0.08 μ_B for Fe in $L1_0$ FePt [149]-[151]. This enhancement of m_l has also been observed in other experiments for FePt [152],[153]. One reason for this enhancement is due to the decreased symmetry in thin film [154]. The underestimation of m_l has

also been found in other systems [35],[155]. It was reported that m_l was enhanced with MCA and tetragonal distorted lattice [153],[156]. The decrease of m_l with Rh concentration also implied the decrease of MCA, which could be qualitatively observed from out-of-plane and in-plane hysteresis loops in Fig. 42.

The spin moment m_s derived for $Fe_{50}Pt_{50}$ was very close to the value from another study when considering the uncertainty [152]. When the Rh concentration increased, m_s showed a significant decrease beyond 15 at. % of Rh. This was consistent with the formation of an AFM phase at the_concentration of Rh above 15 at. % since only uncompensated spins were detected in MCD. Studies of temperature dependent m_s and m_l of FeRh showed that a nearly vanished value of m_s and m_l was observed below the AFM to FM transition temperature [157]. It was reported that at room temperature, a transition from FM to AFM occurred in $Fe_{50}Pt_{34}Rh_{16}$ [143]. However, in D. Lott *et al.'s* report, the AFM at room temperature was demonstrated in $Fe_{50}Pt_{40}Rh_{10}$ using neutron diffraction [144]. In our experiment at 10 K, a significant decrease of m_s was found for concentration between x = 15 and 20 at. %. The deviations could be due to the different sample preparation methods and thicknesses.

The m_l/m_s ratio for Fe in $L1_0$ $Fe_{50}Pt_{50}$ was 0.0875 as shown in Table 7, which was around twice the m_l/m_s ratio obtained for pure Fe [119]. When the Rh concentration increased up to 20 at. %, the m_l/m_s ratio of Fe increased by 36 %. This implied that the doping of Rh in FePt significantly influenced the spin-orbital interaction. This may affect the MCA as well as temperature dependent magnetic properties. A further

investigation of Rh doping effects on temperature dependent magnetic properties as well as T_C was warranted.

6.4 TEMPERATURE-DEPENDENT MAGNETIC PROPERTIES

In HAMR application, high temperature is involved to reduce the switching field of magnetic media material. The thermal gradient dominating the effective writing field is crucial for achieving the narrow transition width. In order to examine the high temperature magnetic properties of FePt with Rh doping, temperature-dependent magnetic measurement was done for this series of samples using SQUID with attached high temperature oven. The data of $Fe_{50}Pt_{50}$ was from a previous study for comparison [70]. It shows with increasing temperature, K_u underwent a steeper decrease than M_s. The initial decrease of M_S might be due to the excitation of spin wave based on Bloch $T^{3/2}$ law. A steeper slope at the initial decrease of M_s gave an indication that the exchange integral may experience a decrease with Rh doping since the coefficient of $T^{3/2}$ law is inversely proportional to the exchange stiffness constant A and exchange integral J [83]. This was further confirmed by examining the variation of T_C. With 15 at. % of Rh doping, T_C was reduced to 500 K. This was very similar to the Mn doping as reported [70]. However, Rh doping allowed higher doping concentration in $L1_0$ FePt since it did not affect S. With 20 at. % of Rh, T_C was reduced to 400 K. However, K_u was also highly reduced in this composition. To make a compromise, 15 at. % of Rh reduced the T_C to 500 K, K_u underwent a 50 % decrease from 4 to 2×10^7 erg/cc at the same time. Log plots as shown in Fig. 45d show that a

value of 2 was derived for *n*. There was no significant change of *n* when doping with Rh. It suggested that there was almost no change of itinerant properties of electron. Some works also showed that an approximate exponential value of 2 was found for $L1_0$ FePt with uniaxial anisotropy [37],[38].

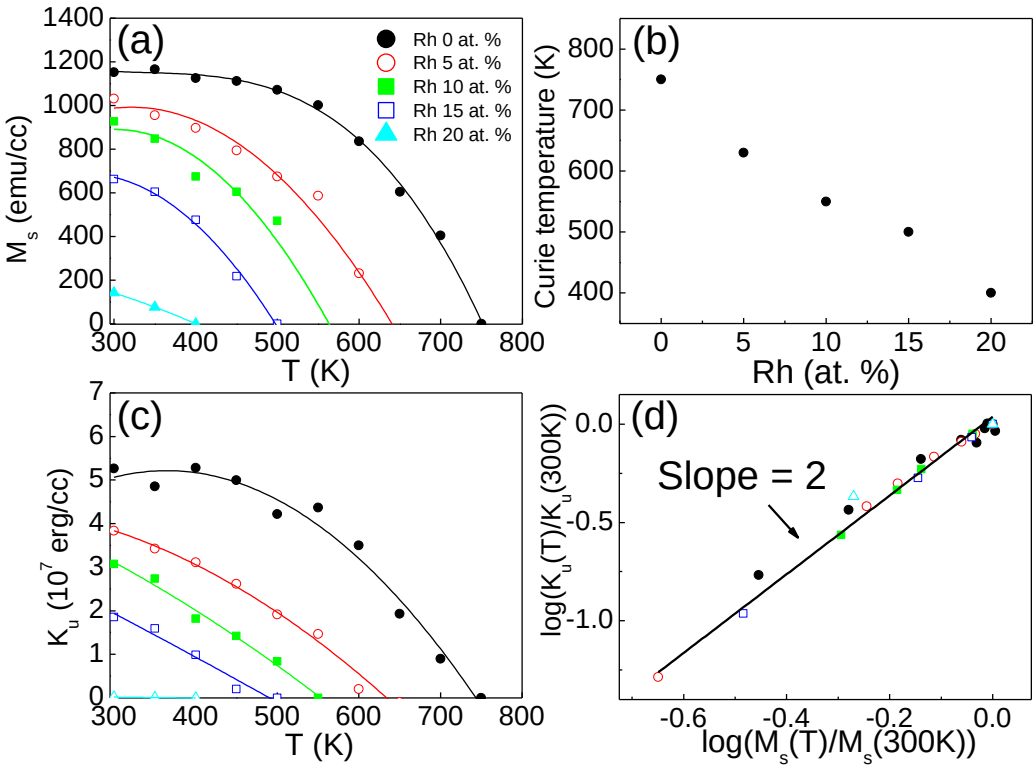

Fig. 45. (a) M_S and (c) K_u varied with the temperature for $Fe_{50}Pt_{50-x}Rh_x$ films, (b) T_C varied with various Rh concentrations. (d) Plots of log[$K(T)/K$(RT)] vs. log[$M(T)/M$(RT)]. The solid curve is fitted to guide the eye.

6.5 LOCAL ATOMIC ENVIRONMENTAL INVESTIGATIONS

The variation of electronic structure and magnetic properties of $L1_0$ FePt with doping element should originate from the change of the local atomic environment. It has been reported that Rh doped FePt had strong effects on its exchange interaction [144] and magnetic moments [146]. In this thesis, the variation of local atomic environment of FePtRh films and its influence on the temperature-dependent magnetic properties were addressed. Furthermore, the proportional relation between normalized T_C and Rh doping concentration with a slope of 1.10 was derived to evaluate the effectiveness of reducing T_C with doping element.

6.5.1 EXAFS DATA ANALYSIS

The analysis of Extended X-ray absorption fine structure (EXAFS) is very helpful in determining the local atomic environment of the atoms concerned due to its elemental-specific feature. The measurements at Fe-*K*, Pt-*L* and Rh-*K* edges were conducted at 20-BM at the Advance photon source (APS) in Argonne national laboratory (ANL), US. X-ray from synchrotron radiation was monochromatized by single crystal Si (111) monochromator and its energy was continuously tuned with tilting the angle of the monochromator. Fluorescence detection model was used for collecting data. During the measurement, the corresponding elemental metal foil (Fe, Pt or Rh) was placed besides the incident beam as a reference to calibrate the X-ray energy. The perpendicular and parallel measurement corresponded to the electrical vector of the X-ray parallel and perpendicular to the film surface normal *n*, respectively. In order to ensure the uniformity and reproductivity, the sample was

spanned around the film normal during the measurements and 4-5 scans were conducted for each measurement. $\chi(k)$ was then extracted from the raw data with Athena and analyzed with Artemis.

During the fitting process, the standard formula (equation 2-3) was used to model the EXAFS spectra [77],[78]. S_0^2 (0.843 here for Fe *K*-edge), the global factor which can be determined form the fitting of elemental foil, should be fixed during the whole analysis process. By constructing a proper model for the fitting, the local atomic environment of absorbing atom can be determined and the parameters used for constructing model can also be optimized from the fitting.

The fitting was carried out by minimizing the *k* weighted *R*-factor which can also evaluate the quality of fitting:

$$R^2 = \frac{\sum_j (k^n(\chi_j^{th}(k) - \chi_j^{\exp}(k)))^2}{\sum_j (k^n \chi_j^{\exp}(k))^2} \tag{6-3}$$

n here is the order of weighting. The statistical significance of fitting was then evaluated by the reduced χ_v^2 function:

$$\chi_v^2 = \frac{1}{N_p - N_{par}} \frac{\sum_j (k^n(\chi_j^{th}(k) - \chi_j^{\exp}(k)))^2}{\sum_j (k^{2n}\sigma_o^2)} \tag{6-4}$$

N_p and N_{par} are independent points and number of variables, respectively. σ_o^2 is the statistical deviation of the experimental points [158].

6.5.2 LOCAL ATOMIC ENVIRONMENT INVESTIGATIONS

In order to examine the variation of local environment with Rh doping, the EXAFS at Fe *K* edge for FePt in both perpendicular ($E \| n$) and parallel ($E \perp n$) measurements were investigated. Here, fully ordered $L1_0$ phase as revealed from the XRD results was used for modeling. By choosing the appropriate fitting parameters as shown in Table 8, a good fitting was achieved as shown in Fig. 46. The values of *R*-factor implying the goodness of fit were 0.0186 and 0.00487 for perpendicular and parallel measurements, respectively. Normally, a value of *R*-factor smaller than 0.02 implies a good fit. This implied a fully ordered $L1_0$ FePt was achieved which was consistent with the results from XRD.

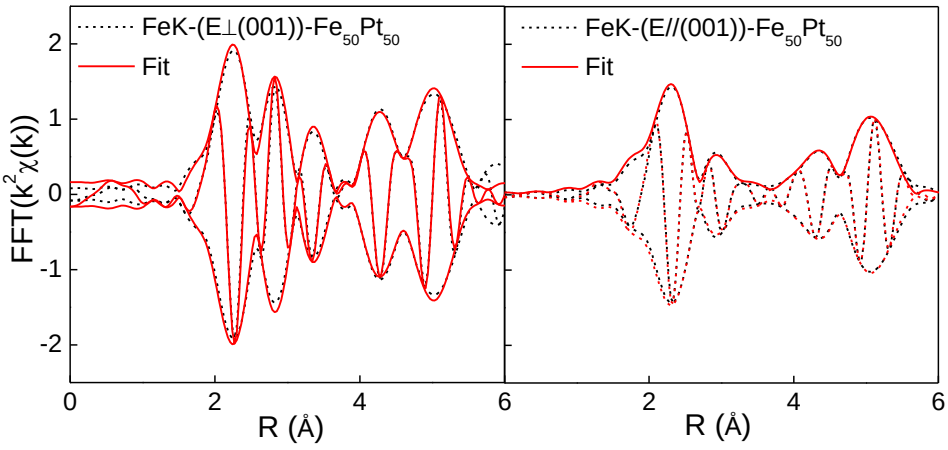

Fig. 46. χ(R) and theoretical χ_{theo}(R) based on ideal $L1_0$ model for Fe *K* edge in perpendicular (left) and parallel (right) measurement configurations for $Fe_{50}Pt_{50}$

Table 8. A summary of the parameters used for constructing the model to have the best fitting with the χ(R) in perpendicular and parallel measurements for Fe *K* edge in $Fe_{50}Pt_{50}$.

Parameter	alpha	ΔE-Fe	ΔE-Pt	σ^2-Fe	σ^2-Pt	R-factor	Reduced χ_v^2
$Fe_{50}Pt_{50}$ – Fe K (⊥)	-0.00173 +/-0.00194	5.71+/- 1.38	6.52+/- 0.552	0.0120+/ -0.00296	0.00603+/- 0.000582	0.0186	145.56
$Fe_{50}Pt_{50}$ – Fe K (∥)	0.00636+/- 0.00340	10.4+/- 1.05	6.39+/- 0.900	0.0180+/ -0.00182	0.00569+/- 0.000665	0.00487	98.22

Basing on the previous investigation on equi-atomic $L1_0$ FePt, further analysis will include doping element Rh to have the knowledge about its location in the $L1_0$ structure. In order to achieve this objective, the local environment with Rh doping was analyzed by fitting the first shell with combining $L1_0$ FePt and FeRh weighted by the doping concentration of Rh. The reason to fit only the first shell is that outer shells may have significant contribution from the multiple scattering, which needs the exact location of each atom and cannot be determined with this method since it is only based on the occupation possibility. Both fully ordered $L1_0$ FePt and FeRh were used for constructing the model and the relative weightings were from the doping concentration of Rh. The fitting results and fitting parameters are shown and summarized in Fig. 47(a, b) and Table 9, respectively. Both the σ^2 of Fe and Pt were consistent with those from whole range fitting in Table 8. It also showed that the lattice had a monotonous shrinkage in the perpendicular and parallel directions, which

was consistent with the XRD results. The consistence of these fitting results with XRD results implied that the model with Rh located in the Pt plane is valid for our samples. The increased σ^2 in perpendicular direction also confirmed the assumption since it was mainly due to the increase of static disorder in path length brought by the relative smaller radius of Rh. Noted here all EXAFS measurements were done in the same temperature, therefore the variation of σ^2 was due to the static disorder.

Further we applied the fitting parameters from Table 9 to the Rh *K* edge. It was found that a good fitting can only be achieved with the model where $L1_0$ structure remained and Rh was only surrounded with Pt (no Rh). With this model, the fitting results at first shell are shown in Figs. 47c and 47d. From EXAFS analysis, we can then draw the implication that Rh replaced Pt and uniformly distribute in the Pt atomic plane.

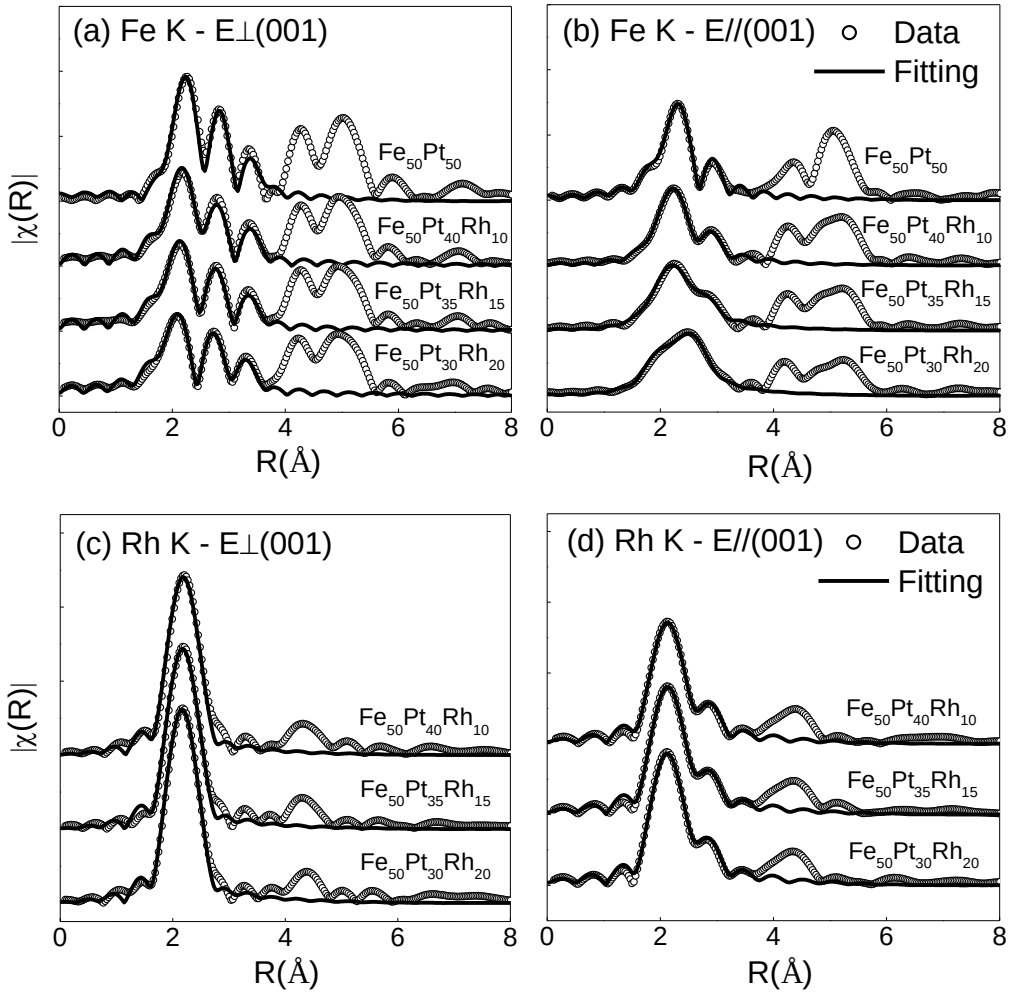

Fig. 47. $\chi(R)$ and theoretical $\chi_{theo}(R)$ at the first shell based on combination of $L1_0$ FePt and FeRh weighted by the corresponding composition for Fe *K* edge in perpendicular (a) and parallel (b) and Rh *K* edge in perpendicular (c) and parallel (d) measurement configurations for $Fe_{50}Pt_{50-x}Rh_x$ (x = 0, 10, 15, 20 at. %).

Table 9. A summary of the parameters used for constructing the model to have the best fitting with the χ(R) for the first shell in perpendicular and parallel measurements for Fe *K* edge in $Fe_{50}Pt_{50-x}Rh_x$ (x=0, 10, 15 and 20).

Parameter	alpha	ΔE-Fe	ΔE-Pt	ΔE-Rh	σ^2-Fe	σ^2-Pt	σ^2-Rh	R-factor
$Fe_{50}Pt_{50}$ – Fe K (⊥)	-0.00419 +/- 0.00492	2.68 +/- 3.21	5.84 +/- 0.764		0.0134 +/- 0.00746	0.00670 +/- 0.00125		0.0215
$Fe_{50}Pt_{40}Rh_{10}$ – Fe K (⊥)	-0.0172 +/- 0.00481	6.44 +/- 2.63	2.26 +/- 1.56	13.3 +/- 2.26	0.0152 +/- 0.00486	0.00591 +/- 0.00126	0.0192 +/- 0.0136	0.00874
$Fe_{50}Pt_{35}Rh_{15}$ – Fe K (⊥)	-0.0250 +/- 0.00638	6.24 +/- 2.60	0.792 +/- 2.25	9.68 +/- 1.63	0.0173 +/- 0.00614	0.00591 +/- 0.00147	0.0183 +/- 0.00867	0.00806
$Fe_{50}Pt_{30}Rh_{20}$ – Fe K (⊥)	-0.0377 +/- 0.00662	6.85 +/- 2.38	-1.34 +/- 2.46	7.31 +/- 1.12	0.0189 +/- 0.00561	0.00587 +/- 0.00133	0.0203 +/- 0.00631	0.00424
$Fe_{50}Pt_{50}$ – Fe K (⫽)	0.00288 +/- 0.00351	9.39 +/- 1.11	6.33 +/- 1.38		0.0162 +/- 0.00172	0.00585 +/- 0.000601		0.00490
$Fe_{50}Pt_{40}Rh_{10}$ – Fe K (⫽)	-0.00828 +/- 0.0515	5.72 +/- 16.2	4.55 +/- 6.22	8.70 +/- 20.8	0.0161 +/- 0.0143	0.00764 +/- 0.00721	0.0134 +/- 0.0538	0.00445
$Fe_{50}Pt_{35}Rh_{15}$ – Fe K (⫽)	-0.0163 +/- 0.0744	3.59 +/- 20.8	4.35 +/- 13.1	6.56 +/- 27.5	0.0156 +/- 0.0170	0.00943 +/- 0.00776	0.0108 +/- 0.0175	0.00747
$Fe_{50}Pt_{30}Rh_{20}$ – Fe K (⫽)	-0.0234 +/- 0.0982	0.893+/- 25.9	4.38 +/- 19.9	6.44 +/- 28.6	0.0157 +/- 0.0187	0.00982 +/- 0.0195	0.00804 +/- 0.00701	0.00802

6.6 DISCUSSION

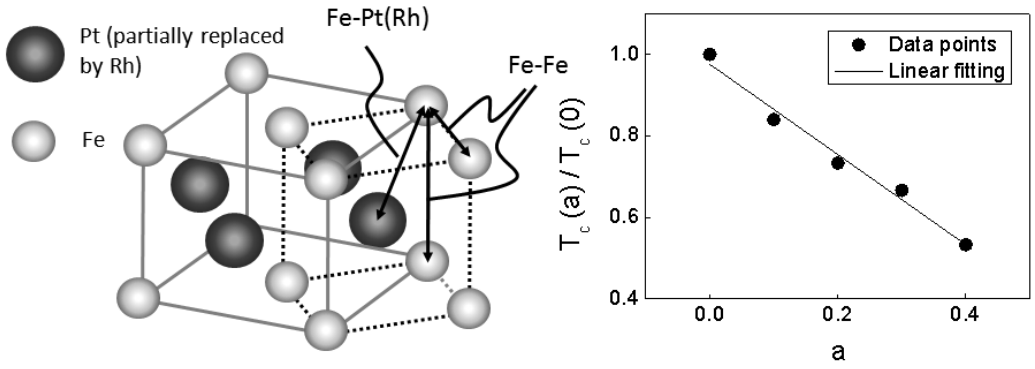

Fig. 48. (left) Atomic model for illustrating the primitive cell where Pt is partially replaced by Rh in the body center; (right) $T_C(a)/T_C(0)$ vs. Rh doing concentration a for Rh doping FePt films, here a is the substitution fraction of Pt with Rh

In order to further investigate the doping effects of Rh, the relation between exchange integral J and T_C was examined by

$$J = \frac{3kT_c}{2zs(s+1)} \tag{6-5}$$

Where s is the magnitude of the spin; k is Boltzmann constant; z is the number of nearest neighbor atoms. Considering the $L1_0$ phase was retained during the doping and S only showed little change, the equation could be simply expressed as $J \propto T_c$. During the estimation, dipolar coupling was neglected between Fe atoms since their contribution was small. It could be concluded that the variation of T_C with Rh doping was mainly due to the change of exchange integral between Fe and Fe after Rh doping. EXAFS results showed that Rh uniformly distributed in FePt and resided in the Pt

plane to replace Pt site. The substitution of Pt with Rh may give rise to the reduction of T_C as well as the variation of exchange integral J. As shown in Fig. 48 (right), the variation of T_C had a proportional relation with Rh doping concentration. By using the linear fit from the equation:

$$\frac{T_c(a)}{T_c(0)} = 1 - ka \tag{6-6}$$

It can be found that good fitting was achieved with the slope k = 1.11. It was similar with Mn doping in the previous report (k = 1.07). This k factor could provide the quantitative criterion to evaluate the effectiveness of reducing T_C.

6.7 SUMMARY

An investigation of m_s and m_l of Fe in $Fe_{50}Pt_{50-x}Rh_x$ films with XMCD in soft XAS region along the easy magnetization axis was presented. The results showed that the magnetic moment of Fe contributed to most of the magnetization. The decrease of m_l implied a decrease of MCA, whereas the decrease of m_s was consistent with the FM to AFM transition at above 15 at. % of Rh. The increase of m_l/m_s with Rh doping concentration suggested that the doping of Rh in FePt had a significant influence on the spin-orbital interaction.

Rh doped $L1_0$ FePt has attracted much attention due to its continuous modification on electronic structure of FePt while retaining the ordered $L1_0$ phase. Temperature-dependent magnetic measurement showed that the saturation magnetization M_s (magnetic anisotropy K_u) was reduced from 1152 emu/cc (5×10^7

erg/cc) to 141 emu/cc (1.95×10^6 erg/cc) with 20 at. % of Rh doped. Meanwhile, T_C was reduced from 750 ^oC to 400 ^oC. The analysis of EXAFS results showed that Rh uniformly distributed in $L1_0$ FePt and replaced the Pt site. The substitution of Pt with Rh affected the exchange integral. A k factor of 1.11 was derived to evaluate the effectiveness of reducing T_C with doping element.

VII. CONCLUSION AND FUTURE WORK

This Chapter summarizes and highlights the key results of this thesis. Future work related to this conclusion is also suggested.

7.1 CONCLUSION

Compositional effects on structure and temperature-dependent magnetic properties in $L1_0$ FePt epitaxial thin films were studied. The highest chemical ordering S, saturation magnetization M_s and anisotropy K_u were all found at the equiatomic composition. It showed that excess Pt had a more profound effect on reducing T_C than the excess Fe. Further dynamical investigation with time-resolved laser-pump X-ray-probe XRD on equatomic FePt film extended our understanding on its application in HAMR. Our findings showed that the cooling rate could be enhanced with the Ag heat sink layer. However, the highest temperature and the duration at high temperature were reduced at the same time. A tradeoff between these should therefore be made or an adjustable thermal control at the interface is required.

The investigations of Nd doped $L1_0$ ordered $Fe_{50}Pt_{50-x}Nd_x$ thin films showed a large enhancement of magnetic moment with a composition of Nd at x = 6 at. %. Analysis of the XMCD spectra at the $L_{3,2}$ edges of Fe and $M_{5,4}$ edges of Nd in $Fe_{50}Pt_{44}Nd_6$ films indicated a significant contribution of the Nd orbital moment. The origin of the large enhancement of magnetic moment was attributed to the effect of ferromagnetic coupling of the total magnetic moments between Fe and Nd. Further first-principle calculations also support this observation. Further

temperature-dependent magnetic properties for this series samples were not conducted due to the deterioration of perpendicular texture when Nd doping concentration exceeded 6 at. %.

The Mn doping effects on structure showed that *c*, *S*, K_u and T_C monotonously decreased with increasing Mn concentration. With 15 at. % Mn added, T_C could be reduced to around 500 K and the magnetic anisotropy was reduced to 1.6×10^7 erg/cc simultaneously. It indicated that doping with Mn was more effective in reducing T_c and maintaining K_u than Ni did. The reduction of *T*c was mainly due to the substitution of Fe with Mn in $L1_0$ FePt as revealed from DSRO investigation.

Further temperature-dependent magnetic measurement on Rh doped $L1_0$ FePt showed that the saturation magnetization M_s (magnetic anisotropy K_u) was reduced from 1152 emu/cc (5×10^7 erg/cc) to 141 emu/cc (1.95×10^6 erg/cc) with 20 at. % of Rh doped. Meanwhile, T_C was reduced from 750 ^oC to 400 ^oC. The analysis of EXAFS results show that Rh uniformly distributed in $L1_0$ FePt and replaced Pt site. The substitution of Pt with Rh affected the exchange integral. A *k* factor of 1.11 was derived to evaluate the effectiveness of reducing T_C with doping element, which was slightly higher than that with Mn doping in the previous report (k = 1.07). Both Mn and Rh doping elements showed higher effectiveness of reducing T_C than Ni when retain the same K_u.

7.2 FUTURE WORK

Our previous conclusion showed that both Mn and Rh showed significant effects on reducing T_C and retain the K_u. Though the composition and Nd, Mn and Rh doping effects have been investigated in details, there remain many other elements that can be of potential use. Future work on the effects of additional doping elements on the temperature-dependent properties is of interests for the optimization of the requirement of HAMR media with low T_C and high K_u.

VIII. REFERENCE

[1] "Data, data everywhere," [Online]. Available: http://www.economist.com/node/15557443/print4%20sur.

[2] "All too much Monstrous amounts of data," [Online]. Available: http://www.economist.com/node/15557421.

[3] "Seagate Breaks Areal Density Barrier: Unveiling the World's First Hard Drive Featuring One Terabyte per Platter," [Online]. Available: http://www.seagate.com/gb/en/about/newsroom/press-releases/unveils-1-terabyte-platter-seagate-pr/.

[4] R. Wood, "Future hard disk drive systems," *J. Magn. Magn. Mater.*, vol. 321, no. 6, pp. 555-561, 2009.

[5] "Kryder's Law," [Online]. Available: http://www.scientificamerican.com/article.cfm?id=kryders-law.

[6] "Moore's law," [Online]. Available: http://en.wikipedia.org/wiki/Moore's_law.

[7] G. E. Moore, "Cramming More Components Onto Integrated Circuits," *Proc. IEEE*, vol. 86, no. 1, pp. 82-85, 1998.

[8] H. N. Bertram and M. Williams, "SNR and density limit estimates: A comparison of longitudinal and perpendicular recording," *IEEE Trans. Magn.*, vol. 36, no. 1, pp. 4-9, 2000.

[9] R. H. Victora, J. H. Xue and M. Patwari, "Areal density limits for perpendicular magnetic recording," *IEEE Trans. Magn.*, vol. 38, no. 5, pp. 1886-1891, 2002.

[10] S. Iwasaki and K. Takemura, "An analysis for the circular mode of magnetization in short wavelength recording," *IEEE Trans. Magn.*, vol. 11, no. 5, pp. 1173-1175, 1975.

[11] R. H. Victora and S. Xiao, "Composite media for perpendicular magnetic recording," *IEEE Trans. Magn.*, vol. 41, no. 2, pp. 537-542, 2005.

[12] W. K. Shen, J. M. Bai, R. H. Victora, J. H. Judy and J. P. Wang, "Composite perpendicular magnetic recording media using [Co/PdSi]n as a hard layer and FeSiO as a soft layer," *J. Appl. Phys.*, vol. 97, no. 10, pp. 10N513-10N513, 2005.

[13] J. P. Wang, W. K. Shen and J. Bai, "Exchange coupled composite media for perpendicular magnetic recording," *IEEE Trans. Magn.*, vol. 41, no. 10, pp. 3181-3186, 2005.

[14] H. J. Richter and A. Y. Dobin, "Angle effects at high-density magnetic recording," *J. Magn. Magn. Mater.*, vol. 287, pp. 41-50, 2005.

[15] D. Suess, T. Schrefl, S. Fähler, M. Kirschner, G. Hrkac and F. Dorfbauer *et al.*, "Exchange spring media for perpendicular recording," *Appl. Phys. Lett.*, vol. 87, no. 1, pp. 012504, 2005.

[16] Z. H. Lu, P. B. Visscher and W. H. Butler, "Domain Wall Switching: Optimizing the Energy Landscape," *IEEE Trans. Magn.*, vol. 43, no. 6, pp. 2941-2943, 2007.

[17] A. Y. Dobin and H. J. Richter, "Domain wall assisted magnetic recording," *Appl. Phys. Lett.*, vol. 89, no. 6, pp. 062512, 2006.

[18] R. H. Victora and X. Shen, "Exchange Coupled Composite Media," *Proc. IEEE*, vol. 96, no. 11, pp. 1799-1809, 2008.

[19] Y. Shiroishi, K. Fukuda, I. Tagawa, H. Iwasaki, S. Takenoiri and H. Tanaka *et al.*, "Future Options for HDD Storage," *IEEE Trans. Magn.*, vol. 45, no. 10, pp. 3816-3822, 2009.

[20] E. A. Dobisz, Z. Z. Bandic, T. W. Wu and T. Albrecht, "Patterned Media: Nanofabrication Challenges of Future Disk Drives," *Proc. IEEE*, vol. 96, no. 11, pp. 1836-1846, 2008.

[21] M. D. Austin, H. X. Ge, W. Wu, M. T. Li, Z. N. Yu and D. Wasserman *et al.*, "Fabrication of 5 nm linewidth and 14 nm pitch features by nanoimprint lithography," *Appl. Phys. Lett.*, vol. 84, no. 26, pp. 5299, 2004.

[22] E. E. Nunez, C. D. Yeo, R. R. Katta and A. A. Polycarpou, "Effect of Planarization on the Contact Behavior of Patterned Media," *IEEE Trans. Magn.*, vol. 44, no. 11, pp. 3667-3670, 2008.

[23] M. H. Kryder, E. C. Gage, T. W. McDaniel, W. A. Challener, R. E. Rottmayer and G. P. Ju *et al.*, "Heat Assisted Magnetic Recording," *Proc. IEEE*, vol. 96, no. 11, pp. 1810-1835, 2008.

[24] N. Kazantseva, D. Hinzke, R. W. Chantrell and U. Nowak, "Linear and elliptical magnetization reversal close to the Curie temperature," *Europhys. Lett.,* vol. 86, no. 2, pp. 27006, 2009.

[25] V. W. Guo, B. Lu, X. W. Wu, G. P. Ju, B. Valcu and D. Weller, "A survey of anisotropy measurement techniques and study of thickness effect on interfacial and volume anisotropies in Co/Pt multilayer media," *J. Appl. Phys.,* vol. 99, no. 8, pp. 08E918, 2006.

[26] Y. Kawada, Y. Ueno and K. Shibata, "Co-Pt multilayers perpendicular magnetic recording media with thin Pt layer and high perpendicular anisotropy," *IEEE Trans. Magn.,* vol. 38, no. 5, pp. 2045-2047, 2002.

[27] T. Asahi, I. Koizumi, Y. Egawa, M. Yoshino, A. Sugiyama and J. Hokkyo *et al*., "Improvement of magnetic intergranular isolation and evaluation of read/write characteristics on SmCo5 perpendicular magnetic thin films," *J. Magn. Magn. Mater.,* vol. 322, no. 23, pp. 3784-3788, 2010.

[28] M. Seifert, V. Neu and L. Schultz, "Epitaxial SmCo5 thin films with perpendicular anisotropy," *Appl. Phys. Lett.,* vol. 94, no. 2, pp. 022501, 2009.

[29] J. Sayama, K. Mizutani, T. Asahi, J. Ariake, K. Ouchi and S. Matsunuma *et al*., "Magnetic properties and microstructure of SmCo5 thin film with perpendicular magnetic anisotropy," *J. Magn. Magn. Mater.,* vol. 287, pp. 239-244, 2005.

[30] D. Weller, A. Moser, L. Folks, M. E. Best, L. Wen and M. F. Toney *et al*., "High Ku materials approach to 100 Gbits/in2," *IEEE Trans. Magn.,* vol. 36, no. 1, pp. 10-15, 2000.

[31] T. Klemmer, D. Hoydick, H. Okumura, B. Zhang and W. A. Soffa, "Magnetic hardening and coercivity mechanisms in L10 ordered FePd ferromagnets," *Scr. Metall. Mater.,* vol. 33, no. 10-11, pp. 1793-1805, 1995.

[32] T. B. Massalski and H. Okamoto, T. B. Massalski and H. Okamoto, Eds., *Binary Alloy Phase Diagrams,* ASM International, 1990.

[33] M. S. Seehra, V. Singh, P. Dutta, S. Neeleshwar, Y. Y. Chen and C. L. Chen *et al*., "Size-dependent magnetic parameters of fcc FePt nanoparticles: applications to magnetic hyperthermia," *J. Phys. D: Appl. Phys.,* vol. 43, no. 14, pp. 145002, 2010.

[34] Cebollada A, Farrow R F C and Toney M F, H. S. Nalwa, Eds., *Magnetic Nanostructures,* California: American Scientific Publisher, 2002.

[35] P. Ravindran, A. Kjekshus, H. Fjellvåg, P. James, L. Nordström and B. Johansson *et al.*, "Large magnetocrystalline anisotropy in bilayer transition metal phases from first-principles full-potential calculations," *Phys. Rev. B,* vol. 63, no. 14, pp. 144409, 2001.

[36] N. Nakajima, T. Koide, T. Shidara, H. Miyauchi, H. Fukutani and A. Fujimori *et al.*, "Perpendicular Magnetic Anisotropy Caused by Interfacial Hybridization via Enhanced Orbital Moment in Co/Pt Multilayers: Magnetic Circular X-Ray Dichroism Study," *Phys. Rev. Lett.,* vol. 81, no. 23, pp. 5229-5232, 1998.

[37] J. U. Thiele, K. R. Coffey, M. F. Toney, J. A. Hedstrom and A. J. Kellock, "Temperature dependent magnetic properties of highly chemically ordered Fe55−xNixPt45L10 films," *J. Appl. Phys.,* vol. 91, no. 10, pp. 6595, 2002.

[38] S. Okamoto, N. Kikuchi, O. Kitakami, T. Miyazaki, Y. Shimada and K. Fukamichi, "Chemical-order-dependent magnetic anisotropy and exchange stiffness constant of FePt (001) epitaxial films," *Phys. Rev. B,* vol. 66, no. 2, pp. 024413, 2002.

[39] O. N. Mryasov, K. Y. Guslienko, U. Nowak and R. W. Chantrell, "Temperature-dependent magnetic properties of FePt: Effective spin Hamiltonian model," *Europhys. Lett.,* vol. 69, pp. 805-811, 2005.

[40] P. Asselin, R. F. L. Evans, J. Barker, R. W. Chantrell, R. Yanes and O. Chubykalo-Fesenko *et al.*, "Constrained Monte Carlo method and calculation of the temperature dependence of magnetic anisotropy," *Phys. Rev. B,* vol. 82, no. 5, pp. 054415, 2010.

[41] C. L. Platt, K. W. Wierman, E. B. Svedberg, R. van de Veerdonk, J. K. Howard and A. G. Roy *et al.*, "L–10 ordering and microstructure of FePt thin films with Cu, Ag, and Au additive," *J. Appl. Phys.,* vol. 92, no. 10, pp. 6104, 2002.

[42] T. Maeda, T. Kai, A. Kikitsu, T. Nagase and J. I. Akiyama, "Reduction of ordering temperature of an FePt-ordered alloy by addition of Cu," *Appl. Phys. Lett.,* vol. 80, no. 12, pp. 2147-2149, 2002.

[43] X. C. Sun, S. S. Kang, J. W. Harrell, D. E. Nikles, Z. R. Dai and J. Li *et al.*, "Synthesis, chemical ordering, and magnetic properties of FePtCu nanoparticle films," *J Chem Phys,* vol. 93, no. 10, pp. 7337-7339, 2003.

[44] W. Y. Zhang, H. Shima, F. Takano, H. Akinaga, X. Z. Yu and T. Hara *et al*., "Enhancement in ordering of Fe50Pt50 film caused by Cr and Cu additives," *J. Appl. Phys.*, vol. 106, no. 3, pp. 033907, 2009.

[45] D. Ravelosona, C. Chappert, V. Mathet and H. Bernas, "Chemical order induced by ion irradiation in FePt (001) films," *Appl. Phys. Lett.*, vol. 76, no. 2, pp. 236-238, 2000.

[46] A. C. Sun, F. T. Yuan, J. H. Hsu, W. M. Liao and H. Y. Lee, "Effect of bombardment with different ions H He Ar on ordering transformation of Fe48Pt52 films," *J. Appl. Phys.*, vol. 105, no. 7, pp. 07B719, 2009.

[47] X. L. Shu, Z. Y. Chen, Q. Chen and W. Y. Hu, "The effect of vacancy created by ion irradiation on the ordering of FePt: A first-principle study," *Nucl. Instrum. Methods Phys. Res. Sect. B-Beam Interact. Mater. Atoms*, vol. 267, no. 18, pp. 3271-3273, 2009.

[48] B. Yao and K. R. Coffey, "The influence of periodicity on the structures and properties of annealed [Fe/Pt]n multilayer films," *J Chem Phys*, vol. 320, no. 3–4, pp. 559-564, 2008.

[49] Y. Ogata, Y. Imai and S. Nakagawa, "Effect of multilayer configuration of [Fe/Pt] multilayer to attain (001) oriented FePt ordered alloy thin films," *J. Appl. Phys.*, vol. 107, no. 9, pp. 09A715, 2010.

[50] T. Suzuki, K. Harada, N. Honda and K. Ouchi, "Preparation of ordered Fe–Pt thin films for perpendicular magnetic recording media," *J Chem Phys*, vol. 193, no. 1–3, pp. 85-88, 1999.

[51] J. S. Chen, B. C. Lim, J. F. Hu, Y. K. Lim, B. Liu and G. M. Chow, "High coercivity L10 FePt films with perpendicular anisotropy deposited on glass substrate at reduced temperature," *Appl. Phys. Lett.*, vol. 90, no. 4, pp. 042508, 2007.

[52] J. S. Chen, B. C. Lim, J. F. Hu, B. Liu, G. M. Chow and G. Ju, "Low temperature deposited L10 FePt-C (001) films with high coercivity and small grain size," *Appl. Phys. Lett.*, vol. 91, no. 13, pp. 132506, 2007.

[53] S. N. Hsiao, F. T. Yuan, H. W. Chang, H. W. Huang, S. K. Chen and H. Y. Lee, "Effect of initial stress/strain state on order-disorder transformation of FePt thin films," *Appl. Phys. Lett.*, vol. 94, no. 23, pp. 232505, 2009.

[54] K. Barmak, J. Kim, L. H. Lewis, K. R. Coffey, M. F. Toney and A. J. Kellock *et al*., "On the relationship of magnetocrystalline anisotropy and stoichiometry in epitaxial L10 CoPt (001) and FePt (001) thin films," *J. Appl. Phys.*, vol. 98, no. 3, pp. 033904, 2005.

[55] K. Barmak, J. Kim, L. H. Lewis, K. R. Coffey, M. F. Toney and A. J. Kellock *et al*., "Stoichiometry–anisotropy connections in epitaxial L10 FePt(001) films," *J. Appl. Phys.*, vol. 95, no. 11, pp. 7501, 2004.

[56] M. L. Yan, H. Zeng, N. Powers and D. J. Sellmyer, "L10,(001)-oriented FePt:B2O3 composite films for perpendicular recording," *J. Appl. Phys.*, vol. 91, no. 10, pp. 8471, 2002.

[57] M. L. Yan, N. Powers and D. J. Sellmyer, "Highly oriented nonepitaxially grown L10 FePt films," *J. Appl. Phys.*, vol. 93, no. 10, pp. 8292, 2003.

[58] J. L. Tsai, F. T. Yuan and S. K. Chen, "Magnetic properties and domain structure of highly coercive Au/FePt films," *J. Appl. Phys.*, vol. 97, no. 10, pp. 10N122, 2005.

[59] D. H. Ping, M. Ohnuma, K. Hono, M. Watanabe, T. Iwasa and T. Masumoto, "Microstructures of FePt-Al-O and FePt-Ag nanogranular thin films and their magnetic properties," *J. Appl. Phys.*, vol. 90, no. 9, pp. 4708-4716, 2001.

[60] Y. C. Wu, L. W. Wang and C. H. Lai, "Low-temperature ordering of (001) granular FePt films by inserting ultrathin SiO2 layers," *Appl. Phys. Lett.*, vol. 91, no. 7, pp. 072502, 2007.

[61] J. S. Chen, B. C. Lim, Y. F. Ding, J. F. Hu, G. M. Chow and G. Ju, "Granular L10 FePt–X (X = C, TiO2, Ta2O5) (001) nanocomposite films with small grain size for high density magnetic recording," *J. Appl. Phys.*, vol. 105, no. 7, pp. 07B702, 2009.

[62] J. S. Chen, T. J. Zhou, Y. F. Ding, B. C. Lim and B. Liu, "Microstructure and magnetic properties of rapidly annealed FePt (001) and FePt–MgO (001) films," *J. Appl. Phys.*, vol. 97, no. 10, pp. 10N108, 2005.

[63] T. Suzuki, H. Muraoka, Y. Nakamura and K. Ouchi, "Design and recording properties of Fe-Pt perpendicular media," *IEEE Trans. Magn.*, vol. 39, no. 2, pp. 691-696, 2003.

[64] J. S. Chen, Y. Z. Zhou, B. C. Lim, T. J. Zhou, J. Zhang and G. M. Chow, "Improvement of recording performance in FePt perpendicular media by Ag pinning layer," *IEEE Trans. Magn.*, vol. 41, no. 10, pp. 3196-3198, 2005.

[65] T. J. Zhou, B. C. Lim and B. Liu, "Anisotropy graded FePt-TiO2 nanocomposite thin films with small grain size," *Appl. Phys. Lett.*, vol. 94, no. 15, pp. 152505, 2009.

[66] T. A. George, Z. Li, M. L. Yan, Y. F. Xu, R. Skomski and D. J. Sellmyer, "Nanostructure and magnetic properties of L10 FePt:X films," *J. Appl. Phys.*, vol. 103, no. 7, pp. 07D502, 2008.

[67] H. M. Lu, Z. H. Cao, C. L. Zhao, P. Y. Li and X. K. Meng, "Size-dependent ordering and Curie temperatures of FePt nanoparticles," *J. Appl. Phys.*, vol. 103, no. 12, pp. 123526, 2008.

[68] H. Zeng, R. Sabirianov, O. Mryasov, M. L. Yan, K. Cho and D. J. Sellmyer, "Curie temperature of FePt:B2O3 nanocomposite films," *Phys. Rev. B*, vol. 66, no. 18, pp. 184425, 2002.

[69] B. R. Knight, J. A. Bain and T. E. Schlesinger, "HAMR Adjacent Track Stability in the Presence of a Medium Curie Temperature Distribution," *IEEE Trans. Magn.*, vol. 46, no. 6, pp. 2462-2465, 2010.

[70] D. B. Xu, J. S. Chen, T. J. Zhou and G. M. Chow, "Effects of Mn doping on temperature-dependent magnetic properties of L10 FeMnPt," *J. Appl. Phys.*, vol. 109, no. 7, pp. 07B747, 2011.

[71] E. Betzig, J. K. Trautman, R. Wolfe, E. M. Gyorgy, P. L. Finn and M. H. Kryder *et al.*, "Near-field magneto-optics and high density data storage," *Appl. Phys. Lett.*, vol. 61, no. 2, pp. 142-144, 1992.

[72] B. D. Terris, H. J. Mamin, D. Rugar, W. R. Studenmund and G. S. Kino, "Near-field optical data storage using a solid immersion lens," *Appl. Phys. Lett.*, vol. 65, no. 4, pp. 388-390, 1994.

[73] H. Sukeda, H. Saga, H. Nemoto, Y. Itou, C. Haginoya and T. Matsumoto, "Thermally assisted magnetic recording on flux-detectable RE-TM media," *J Chem Phys*, vol. 37, no. 4, pp. 1234-1238, 2001.

[74] L. G. Parratt, "Surface Studies of Solids by Total Reflection of X-Rays," *Phys. Rev.*, vol. 95, no. 2, pp. 359-369, 1954.

[75] V. Holy, U. Pietsch and T. Baumbach, V. Holy, Eds., *High-Resolution X-Ray Scattering from Thin Films and Multilayers,* Springer Verlag, 1999.

[76] R. N. Ramesh, Y. N. Hua, K. Li and K. F. Lo, "Studies on X-ray reflectivity technique and application in thickness measurements in wafer fabrication," *in Semiconductor Electronics, 2004. ICSE 2004. IEEE International Conference on,* 2004.

[77] J. J. Rehr and R. C. Albers, "Theoretical approaches to x-ray absorption fine structure," *Rev. Mod. Phys.,* vol. 72, no. 3, pp. 621-654, 2000.

[78] P. A. Lee, P. H. Citrin, P. Eisenberger and B. M. Kincaid, "Extended x-ray absorption fine structure—its strengths and limitations as a structural tool," *Rev. Mod. Phys.,* vol. 53, no. 4, pp. 769-806, 1981.

[79] E. Sayers and B. Bunker, "X-Ray Absorption: Principles, Applications, Techniques of EXAFS, SEXAFS, and XANES," *in Chemical Analysis: A Series of Monographs on Analytical Chemistry and Its Applications,* vol. 92, D. C. Koningsberger and R. Prins, Ed. New York:Wiley-Interscience, pp. 443-571, 1988.

[80] D. C. Koningsberger, B. L. Mojet, G. E. V. Dorssen and D. E. Ramaker, "XAFS Spectroscopy : Fundamental Principles and Data Analysis," *Topics in Catalysis,* vol. 10, no. 3-4, pp. 143-155, 2000.

[81] S. I. Zabinsky, J. J. Rehr, A. Ankudinov, R. C. Albers and M. J. Eller, "Multiple-scattering calculations of x-ray-absorption spectra," *Phys. Rev. B,* vol. 52, no. 4, pp. 2995-3009, 1995.

[82] J. Lindemuth, J. Krause and B. Dodrill, "Finite sample size effects on the calibration of vibrating sample magnetometer," *IEEE Trans. Magn.,* vol. 37, no. 4, pp. 2752-2754, 2001.

[83] J. Stöhr and H. C. Siegmann, *Magnetism: From Fundamentals to Nanoscale Dynamics,* Springer, 2006.

[84] E. Beaurepaire, H. Bulou, F. Scheurer and J. P. Kappler, *Magnetism and Synchrotron Radiation: New Trends,* Springer, 2010.

[85] P. Carra, B. T. Thole, M. Altarelli and X. D. Wang, "X-ray circular dichroism and local magnetic fields," *Phys. Rev. Lett.,* vol. 70, no. 5, pp. 694-697, 1993.

[86] B. T. Thole, P. Carra, F. Sette and G. V. D. Laan, "X-ray circular dichroism as a probe of orbital magnetization," *Phys. Rev. Lett.*, vol. 68, no. 12, pp. 1943-1946, 1992.

[87] H. J. Elmers, G. H. Fecher, D. Valdaitsev, S. A. Nepijko, A. Gloskovskii and G. Jakob *et al.*, "Element-specific magnetic moments from core-absorption magnetic circular dichroism of the doped Heusler alloy Co2Cr0.6Fe0.4Al," *Phys. Rev. B*, vol. 67, no. 10, pp. 104412, 2003.

[88] M. F. Toney, J. N. Howard, J. Richer, G. L. Borges, J. G. Gordon and O. R. Melroy *et al.*, "Electrochemical deposition of copper on a gold electrode in sulfuric acid: resolution of the interfacial structure," *Phys Rev Lett*, vol. 75, no. 24, pp. 4472-4475, 1995.

[89] J. U. Thiele, L. Folks, M. F. Toney and D. K. Weller, "Perpendicular magnetic anisotropy and magnetic domain structure in sputtered epitaxial FePt (001) L10 films," *J. Appl. Phys.*, vol. 84, no. 10, pp. 5686, 1998.

[90] J. B. Nelson and D. P. Riley, "An experimental investigation of extrapolation methods in the derivation of accurate unit-cell dimensions of crystals," *Proc. Phys. Soc.*, vol. 57, no. 3, pp. 160, 1945.

[91] R. F. C. Farrow, D. Weller, R. F. Marks, M. F. Toney, A. Cebollada and G. R. Harp, "Control of the axis of chemical ordering and magnetic anisotropy in epitaxial FePt films," *J. Appl. Phys.*, vol. 79, no. 8, pp. 5967, 1996.

[92] Z. H. Lu, R. V. Chepulskii and W. H. Butler, "First-principles study of magnetic properties of L10-ordered MnPt and FePt alloys," *Phys. Rev. B*, vol. 81, no. 9, pp. 094437, 2010.

[93] H. B. Callen and E. Callen, "The present status of the temperature dependence of magnetocrystalline anisotropy, and the power law," *J. Phys. Chem. Solids*, vol. 27, no. 8, pp. 1271-1285, 1966.

[94] J. S. Chen, J. F. Hu, B. C. Lim, W. L. Phyoe, B. Liu and G. Ju, "Structure and magnetic properties of L10 FePt film with Ag heat sink layer," *J. Appl. Phys.*, vol. 105, no. 7, pp. 07B724, 2009.

[95] R. Fernandez, D. Teweldebrhan, C. Zhang, A. Balandin and S. Khizroev, "A comparative analysis of Ag and Cu heat sink layers in L10-FePt films for heat-assisted magnetic recording," *J. Appl. Phys.*, vol. 109, no. 7, pp. 07B763, 2011.

[96] C. Rose-Petruck, R. Jimenez, T. Guo, A. Cavalleri, C. W. Siders and F. Rksi *et al.*, "Picosecond–milliångström lattice dynamics measured by ultrafast X-ray diffraction," *Nature,* vol. 398, no. 6725, pp. 310-312, 1999.

[97] A. S. Edward and B. Dale, "Delay of laser excited electron/hole interaction with germanium lattice," *J. Phys.: Conf. Ser.,* vol. 190, no. 1, pp. 012053, 2009.

[98] S. D. Brorson, J. G. Fujimoto and E. P. Ippen, "Femtosecond electronic heat-transport dynamics in thin gold films," *Phys. Rev. Lett.,* vol. 59, no. 17, pp. 1962-1965, 1987.

[99] T. Guray and H. J. Maris, "Electron diffusion in metals studied by picosecond ultrasonics," *Phys. Rev. B,* vol. 49, no. 21, pp. 15046-15054, 1994.

[100] S. Volz and R. Carminati, *Microscale and nanoscale heat transfer,* Springer Verlag, 2007.

[101] A. Plech, S. Kürbitz, K. J. Berg, H. Graener, G. Berg and S. Grésillon *et al.*, "Time-resolved X-ray diffraction on laser-excited metal nanoparticles," *Europhys. Lett.,* vol. 61, no. 6, pp. 762, 2003.

[102] J. V. Goicochea and B. Michel, "Impact of electron-phonon transport on the thermal resistance of metal-nonmetal interfaces," *in Semiconductor Thermal Measurement and Management Symposium (SEMI-THERM), 2011 27th Annual IEEE,* pp. 155-160, 2011.

[103] B. Feng, Z. X. Li and X. Zhang, "Role of phonon in the thermal and electrical transports in metallic nanofilms," *J. Appl. Phys.,* vol. 105, no. 10, pp. 104315, 2009.

[104] M. L. Huberman and A. W. Overhauser, "Electronic Kapitza conductance at a diamond-Pb interface," *Phys. Rev. B,* vol. 50, no. 5, pp. 2865-2873, 1994.

[105] G. D. Mahan, "Kapitza thermal resistance between a metal and a nonmetal," *Phys. Rev. B,* vol. 79, no. 7, pp. 075408, 2009.

[106] A. Majumdar and P. Reddy, "Role of electron--phonon coupling in thermal conductance of metal--nonmetal interfaces," *Appl. Phys. Lett.,* vol. 84, no. 23, pp. 4768-4770, 2004.

[107] B. C. Gundrum, D. G. Cahill and R. S. Averback, "Thermal conductance of metal-metal interfaces," *Phys. Rev. B,* vol. 72, no. 24, pp. 245426, 2005.

[108] J. Chen, W. K. Chen, J. Tang and P. M. Rentzepis, "Time-resolved structural dynamics of thin metal films heated with femtosecond optical pulses," *Proc. Natl. Acad. Sci. U S A.*, vol. 108, no. 47, pp. 18887-18892, 2011.

[109] "Refractive Index Database," [Online]. Available: http://refractiveindex.info.

[110] K. Sato, A. Mizusawa, K. Ishida, T. Seki, T. Shima and K. Takanashi, "Magneto-Optical Spectra of Ordered and Disordered FePt Films Prepared at Reduced Temperatures," *Trans. Magn. Soc. Jpn.*, vol. 4, no. 4-2, pp. 297-300, 2004.

[111] Y. B. Band, *Light and Matter: Electromagnetism, Optics, Spectroscopy and Lasers Volume 1 of Light and Matter*, John Wiley & Sons, 2006.

[112] M. Nicoul, U. Shymanovich, A. Tarasevitch, D. V. D. Linde and S. T. Klaus, "Picosecond acoustic response of a laser-heated gold-film studied with time-resolved x-ray diffraction," *Appl. Phys. Lett.*, vol. 98, no. 19, pp. 191902, 2011.

[113] A. Cavalleri, C. W. Siders, F. L. H. Brown, D. M. Leitner, C. Tóth and J. A. Squier *et al.*, "Anharmonic Lattice Dynamics in Germanium Measured with Ultrafast X-Ray Diffraction," *Phys. Rev. Lett.*, vol. 85, no. 3, pp. 586-589, 2000.

[114] M. Perner, S. Gresillon, J. März, G. V. Plessen, J. Feldmann and J. Porstendorfer *et al.*, "Observation of Hot-Electron Pressure in the Vibration Dynamics of Metal Nanoparticles," *Phys. Rev. Lett.*, vol. 85, no. 4, pp. 792-795, 2000.

[115] N. Kazantseva, U. Nowak, R. W. Chantrell, J. Hohlfeld and A. Rebei, "Slow recovery of the magnetisation after a sub-picosecond heat pulse," *Europhys. Lett.*, vol. 81, no. 2, pp. 27004, 2008.

[116] S. Akimasa, "First Principle Calculation of the Magnetocrystalline Anisotropy Energy of FePt and CoPt Ordered Alloys," *J. Phys. Soc. Jpn.*, vol. 63, pp. 3053-3058, 1994.

[117] E. Burzo, "Magnetic properties and exchange interaction in rare-earth-iron-based compounds," *Romanian Reports in Physics*, vol. 63, pp. 1316-1328, 2011.

[118] C. J. Sun, D. B. Xu, S. M. Heald, J. S. Chen and G. M. Chow, "Directional short range order in L10 FeMnPt magnetic thin films," *Phys. Rev. B*, vol. 84, no. 14, pp. 140408(R), 2011.

[119] C. T. Chen, Y. U. Idzerda, H. J. Lin, N. V. Smith, G. Meigs and E. Chaban *et al*., "Experimental Confirmation of the X-Ray Magnetic Circular Dichroism Sum Rules for Iron and Cobalt," *Phys. Rev. Lett.,* vol. 75, no. 1, pp. 152-155, 1995.

[120] J. M. Esteva, R. C. Karnatak, J. C. Fuggle and G. A. Sawatzky, "Selection Rules and Multiplet Effects in Comparison of X-Ray Absorption and Photoemission Peak Energies," *Phys. Rev. Lett.,* vol. 50, no. 12, pp. 910-913, 1983.

[121] Y. Teramura, A. Tanaka, B. T. Thole and T. Jo, "Effect of Coulomb Interaction on the X-Ray Magnetic Circular Dichroism Spin Sum Rule in Rare Earths," *J. Phys. Soc. Jpn.,* vol. 65, no. 9, pp. 3056-3059, 1996.

[122] R. Cid, J. D áz, L. M. Álvarez-Prado, J. M. Alameda, S. M. Valvidares and J. C. Cezar *et al*., "Microscopic origin of perpendicular magnetic anisotropy in amorphous Nd-Co homogeneous and compositionally modulated, thin films studied by XMCD," *J. Phys.: Conf. Ser.,* vol. 200, no. 7, pp. 072017, 2010.

[123] D. J. Keavney, E. E. Fullerton, D. Li, C. H. Sowers, S. D. Bader and K. Goodman *et al*., "Enhanced Co orbital moments in Co–rare-earth permanent-magnet films," *Phys. Rev. B,* vol. 57, no. 9, pp. 5291-5297, 1998.

[124] K. H. J. Buschow, "New developments in hard magnetic materials," *Reports on Progress in Physics,* vol. 54, no. 9, pp. 1123, 1991.

[125] S. Imada, T. Muro, S. Suga, K. Kobayashi, H. Maruyama and H. Yamazaki, "MCD in soft x-ray absorption of Nd2Fe14B," *Journal of Electron Spectroscopy and Related Phenomena,* vol. 78, pp. 279-282, 1996.

[126] G. Kresse and J. Hafner, "Ab initio molecular dynamics for liquid metals," *Phys. Rev. B,* vol. 47, no. 1, pp. 558-561, 1993.

[127] G. Kresse and J. Furthm üller, "Efficient iterative schemes for ab initio total-energy calculations using a plane-wave basis set," *Phys. Rev. B,* vol. 54, no. 16, pp. 11169-11186, 1996.

[128] A. H. Reshak, M. Piasecki, S. Auluck, I. V. Kityk, R. Khenata and B. Andriyevsky *et al*., "Effect of U on the electronic properties of neodymium gallate (NdGaO3): theoretical and experimental studies," *J Phys Chem B.,* vol. 113, no. 46, pp. 15237-15242, 2009.

[129] T. Burkert, O. Eriksson, S. I. Simak, A. V. Ruban, B. Sanyal and L. Nordström *et al.*, "Magnetic anisotropy of L10 FePt and Fe1−xMnxPt," *Phys. Rev. B,* vol. 71, no. 13, pp. 134411, 2005.

[130] D. C. Berry, J. Kim, K. Barmak, K. Wierman, E. B. Svedberg and J. K. Howard, "Differential scanning calorimetry studies of the effect of Cu on the A1 to L10 transformation in FePt thin films," *J Chem Phys,* vol. 53, no. 4, pp. 423-428, 2005.

[131] L. Belliard, J. Miltat, V. Kottler, V. Mathet, C. Chappert, and T. Valet, "Stripe domains morphology versus layers thickness in CoPt multilayers" *J. Appl. Phys.*, vol. 81, pp. 5315, 1997.

[132] S. S. A. Razee, J. B. Staunton, B. Ginatempo, F. J. Pinski and E. Bruno, "Ab Initio theoretical description of the interrelation between magnetocrystalline anisotropy and atomic short-range order," *Phys. Rev. Lett.,* vol. 82, no. 26, pp. 5369-5372, 1999.

[133] H. Bernas, J. P. Attané, K. H. Heinig, D. Halley, D. Ravelosona and A. Marty *et al.*, "Ordering Intermetallic Alloys by Ion Irradiation: A Way to Tailor Magnetic Media," *Phys. Rev. Lett.,* vol. 91, no. 7, pp. 077203, 2003.

[134] G. Meyer and J. U. Thiele, "Effective electron-density dependence of the magnetocrystalline anisotropy in highly chemically ordered pseudobinary Fe1−xMnx50Pt50 L10 alloys," *Phys. Rev. B,* vol. 73, no. 21, pp. 214438, 2006.

[135] S. M. Heald, J. O. Cross, D. L. Brewe and R. A. Gordon, "The PNC/XOR X-ray microprobe station at APS sector 20," *Nuclear Instruments and Methods in Physics Research Section A: Accelerators, Spectrometers, Detectors and Associated Equipment,* vol. 582, no. 1, pp. 215-217, 2007.

[136] J. O. Cross and A. I. Frenkel, "Use of scattered radiation for absolute x-ray energy calibration," *Rev. Sci. Instrum.,* vol. 70, no. 1, pp. 38-40, 1999.

[137] S. Kraft, J. Stümpel, P. Becker and U. Kuetgens, "High resolution x-ray absorption spectroscopy with absolute energy calibration for the determination of absorption edge energies," *Rev. Sci. Instrum.,* vol. 67, no. 3, pp. 681-687, 1996.

[138] H. Sakurai, F. Itoh, H. Maruyama, A. Koizumi, K. Kobayashi and H. Yamazaki *et al.*, "Circular Magnetic X-Ray Dichroism at the K-Absorption Edge in Fe–Ni Alloys," *J. Phys. Soc. Jpn.,* vol. 62, no. 2, pp. 459-463, 1993.

[139] J. E. Müller, O. Jepsen and J. W. Wilkins, "X-ray absorption spectra: K-edges of 3d transition metals, L-edges of 3d and 4d metals, and M-edges of palladium," *Solid State Commun.,* vol. 42, no. 5, pp. 365-368, 1982.

[140] R. A. Gordon, E. D. Crozier, D. T. Jiang, P. S. Budnik, T. L. Monchesky and B. Heinrich, "In situ XAFS study of Fe epitaxially grown by MBE on GaAs(0 0 1)-4 × 6," *Surface Science,* vol. 581, no. 1, pp. 47-57, 2005.

[141] J. Lyubina, I. Opahle, M. Richter, O. Gutfleisch, K. H. Müller and L. Schultz *et al.*, "Influence of composition and order on the magnetism of Fe–Pt alloys: Neutron powder diffraction and theory," *Appl. Phys. Lett.,* vol. 89, no. 3, pp. 032506, 2006.

[142] N. Inaba, Y. Uesaka and M. Futamoto, "Compositional and temperature dependence of basic magnetic properties of CoCr-alloy thin films," *IEEE Trans. Magn.,* vol. 36, no. 1, pp. 54-60, 2000.

[143] T. Hasegawa, J. Miyahara, T. Narisawa, S. Ishio, H. Yamane and Y. Kondo *et al.*, "Study of ferro-antiferromagnetic transition in [001]-oriented L10 FePt1−xRhx film," *J. Appl. Phys.,* vol. 106, no. 10, pp. 103928, 2009.

[144] D. Lott, J. Fenske, A. Schreyer, P. Mani, G. J. Mankey and F. Klose *et al.*, "Antiferromagnetism in a Fe50Pt40Rh10 thin film investigated using neutron diffraction," *Phys. Rev. B,* vol. 78, no. 17, pp. 174413, 2008.

[145] N. Braidy, Y. L. Bouar, M. Fèvre and C. Ricolleau, "Determination of the long-range order parameter from the tetragonality ratio of L10 alloys," *Phys. Rev. B,* vol. 81, no. 5, pp. 054202, 2010.

[146] D. B. Xu, C. J. Sun, J. S. Chen, S. W. Han, S. M. Heald and R. A. Rosenberg *et al.*, "Investigation of spin and orbital moments of L10 FePtRh thin films," *J. Appl. Phys.,* vol. 111, no. 7, pp. 07C120, 2012.

[147] J. Camarero, Y. Pennec, J. Vogel, S. Pizzini, M. Cartier and F. Fettar *et al.*, "Field dependent exchange coupling in NiO/Co bilayers," *Phys. Rev. B,* vol. 67, no. 2, pp. 020413(R), 2003.

[148] S. Imada, T. Muro, T. Shishidou, S. Suga, H. Maruyama and K. Kobayashi *et al.*, "Orbital contribution to the 3d magnetic moment in ferromagnetic Cu3Au-type transition-metal-Pt alloys probed by soft-x-ray magnetic circular dichroism," *Phys. Rev. B,* vol. 59, no. 13, pp. 8752-8758, 1999.

[149] A. Sakuma, "First Principle Calculation of the Magnetocrystalline Anisotropy Energy of FePt and CoPt Ordered Alloys," *J. Phys. Soc. Jpn.*, vol. 63, no. 8, pp. 3053, 1994.

[150] I. Galanakis, M. Alouani and H. Dreyssé, "Perpendicular magnetic anisotropy of binary alloys: A total-energy calculation," *Phys. Rev. B,* vol. 62, no. 10, pp. 6475-6484, 2000.

[151] I. Galanakis, M. Alouani and H. Dreyssé, "Calculated magnetic properties of low-dimensional systems: the AuCu- and AuCu3-type ferromagnets," *J. Magn. Magn. Mater.,* vol. 242, pp. 27-32, 2002.

[152] C. J. Sun, G. M. Chow, G. H. Fecher, J. S. Chen, H. J. Lin and Y. Hwu, "Spin and Orbital Magnetic Moments of FePt Thin Films," *Jpn. J. Appl. Phys.,* vol. 45, pp. 2539-2541, 2006.

[153] S. Imada, A. Yamasaki, S. Suga, T. Shima and K. Takanashi, "Perpendicular magnetization of L10-ordered FePt films in the thinnest limit," *Appl. Phys. Lett.,* vol. 90, no. 13, pp. 132507, 2007.

[154] O. Šipr, M. Košuth and H. Ebert, "Magnetic structure of free iron clusters compared to iron crystal surfaces," *Phys. Rev. B,* vol. 70, no. 17, pp. 174423, 2004.

[155] I. V. Solovyev, "Orbital Polarization in Itinerant Magnets," *Phys. Rev. Lett.,* vol. 95, no. 26, pp. 267205, 2005.

[156] G. H. O. Daalderop, P. J. Kelly and M. F. H. Schuurmans, "Magnetocrystalline anisotropy and orbital moments in transition-metal compounds," *Phys. Rev. B,* vol. 44, no. 21, pp. 12054-12057, 1991.

[157] C. Stamm, J. U. Thiele, T. Kachel, I. Radu, P. Ramm and M. Kosuth *et al.*, "Antiferromagnetic-ferromagnetic phase transition in FeRh probed by x-ray magnetic circular dichroism," *Phys. Rev. B,* vol. 77, no. 18, pp. 184401, 2008.

[158] C. Meneghini, S. D. Matteo, C. Monesi, T. Neisius, L. Paolasini and S. Mobilio *et al.*, "Antiferromagnetic–paramagnetic insulating transition in Cr-doped V2O3 investigated by EXAFS analysis," *J. Phys.: Condens. Matter,* vol. 21, no. 35, pp. 355401, 2009.